LBL-34880
UC-404

# Lawrence Berkeley Laboratory

UNIVERSITY OF CALIFORNIA

## Materials Sciences Division

# Methyl Quantum Tunneling and Nitrogen-14 NQR NMR Studies Using a SQUID Magnetic Resonance Spectrometer

B.E. Black
(Ph.D. Thesis)

July 1993

LOAN COPY
Circulates
for 4 weeks
Copy 2
Bldg. 50 Library.
LBL-34880

Prepared for the U.S. Department of Energy under Contract Number DE-AC03-76SF00098

**DISCLAIMER**

This document was prepared as an account of work sponsored by the United States Government. Neither the United States Government nor any agency thereof, nor The Regents of the University of California, nor any of their employees, makes any warranty, express or implied, or assumes any legal liability or responsibility for the accuracy, completeness, or usefulness of any information, apparatus, product, or process disclosed, or represents that its use would not infringe privately owned rights. Reference herein to any specific commercial product, process, or service by its trade name, trademark, manufacturer, or otherwise, does not necessarily constitute or imply its endorsement, recommendation, or favoring by the United States Government or any agency thereof, or The Regents of the University of California. The views and opinions of authors expressed herein do not necessarily state or reflect those of the United States Government or any agency thereof or The Regents of the University of California and shall not be used for advertising or product endorsement purposes.

Lawrence Berkeley Laboratory is an equal opportunity employer.

## DISCLAIMER

This document was prepared as an account of work sponsored by the United States Government. While this document is believed to contain correct information, neither the United States Government nor any agency thereof, nor the Regents of the University of California, nor any of their employees, makes any warranty, express or implied, or assumes any legal responsibility for the accuracy, completeness, or usefulness of any information, apparatus, product, or process disclosed, or represents that its use would not infringe privately owned rights. Reference herein to any specific commercial product, process, or service by its trade name, trademark, manufacturer, or otherwise, does not necessarily constitute or imply its endorsement, recommendation, or favoring by the United States Government or any agency thereof, or the Regents of the University of California. The views and opinions of authors expressed herein do not necessarily state or reflect those of the United States Government or any agency thereof or the Regents of the University of California.

LBL-34880
UC-404

# Methyl Quantum Tunneling and Nitrogen-14 NQR NMR Studies Using a SQUID Magnetic Resonance Spectrometer

Bruce Elmer Black

Department of Chemistry
University of California

and

Materials Sciences Division
Lawrence Berkeley Laboratory
University of California
Berkeley, California 94720

July 1993

This work was supported by the Director, Office of Energy Research, Office of Basic Energy Sciences, Materials Sciences Division, of the U.S. Department of Energy under Contract No. DE-AC03-76SF00098.

# Methyl Quantum Tunneling and Nitrogen-14 NQR Studies Using A dc SQUID Magnetic Resonance Spectrometer

Copyright © 1993

by

Bruce Elmer Black

recycled paper

Abstract

Methyl Quantum Tunneling and Nitrogen-14 NQR Studies Using A dc SQUID Magnetic Resonance Spectrometer

by

Bruce Elmer Black

Doctor of Philosophy in Chemistry

University of California at Berkeley

Professor Alex Pines, Chair

Nuclear Magnetic Resonance (NMR) and Nuclear Quadrupole Resonance (NQR) techniques have been very successful in obtaining molecular conformation and dynamics information. Unfortunately, standard NMR and NQR spectrometers are unable to adequately detect resonances below a few megahertz due to the frequency dependent sensitivity of their Faraday coil detectors. For this reason a new spectrometer with a dc SQUID (Superconducting Quantum Interference Device) detector, which has no such frequency dependence, has been developed. Previously, this spectrometer was used to observe $^{11}B$ and $^{27}Al$ NQR resonances. I have increased the scope of this study to include $^{23}Na$, $^{51}V$, and $^{55}Mn$ NQR transitions.

Also, I present a technique to observe $^{14}N$ NQR resonances through cross relaxation of the nitrogen polarization to adjacent proton spins. When the proton Zeeman splitting matches one nitrogen quadrupolar transition the remaining two $^{14}N$ transitions can be detected by sweeping a saturating rf field through resonance. Additionally, simultaneous excitation of two nitrogen resonances provides signal enhancement which helps to connect transitions from the same site. In this way, we have observed nitrogen-14 resonances in several amino acids and polypeptides.

This spectrometer has also been useful in the direct detection of methyl quantum tunneling splittings at 4.2 K. Tunneling frequencies of a homologous series of carboxylic

acids were measured and for solids with equivalent crystal structures, an exponential correlation between the tunneling frequency and the enthalpy of fusion is observed. This correlation provides information about the contribution of intermolecular interactions to the energy barrier for methyl rotation.

# Table of Contents


Table of Contents iii

List of Figures vi

List of Tables ix

Acknowledgements x

Chapter 1 Introduction 1

Chapter 2 The SQUID Magnetic Resonance Spectrometer 4

2.1 Superconductivity in a Magnetic Field 4

2.1.1 Flux Exclusion: The Meisner Effect 5

2.1.2 Flux Trapping and Quantization 8

2.1.3 The Josephson Junction 10

2.2 The dc SQUID 13

2.2.1 Fundamental Description 14

2.2.2 The SQUID as a Detector 17

2.3 The Spectrometer 23

2.3.1 Hardware Overview 24

2.3.2 Software Improvements 27

2.3.3 Operation 28

Chapter 3 Z-axis cw NMR and NQR 29

3.1 Hamiltonians 29

3.1.1 The Quadrupolar Hamiltonian 31

3.1.2 The Zeeman Hamiltonian 38

3.1.3 The Dipolar Hamiltonian 39

3.1.4 rf Irradiation 41

3.2 Relaxation 41

3.2.1 Spin-lattice Relaxation 42

3.2.2 Spin-spin Relaxation (Cross-relaxation) 44

3.3 Z-axis cw Magnetic Resonance 46

3.3.1 Single Crystal NMR (I=1/2) 46

3.3.2 Half Odd Integer Spin Single Crystal NQR 50

3.3.3 Integer Spin NQR 53

3.3.4 Powder Samples 54

3.4 Experimental Lineshapes and Intensities 57

Chapter 4 NQR of I = 3/2, 5/2 and 7/2 Nuclei 63

4.1 Boron-11 (I = 3/2) 63

4.1.1 Sodium Borate Glass 63

4.1.2 Boron Nitride 66

4.2 Sodium-23 (I = 3/2) 66

4.3 Aluminum-27 (I = 5/2) 68

4.3.1 Sapphire ($\alpha$-$Al_2O_3$) Crystal 68

4.3.2 Petalite 72

4.4 Vanadium-51 (I = 7/2) 72

4.5 Manganese-55 (I = 5/2) 75

4.5.1 Potassium Permanganate 76

4.5.2 Silver Permanganate 76

Chapter 5 NQR of Nitrogen-14 (I=1) 80

5.1 The Integer Spin Problem 80

5.2 Direct Detection 83

5.2.1 Solid $\alpha$-$N_2$ 86

5.3 Indirect Detection 86

5.3.1 Single Sweep 89

5.3.2 Single Sweep ($\nu_{cr} = 2\nu_h$) 95

5.3.3 Double Sweep 100

5.3.4 Double Irradiation 104

5.3.5 Level Matching Conditions 106

5.4 Experimental Results 110

Chapter 6 SQUID NMR and Methyl Quantum Tunneling 117

6.1 Theory 117

6.1.1 Barrier Heights 129

6.1.2 Previous Methods 131

6.2 Experimental Results 133

6.3 Correlations with Thermodynamic Properties 135

Bibliography 141

# List of Figures


2.1 The Meisner effect and flux trapping 6

2.2 Schematic of a Josephson junction 11

2.3 Schematic of a dc SQUID 15

2.4 Voltage versus flux curve of a dc SQUID 18

2.5 Feedback and lock-in detection scheme 19

2.6 Pickup coil 22

2.7 SQUID spectrometer 25

2.8 SQUID probe 26

3.1 Electric field gradient 32

3.2 I=7/2 energy level diagram 34

3.3 I=1 energy level diagram 35

3.4 Relative splittings for I=3/2, 5/2, and 7/2 36

3.5 Relative splittings for I=9/2 and 1 37

3.6 Example of a $T_1$ measurement 43

3.7 Cross-relaxation examples 45

3.8 Spin-1/2 energy levels and populations 47

3.9 Theoretical NMR and NQR signals 49

3.10 Spin-3/2 energy levels and populations 51

3.11 Single crystal and powder spectra 56

3.12 Simulated NMR lineshapes as a function of $T_1$ 58

3.13 NQR lineshapes as a function of rf power 60

3.14 NQR lineshapes as a function of sweep time 61

3.15 $^{14}N$ NQR lineshapes as a function of sweep time 62

4.1 $^{11}B$ spectra of $xNa_2O \cdot B_2O_3$ 64

4.2 $^{11}B$ spectrum of BN 67

4.3 $^{23}Na$ spectrum of NaBrO4 69

4.4 $^{27}Al$ spectra of sapphire in different magnetic fields 71

4.5 $^{27}Al$ spectra of petalite 73

4.6 $^{51}V$ spectrum of ammonium metavanadate 74

4.7 $^{55}Mn$ spectra of $KMnO_4$ 77

4.8 $^{55}Mn$ spectra of $AgMnO_4$ 78

5.1 I=1 energy level diagram 82

5.2 Spin-1 problem 85

5.3 $N_2$ spectrum 87

5.4 Single sweep example 92

5.5 Single sweep intensities 96

5.6 Diglycine spectra 97

5.7 Single sweep ($\nu_{cr} = 2\nu_h$) example 99

5.8 Double sweep example 101

5.9 Double sweep intensities 103

5.10 Double irradiation example 105

5.11 Double irradiation intensities 107

5.12 $^{14}N$ spectra of L-alanine with and without double irradiation 108

5.13 $^{14}N$ derivative spectra of L-serine 109

6.1 Harmonic oscillator energy levels 121

6.2 Methyl group rotational potential and energy levels 122

6.3 Methyl spin energy level diagram 125

6.4 Methyl tunneling spectrum of hexanol 127

6.5 Sample tunneling frequencies 130

6.6 Tunneling frequencies of the carboxylic acids 136

6.7 Correlations between $\omega_t$ and $\Delta H_{fus}$ 137

6.8 Sample crystal structure 139

# List of Tables


3.1 Spin properties of nuclei discussed in this work 30

5.1 $^{14}N$ amino acid results 111

5.2 $^{14}N$ polypeptide and other results 112

6.1 $C_3$ character table 118

6.2 Experimental tunneling frequencies 134

# Acknowledgments

I would like to begin by thanking Professor Alex Pines for his encouragement and support of this research. I would also especially acknowledge Chuck Connor and Jeff Chang for building the SQUID magnetic resonance spectrometer. Their work provided the foundation upon which I could build. Jeff introduced me to the experiment and together we worked on $^{11}B$ and $^{27}Al$ NQR and the direct detection of $^{14}N$ quadrupolar resonances. Francois Creuzet provided the samples and helped in an unsuccessful attempt to study sodium borosilicate glasses.

Günter Meyer and John Harwood were my coworkers on the measurement of methyl quantum tunneling splittings of the carboxylic acids. Günter and I went on to discover the tunneling frequency-enthalpy of fusion correlation. Special thanks go to Ulrike Werner for her help in the general understanding and in further experiments on the methyl group project.

She has also played an important role in the development of the $^{14}N$ NQR indirect detection method. Together with Marcia Ziegeweid, we have applied this technique to amino acids and polypeptides.

In addition to all the people mentioned above, I would like to express my appreciation to all the members of the Pines group. I have enjoyed their encouragement, interest, and friendship over the past five years.

And finally a special thanks goes to my family. My wife, "A", has generously supported me during my entire graduate school career. She has helped when things have not gone well and celebrated with me when I have accomplished my goals. Also, my son, Benjamin, has been a great source of joy for me. His birth near the beginning of this thesis writing period and his subsequent needs have increased the preparation time of this work, but have also made it less of a drudgery. I have enjoyed watching him grow over the past six months.

This work was supported by the Director, Office of Energy Research, Office of Basic Energy Sciences, Materials Sciences Division of the U.S. Department of Energy under Contract No. DE-AC03-76SF00098.

# Chapter 1
# Introduction

Magnetic resonance has become an important tool in the modern scientist's arsenal for the determination of structural and dynamical information. One source of molecular information is the quadrupolar coupling which describes the interaction of the electric quadrupole moment of the nucleus with a surrounding electric field gradient.[1-3] This electric field gradient is caused primarily by the asymmetric distribution of bonding electrons, but may also result from ions and lattice defects. Thus the quadrupolar interaction reflects the environment around the nucleus and can provide information about coordination number, bonding symmetry, lattice symmetry, and defects.

Solid state NMR and NQR are used to examine this interaction. Unfortunately, unlike liquid NMR, solid state NMR suffers from a deficiency in resolution due to the lack of molecular motion, which in a liquid serves to average anisotropic interactions to zero. In solid state powder samples, anisotropies from the dipolar and quadrupolar couplings broaden the spectrum often to the point where all information is lost.[4, 5] To combat this problem several techniques have been developed. For spin-1/2 nuclei (those with no quadrupolar moment) magic-angle spinning (MAS) sharpens the resonances by eliminating the dipolar anisotropy.[6]

However, for nuclei with $I>1/2$ this is not good enough as the quadrupolar anisotropy is not completely averaged. For nuclei with $I=3/2$, $5/2$, $7/2$, ... and small quadrupolar couplings, dynamic angle spinning (DAS) and double rotation spinning (DOR) have been proven to be very successful in providing resolved spectra of the central transition ($-1/2 \leftrightarrow +1/2$).[7-9] From these experiments information about the sample can be obtained including the dipolar and quadrupolar couplings. For integer spin nuclei, however, there is no central transition and a good direct technique such as this is not available.

It is also possible to study the quadrupolar interaction by zero field techniques, primarily Nuclear Quadrupole Resonance (NQR).[1] In NQR the quadrupolar splittings are directly measured rather than calculated from simulated lineshapes as in the NMR experiments discussed above. Typical NQR experiments can measure large quadrupolar couplings of nuclei such as the halogens.

Unfortunately, both standard NMR and NQR techniques suffer when it comes to measuring low frequency resonances. This is due to their detection scheme. Most magnetic resonance spectrometers use a Faraday detector. This is simply a coil which measures the voltage produced by the Faraday effect as the transverse magnetization oscillates after rf irradiation at the resonance frequency.[10] The sensitivity of the Faraday effect is proportional to the rate of change in magnetization ($d\Phi/dt$).[11] Thus the voltage decreases linearly with the resonance frequency. This places a limit of several MHz on the detectable resonances. However, many important nuclei, such as $^{11}B$, $^{14}N$, $^{23}Na$, and $^{27}Al$ have smaller splittings. So a new technique must be found to study these materials. One such method is field cycling[12, 13] which, however, is an inherent two dimensional experiment and has the disadvantage of long experimental times.

Another promising technique is described in this thesis. This spectrometer uses a dc SQUID[14-16] (Superconducting Quantum Interference Device) as a detector of magnetic resonance signals.[17, 18] The SQUID is able to directly detect changes in magnetic flux. This type of detector has no inherent frequency dependence.[19] Thus the SQUID magnetic resonance spectrometer is able to observe quadrupolar splittings in a frequency range that was difficult to investigate before. Chapter 2 describes the theory behind the utilization of the SQUID as a detector. It also presents a brief outline of the SQUID magnetic resonance spectrometer. Chapter 3 continues with a general description of the experimental technique and an overview of the expected spectra.

While working on this project I have expanded the range of samples that have been investigated. During this time we have added $^{23}Na$, $^{51}V$, and $^{55}Mn$ to the nuclei that have

already been studied: $^{11}B$ and $^{27}Al$.[17, 18, 20-22] Chapter 4 presents results from my experiments involving these materials.

Also, we have developed a new technique for the study of integer spin NQR, primarily $^{14}N$, which now allows us to analyze some biologically important molecules. The theory and results of these experiments are presented in Chapter 5.

There is even information to be gained from very low field (50-200 G) NMR experiments. One example is methyl quantum tunneling.[23] In high magnetic fields these transitions are forbidden. However, in low field the nonsecular parts of the dipolar Hamiltonian provide a means whereby tunneling transitions become slightly allowed.[24] The SQUID spectrometer has proven useful in studying methyl groups attached to $sp^3$ hybridized carbon atoms which normally have tunneling frequencies less than 1 MHz.[25, 26] These results are presented in Chapter 6 along with an interesting correlation between the tunneling frequency and thermodynamic properties of the straight-chained carboxylic acids.

Overall the SQUID detection scheme proves to be a viable technique for the study of low frequency magnetic resonance and compares favorably with other methods.

# Chapter 2
# The SQUID Magnetic Resonance Spectrometer

This chapter focuses on a brief description of the dc SQUID and the SQUID spectrometer. Both of these subjects are presented in greater detail elsewhere,[15, 17, 18, 21, 27-36] my purpose is simply to provide a working knowledge of the spectrometer and the SQUID that will allow one to understand the experiments in this thesis.

Because the SQUID is a device designed to use the unique properties of a superconductor in a magnetic field I will begin this chapter with a discussion of that subject including descriptions of the Meisner effect or flux exclusion, flux trapping and quantization, and the Josephson junction. The second part of the chapter will introduce the theory behind the operation of a dc SQUID and explain how it can be used as a magnetic resonance detector. The third section will present a survey of the spectrometer and outline several recent changes in operation.

## 2.1 Superconductivity in a Magnetic Field

In 1911, Kammerlingh Onnes found that cooling mercury to a temperature below 4.2 K resulted in a precipitous drop in resistivity.[37] Thus was born the study of superconductors. In 1957, Bardeen, Cooper, and Schrieffer formulated a theory which characterized a majority of superconductors.[38] It described the net attraction of two electrons coupled by a phonon. These sets of electrons became known as Cooper pairs. In this coupled state they behave like bosons, in that all electron pairs can be described by the same bound-state wavefunction. The BCS theory describes many superconductors successfully, but is found to be inadequate for many materials such as high $T_C$ and organic

superconductors. However, in this thesis I will be concerned only with materials that do act in accordance with the BCS theory.

When superconductors are placed in a magnetic field, it was found that they can be classified into two distinct types.[31] Type I materials remain in the superconducting state as long as the field is below a specific critical value which is dependent on the type of material and its purity. Above that field it is no longer superconducting. Type II superconductors have two critical field values, $H_{C1}$ and $H_{C2}$ ($H_{C1} < H_{C2}$). Below $H_{C1}$ the entire substance is superconducting like the Type I materials. Between the two critical fields, parts of the sample become nonsuperconducting. The amount of superconducting material varies linearly with the field until above $H_{C2}$ the entire sample is nonsuperconducting. The critical fields for many superconductors are in the low to moderate field strengths. One example is lead which has a critical field of 803 gauss at absolute zero.[39] All magnetic field strengths in the experiments described in this thesis are well below the critical fields of the superconducting materials used in the spectrometer.

## 2.1.1 Flux Exclusion: The Meisner Effect

When a magnetic field is applied around a superconductor, the material generates currents to oppose the field according to Lenz's law. Because there is no resistance in the superconducting state, these persistent currents will eliminate the magnetic field in the interior of the superconductor. Thus magnetic flux is excluded from the material except for a narrow region near the surface, the depth of which is calculated below.

More interesting is the related phenomenon discovered experimentally by Meisner and depicted in Figure 2.1.[40] He found that if a piece of potentially superconducting material is placed in a magnetic field at high temperature and then cooled below its critical superconducting temperature, $T_C$, the magnetic field will also be excluded from the interior

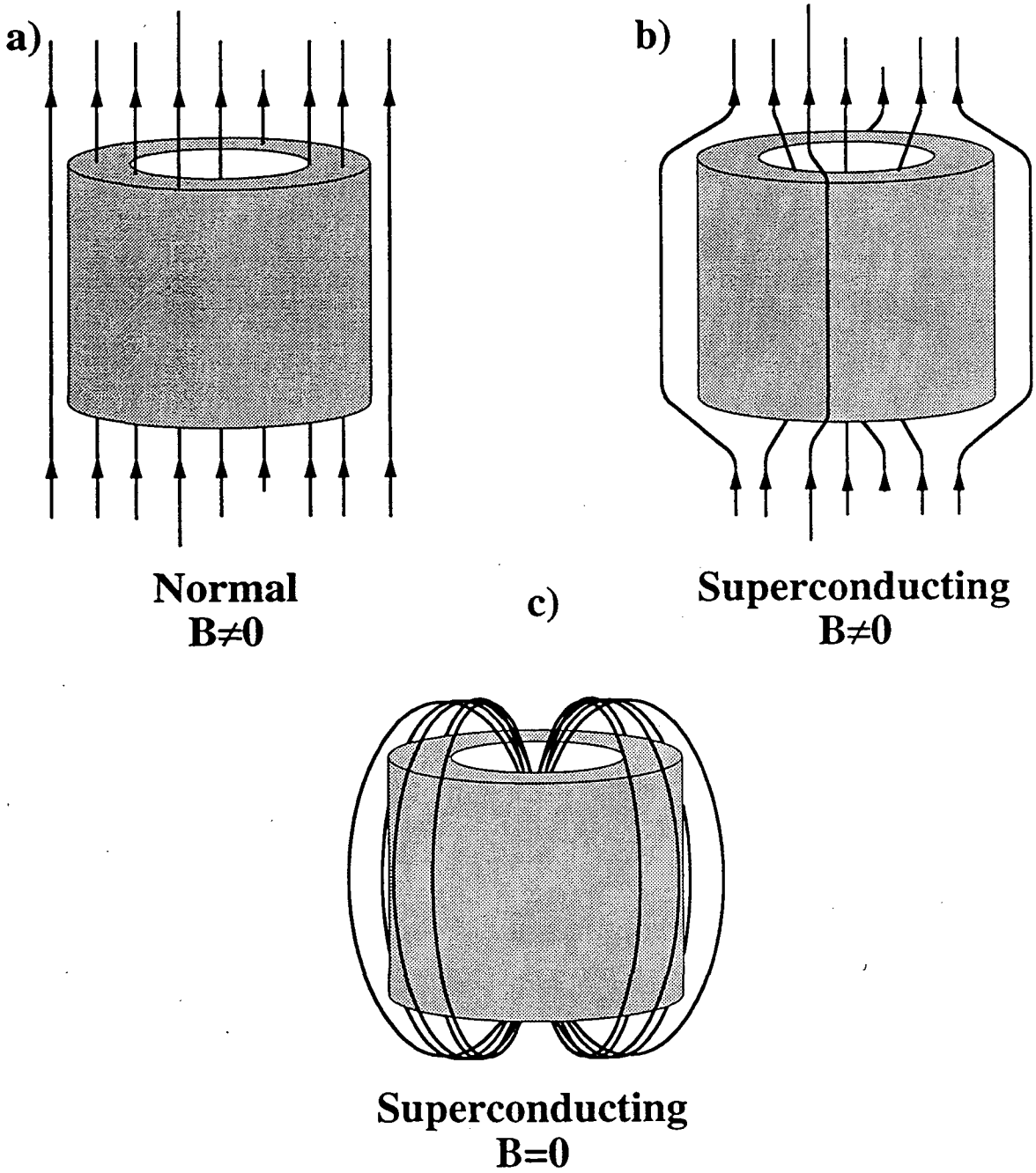


Figure 2.1. Superconducting material in a magnetic field. a) Before it is cooled the magnetic flux penetrates the sample. b) After it become superconducting, the flux is excluded from the interior of the sample. This is the Meisner effect. c) When the magnetic field is removed from a superconducting ring, currents flow around the surface that keep the magnetic flux through the ring constant. This is flux trapping.

of the superconductor. The explanation of this result can be found by first developing the London equation.[41, 42]

The velocity of a particle, as determined by kinematics, is

$$v = \frac{1}{m}(p - \frac{q}{c}A) \qquad 2.1$$

where m is the mass of the particle, p its momentum, q its charge, c the speed of light, and A the vector potential due to the magnetic field. When p is replaced by its quantum mechanical analog, $-i\hbar\nabla$,

$$v = \frac{1}{m}(-i\hbar\nabla - \frac{q}{c}A). \qquad 2.2$$

Let the superconductor wavefunction be written as

$$\Psi = \sqrt{\rho}\,\exp(i\theta(r)) \qquad 2.3$$

where $\rho$ is the concentration of Cooper pairs in the superconductor which we will assume to be relatively constant over the sample. The particle flux is then given by

$$\Psi v \Psi^* = \frac{\rho}{m}(\hbar\nabla\theta - \frac{q}{c}A) \qquad 2.4$$

and we can express the electric current density as

$$j = q\Psi v \Psi^* = \frac{\rho q}{m}(\hbar\nabla\theta - \frac{q}{c}A). \qquad 2.5$$

Taking the curl of each side eliminates the $\nabla\theta$ term (the curl of a scalar is zero) and gives the London equation:

$$\nabla \mathbf{X}\, j = -\frac{\rho q^2}{mc}(\nabla \mathbf{X}\, A) = -\frac{\rho q^2}{mc}B. \qquad 2.6$$

One of Maxwell's equations states that

$$\nabla \mathbf{X} B = \frac{4\pi}{c} j. \qquad 2.7$$

Taking the curl of 2.7 and substituting in 2.6 gives

$$\nabla \mathbf{X} \nabla \mathbf{X} B = -\nabla^2 B = \frac{4\pi}{c} \nabla \mathbf{X} j = -\frac{4\pi\rho q^2}{mc^2} B. \qquad 2.8$$

We will define the London penetration depth, $\lambda$, to be

$$\lambda = \sqrt{\frac{mc^2}{4\pi\rho q^2}}. \qquad 2.9$$

Equation 2.8 then reduces to

$$\nabla^2 B = \frac{1}{\lambda^2} B \qquad 2.10$$

which has a solution

$$B(r) = B(0) \exp(-\frac{r}{\lambda}). \qquad 2.11$$

Thus the magnetic field drops asymptotically to zero. A typical penetration depth into the superconductor, $\lambda$, is calculated to be on the order of 100 Å. From this result we see that the bulk of the superconductor feels no net magnetic field.

## 2.1.2 Flux Trapping and Quantization

Something interesting happens if, instead of a solid sample, a ring of superconducting material is placed into a magnetic field at high temperature and cooled below $T_C$.[43] Even when the magnetic field is removed the flux through the ring remains constant, as depicted in Figure 2.1, and is quantized. The field is retained by a supercurrent that circulates around the ring surface which maintains the flux despite any

change in the surrounding magnetic field. This is commonly called flux trapping. We use this property to provide a small steady field for our magnetic resonance experiments.

We start with equation 2.5;

$$j = \frac{\rho q}{m}(\hbar\nabla\theta - \frac{q}{c}A). \qquad 2.5$$

Let's examine a closed path C through the interior of the superconductor but well away from the surface. We know from the previous section that B and thus j are zero in this region. So,

$$\hbar c\nabla\theta = qA. \qquad 2.12$$

When we integrate the left side of equation 2.12 around the path C and realize that the wavefunction, $\Psi$, must be single valued we find that

$$\hbar c\oint_C \nabla\theta \, dl = 2\pi n\hbar c. \qquad 2.13$$

Integrating the right side of equation 2.12 and applying Stoke's theorem gives us

$$q(\oint_C A \, dl) = q\iint(\nabla \text{ X } A) \, d\sigma = q\iint B \, d\sigma = q\Phi \qquad 2.14$$

where $\Phi$ is the magnetic flux through the region bound by C. Combining equations 2.12, 2.13, and 2.14 renders

$$\Phi = \frac{2\pi\hbar c}{q} n. \qquad 2.15$$

Thus we see that the magnetic flux through the ring is constant and quantized in units of a magnetic flux quantum, $\Phi_0$, where

$$\Phi_0 = \frac{2\pi\hbar c}{q} = 2.0678 \text{ X } 10^{-7} \text{ Gauss cm}^2. \qquad 2.16$$

This information will have significance later when we consider the SQUID which is primarily a superconducting ring.

### 2.1.3 The Josephson Junction

The next subject in this review is the Josephson junction.[27, 28, 43, 44] A Josephson junction is formed by two bulk superconductors separated by either insulating material or a much narrower superconducting region as depicted in Figure 2.2.[27, 28, 44] If this barrier is small enough, significant tunneling across the junction will occur when a bias current is applied. The tunneling of Cooper pairs in this manner provides a supercurrent. A definite phase relationship exists between the wavefunctions of the two bulk superconductors.[38] But first we will start with two superconducting materials and assume isolated wavefunctions;

$$\Psi_1 = \sqrt{\rho_1}\,\exp(i\theta_1(r)) \qquad 2.17a$$

$$\Psi_2 = \sqrt{\rho_2}\,\exp(i\theta_2(r)). \qquad 2.17b$$

When tunneling of electrons from one piece to the other is allowed and a potential, V, is applied across the junction the following time dependent Schrödinger equations can be written;

$$i\hbar\frac{\partial\Psi_1}{\partial t} = \hbar T\Psi_2 + eV\Psi_1, \qquad 2.18a$$

$$i\hbar\frac{\partial\Psi_2}{\partial t} = \hbar T\Psi_1 - eV\Psi_2 \qquad 2.18b$$

where $\hbar T$ represents the tunneling of electrons across the junction and T has the dimensions of a rate or frequency.

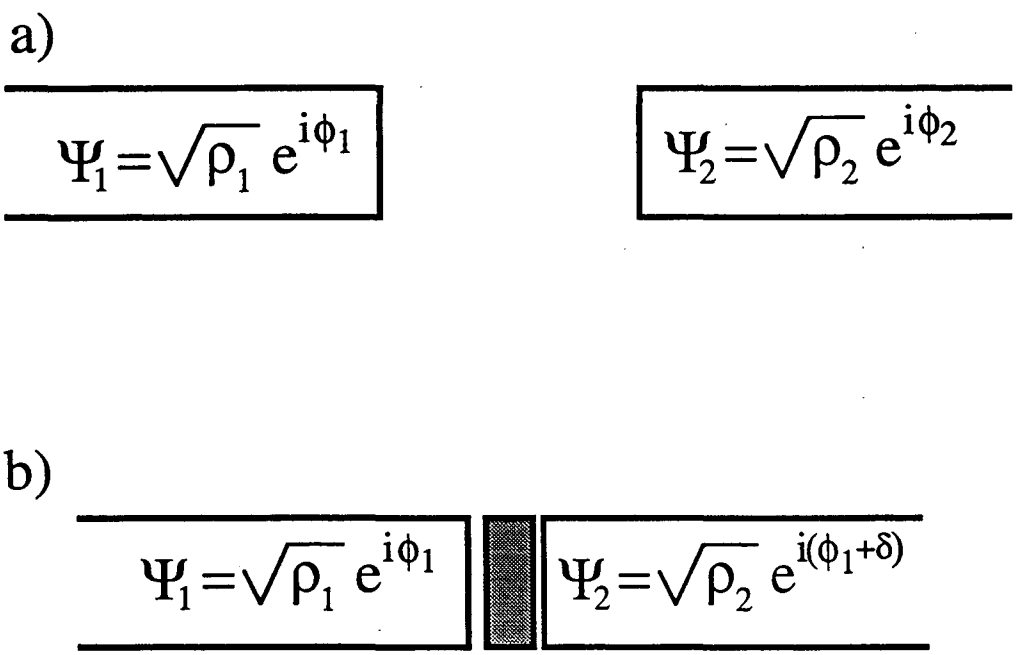


Figure 2.2. The Josephson junction is made of two bulk superconductors connected by a small nonsuperconducting region or a narrower band of superconducting material. If the two bulk samples are not to far away from one another and a biasing current is applied, electrons can tunnel between the two samples and still retain their Cooper pair identity. The current from these tunneling electrons is called the supercurrent.

Combining equations 2.17a and 2.18a gives

$$\frac{\partial\Psi_1}{\partial t} = \frac{1}{2\sqrt{\rho_1}}\exp(i\theta_1)\frac{\partial\rho_1}{\partial t} + i\Psi_1\frac{\partial\theta_1}{\partial t} = -iT\Psi_2 - \frac{ieV\Psi_1}{\hbar} \qquad 2.19$$

and a similar equation for $\Psi_2$. Multiplying 2.19 by $\sqrt{\rho_1}\exp(-i\theta_1)$ and setting $\Delta = \theta_2 - \theta_1$ leaves

$$\frac{1}{2}\frac{\partial\rho_1}{\partial t} + i\rho_1\frac{\partial\theta_1}{\partial t} = -\frac{ieV\rho_1}{\hbar} - iT\sqrt{\rho_1\rho_2}\exp(i\Delta). \qquad 2.20a$$

Multiplying the corresponding equation for $\Psi_2$ by $\sqrt{\rho_2}\exp(-i\theta_2)$ gives

$$\frac{1}{2}\frac{\partial\rho_2}{\partial t} + i\rho_2\frac{\partial\theta_2}{\partial t} = +\frac{ieV\rho_2}{\hbar} - iT\sqrt{\rho_1\rho_2}\exp(-i\Delta). \qquad 2.20b$$

By letting $\exp(i\Delta) = \cos(\Delta) + i\sin(\Delta)$ and equating real and imaginary part we find that;

$$\frac{\partial\rho_1}{\partial t} = 2T\sqrt{\rho_1\rho_2}\sin(\Delta) = -\frac{\partial\rho_2}{\partial t}, \qquad 2.21$$

$$\frac{\partial\theta_1}{\partial t} = -\frac{eV}{\hbar} - T\sqrt{\frac{\rho_2}{\rho_1}}\cos(\Delta), \qquad 2.22$$

$$\frac{\partial\theta_2}{\partial t} = \frac{eV}{\hbar} - T\sqrt{\frac{\rho_1}{\rho_2}}\cos(\Delta). \qquad 2.23$$

If the two junctions are the same then

$$\rho_1 = \rho_2 \qquad 2.24$$

and thus

$$\frac{\partial(\theta_2-\theta_1)}{\partial t} = \frac{\partial\Delta}{\partial t} = \frac{2eV}{\hbar}. \qquad 2.25$$

Upon integration,

$$\Delta(t) = \Delta(0) + \frac{2eVt}{\hbar}. \qquad 2.26$$

The supercurrent flow, $j_s$, is proportional to $\frac{\partial \rho}{\partial t}$, which combined with equation 2.26 results in

$$j_s = j_{s0} \sin(\Delta(t)) = j_{s0} \sin(\Delta(0) + \frac{2eVt}{\hbar}). \qquad 2.27$$

We see that the current between the two bulk superconductors oscillates at a frequency,

$$\omega = \frac{2eV}{\hbar} \qquad 2.28$$

which is 486 MHz for a potential of 1 μV. In our dc SQUID spectrometer the junction is biased by several microvolts giving oscillations in the gigahertz range. We are able to ignore these oscillations by using a narrowband detector, which retrieves only the time averaged value of the supercurrent.

## 2.2 The dc SQUID

As mentioned earlier the dc SQUID is essentially a superconducting ring. It also has two Josephson junctions placed in the ring as shown in Figure 2.3. The characteristics of the SQUID are governed by these two facts which create quantum interference between the supercurrents flowing through each side of the SQUID.[31, 38] These supercurrents will have a phase based on the magnetic flux penetrating the ring and thus be a function of the strength of the magnetic field. This attribute makes the SQUID a sensitive detector of change in magnetic flux. We will utilize this property in order to measure magnetic resonance signals. A more detailed and mathematical description of the process is given below.

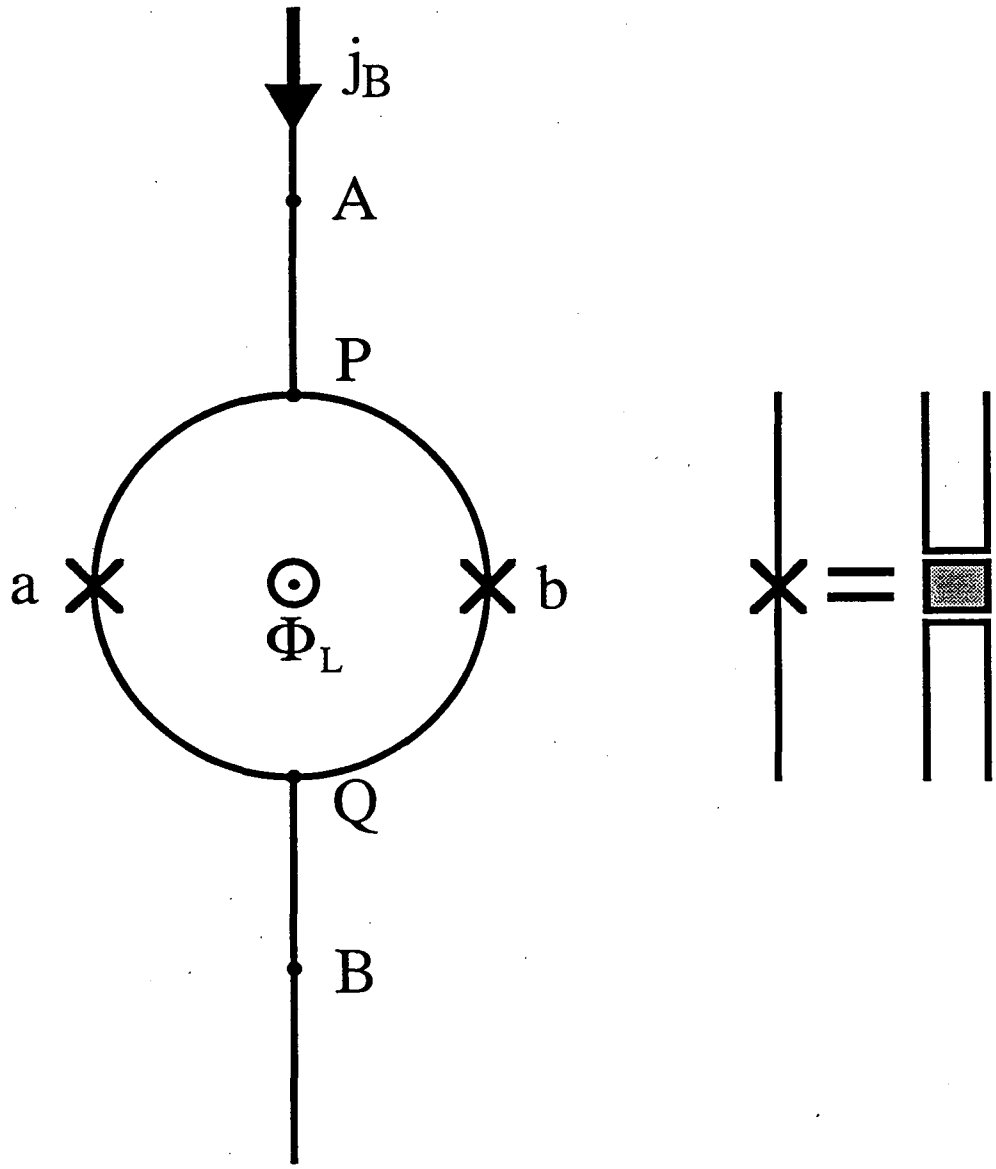


Figure 2.3. A dc SQUID (left) consists of two Josephson junctions (right), a and b, connected in parallel. As superconducting electrons travel through the SQUID, they acquire a phase which depends on the amount of magnetic flux threading the loop. Quantum interference between the pairs produces a periodic voltage across the SQUID which is a function of $\Phi_L$.

## 2.2.1 Fundamental Description [27, 32-35]

The dc SQUID in our detector (depicted in Figure 2.3) contains two parallel Josephson junctions; a and b, a magnetic flux, $\Phi_L$, penetrating the loop; a potential, V, across the junctions; and a current, $j_b$, biasing the SQUID. A supercurrent is generated through the Josephson junctions as described above which can be separated into two parts, one component going between points P and Q through junction a and the other going through junction b. Each part of the supercurrent will gain a phase due to both the Josephson junction and the vector potential of the magnetic field:

$$\Delta\phi_a(t) = \Delta_a(t) + \frac{2e}{\hbar c}\int_P^Q A ds \qquad 2.29a$$

$$\Delta\phi_b(t) = \Delta_b(t) + \frac{2e}{\hbar c}\int_P^Q A ds. \qquad 2.29b$$

By recognizing that the current must be single valued we know that

$$\Delta\phi_b(t) - \Delta\phi_a(t) = 2\pi n. \qquad 2.30$$

For simplification we will set n=0. Thus

$$\Delta_b(t) - \Delta_a(t) = \frac{2e}{\hbar c}\oint A\, ds = \frac{2e}{\hbar c}\Phi_L. \qquad 2.31$$

We combine equations 2.30 and 2.31 to give

$$\Delta\phi_a'(t) = \Delta_a(t) - \frac{e}{\hbar c}\Phi_L, \qquad 2.32a$$

$$\Delta\phi_b'(t) = \Delta_b(t) + \frac{e}{\hbar c}\Phi_L. \qquad 2.32b$$

The total supercurrent will then be

$$j_s = j_{sa}\sin(\Delta\phi_a'(t)) + j_{sb}\sin(\Delta\phi_b'(t)) \qquad 2.33$$

where $j_{sa}$ and $j_{sb}$ are the maximum supercurrents going through each half of the SQUID. For simplification we will assume that the two junctions are equivalent so that $j_{sa} = j_{sb} = j_{s0}$ and $\Delta_a(t) = \Delta_b(t) = \Delta(t)$. Thus

$$\begin{aligned} j_s &= j_{s0} \sin(\Delta(t) - \frac{e}{\hbar c}\phi) + j_{s0} \sin(\Delta(t) + \frac{e}{\hbar c}\Phi_L) \\ &= 2j_{s0} \sin(\Delta(t)) \cos(\frac{e}{\hbar c}\Phi_L). \end{aligned} \qquad 2.34$$

Therefore the supercurrent is a sinusoidal function of the magnetic flux.

The voltage across the SQUID is proportional to the normal current (the difference between the bias current and the supercurrent so long as $j_b > 2j_{s0}$):

$$V(t) = R(j_b - 2j_{s0} \sin(\Delta(t)) \cos(\frac{e}{\hbar c}\Phi_L)). \qquad 2.35$$

We note also that $\Delta(t)$ is a function of the voltage and oscillates at a very high frequency, however as mentioned above, a narrowband detector will only observe the time averaged voltage. This is not simply zero.

From equation 2.25, we know that

$$V(t) = \frac{\hbar}{2e}\frac{\partial\Delta(t)}{\partial t}. \qquad 2.36$$

Rearranging to find the period of one oscillation gives

$$T = \int_0^T dt = \frac{\hbar}{2e}\int_0^{2\pi}\frac{d\Delta(t)}{V(t)}$$

$$= \frac{\hbar}{2e}\int_0^{2\pi}\frac{d\Delta(t)}{R(j_b(t) - 2j_{s0}\sin(\Delta(t))\cos(\frac{e}{\hbar c}\Phi_L))}. \qquad 2.37$$

We can also calculate the time averaged value of the voltage over one period as

$$V=\frac{1}{T}\int V(t)\,dt = \frac{\hbar}{2eT}\int \frac{d\Delta(t)}{dt}\,dt = \frac{\hbar}{2eT}\,2\pi. \qquad 2.38$$

Combining equations 2.37 and 2.38 provides

$$V = \frac{\hbar}{2e}\,2\pi\,\frac{2eR}{\hbar}\left(\int \frac{d\Delta(t)}{(j_b(t) - 2j_{s0}\sin(\Delta(t))\cos(\frac{e}{\hbar c}\Phi_L))}\right)^{-1}. \qquad 2.39$$

Which upon evaluation of the integral leaves

$$V = R\sqrt{j_b^2 - (2j_{s0}\cos(\frac{e}{\hbar c}\Phi_L))^2}. \qquad 2.40$$

Therefore, the time averaged voltage is also a function of the magnetic flux penetrating the SQUID. Figure 2.4 plots the voltage dependence of the magnetic flux.

## 2.2.2 The SQUID as a Detector

There are several simple ways in which the SQUID can be used as a detector. First, for changes in magnetic flux that are much greater than a single flux quantum, one can simply count the number of oscillations in the voltage to obtain the number of flux quanta in the signal. Alternatively, for flux changes much less than one flux quantum, one can set the SQUID at the linear part of the flux versus voltage curve. As long as the flux change is small the voltage change will be a linear function of the flux. Neither of these two schemes is satisfactory for most applications.

More typically the SQUID is used as a null detector in a negative feedback loop[45] as shown in Figure 2.5. The output from the SQUID due to the change in the magnetic flux is fed through the appropriate electronics and a portion of the voltage obtained is then used to drive a coil around the SQUID that will offset the actual magnetic flux change. This means

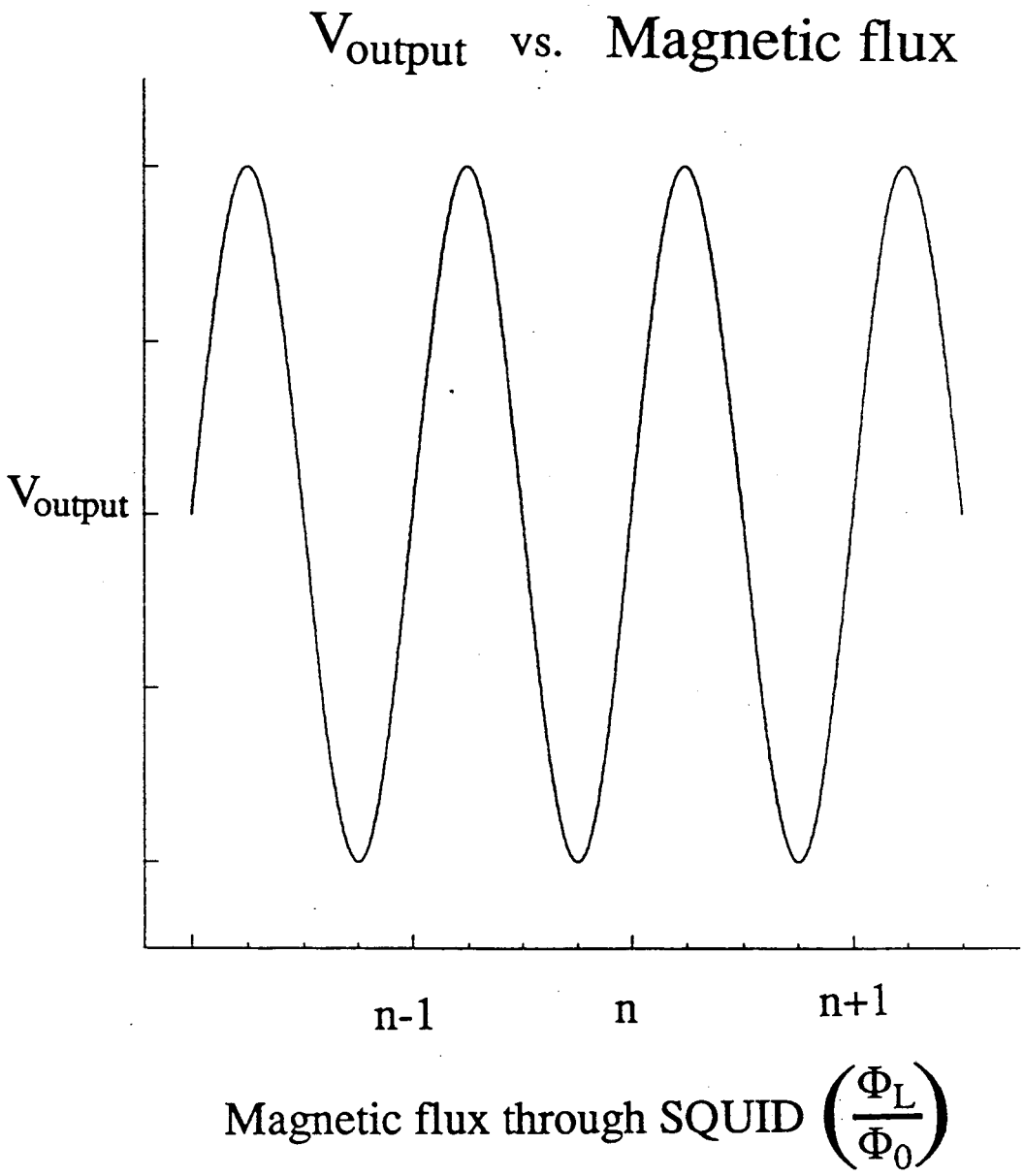


Figure 2.4. Due to the quantum interference of the supercurrent going through the two Josephson junctions, the averaged voltage is a function of the magnetic flux threading the SQUID.

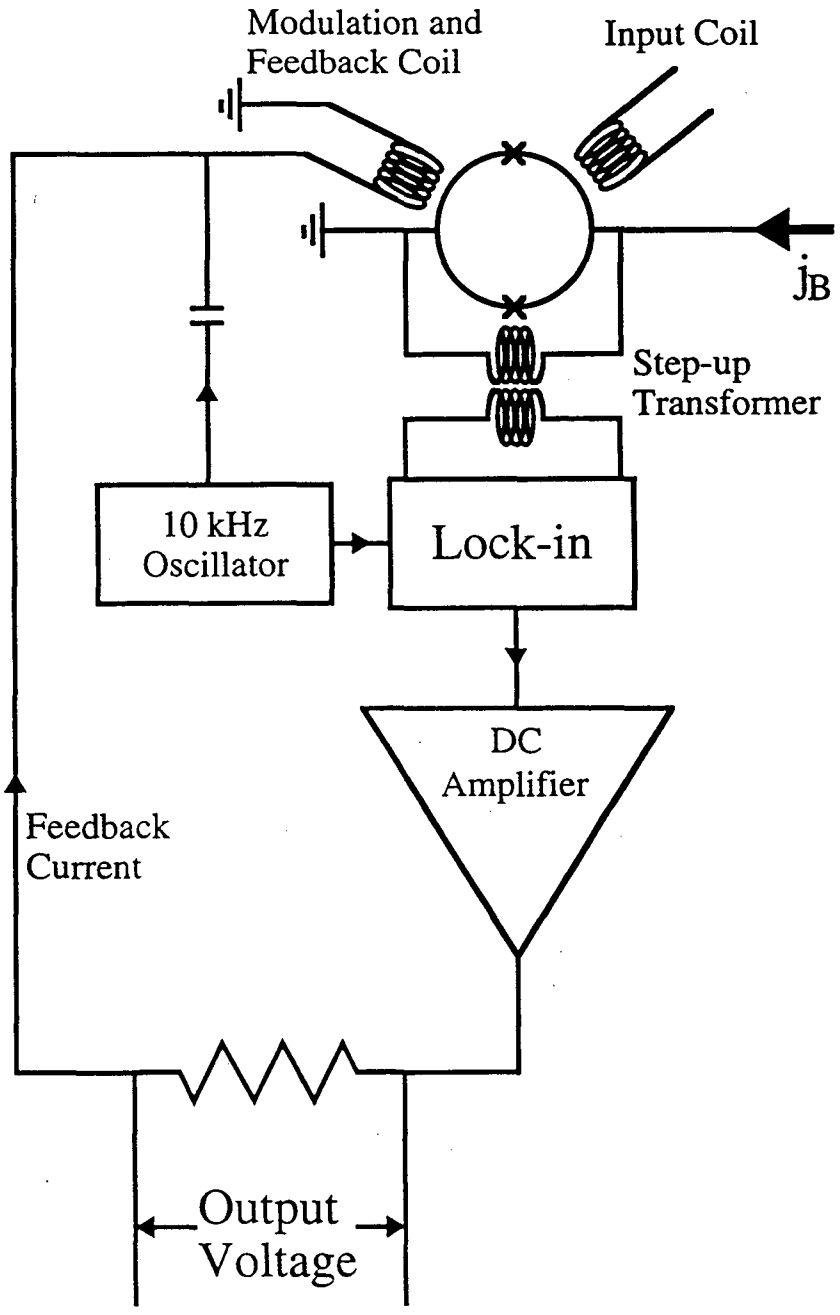


Figure 2.5. A schematic of the SQUID system with the coils, lock-in detection electronics, and feedback circuit. This scheme has low system noise and high sensitivity.

that the magnetic flux through the SQUID will remain constant. The size of the magnetic flux change is no longer a limitation as long as it doesn't vary faster than the electronics can react.

The SQUID is very useful for detecting low frequency resonances. These are difficult to observe by standard NQR techniques which use the induction of current in a wound coil for detection. This Faraday detector measures the changes in the oscillating magnetic flux as a function of time ($d\Phi/dt$). This is obviously frequency dependent, i.e. as the frequency decreases so does $d\Phi/dt$. Therein lies the strength of the SQUID detector. It measures the magnetic flux directly, which has no frequency dependence.

With this advantage we want to use the SQUID to detect low frequency (down to dc) signals. However, the system's noise power has a 1/f characteristic which dominates at low frequencies.[30] This is important in our experiments where we measure a change in the magnetization of a sample over several seconds, which corresponds to frequencies very close to dc. The usual remedy for this problem is frequency modulation, also known as lock-in detection.[46]

In this process the low frequency signal is mixed with a higher frequency carrier wave. This higher frequency signal can then be detected with only the typical white noise. One disadvantage of this system is that signals with frequencies greater than the mixing frequency are lost. Because the modulation frequency is limited by unavoidable stray reactances in the detection and feedback circuits it is generally less than a few hundred kilohertz. For our cw-spectrometer this is not important because the signals are always near dc. But it does provide an important limitation for a pulsed SQUID NMR/NQR spectrometer, where the signal is detected at the frequency of the resonance.

The next problem to be solved is how to couple the signal into the SQUID. One could build a SQUID and rf coils around the sample container.[47] Then when a resonance frequency is irradiated the change in magnetization of the sample will be detected directly by the surrounding SQUID. This however is not practical. First, SQUIDs are typically

very small, on the order of micrometers or less, therefore the sample must be that small as well. Also, the ability to change the sample would be severally hampered by the size and delicacy of the SQUID. And lastly, the sample would always have to remain at the temperature of the SQUID which, as will be seen in Chapter 3, is often not an advantageous situation.

A typical solution for many uses is a flux transformer or pickup coil.[48] To detect low frequency signals an untuned superconducting circuit couples the sample flux into the SQUID as shown in Figure 2.6. The circuit is simply two superconducting coils made from a single piece of superconducting wire with one coil around the SQUID and the other coil, the pickup coil, surrounding the sample. As we sweep through a resonance the sample magnetization, and thus the magnetic flux through the pickup coil, will change. As described previously, the flux through a superconducting ring, or coil, is kept constant. So as the flux changes in the pickup coil a supercurrent is generated that produces a flux change of equal magnitude but opposite direction in the coil around the SQUID which is then detected.

This circuit, as all others, suffers losses and so it is worthwhile to discuss the circuit design. The magnetic flux generated in the pickup coil by a sample of magnetization, M, is

$$\Phi_p = 4\pi^2 f r_p^2 N_p M \qquad 2.41$$

where f is the filling factor, $r_p$ is the radius of the pickup coil, and $N_p$ is the number of turns in the pickup coil. This magnetic flux will induce a current in the superconducting circuit of

$$I_p = \frac{\Phi_p}{(l_s + l_p)}, \qquad 2.42$$

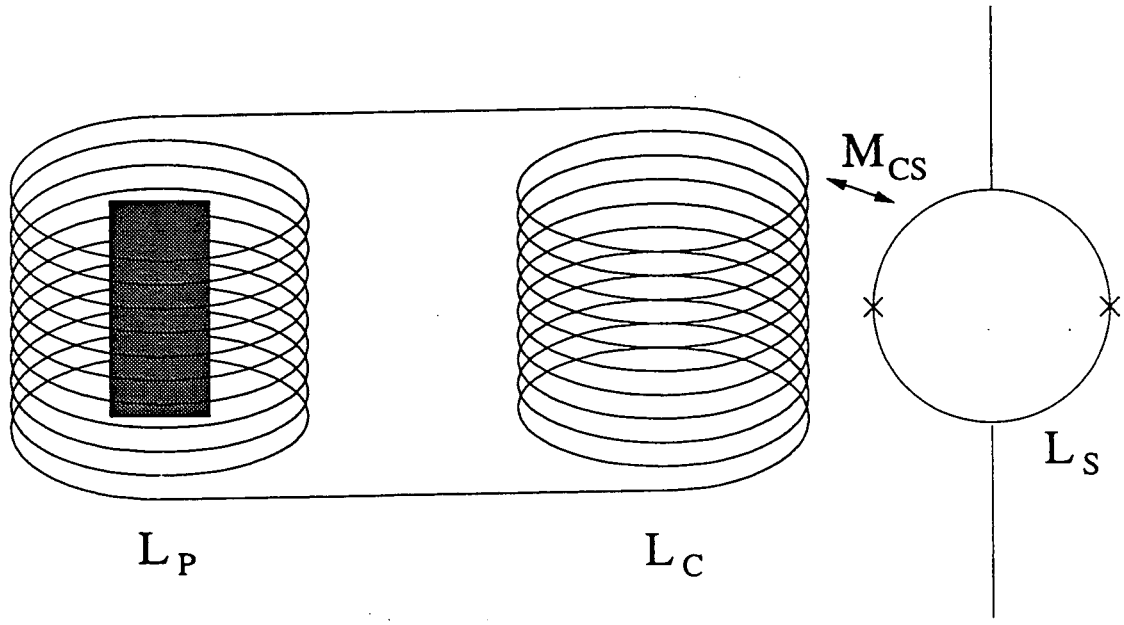


Figure 2.6. A schematic of the superconducting transformer used to couple the sample flux into the dc SQUID. A change in magnetic flux through the pickup coil causes an opposing change at the other coil. This it then coupled into the SQUID by mutual inductance, $M_{CS}$.

where $l_s$ and $l_p$ are the inductances of the coil around the SQUID and the pickup coil respectively. The amount of flux ultimately coupled into the SQUID depends on the mutual inductance between the coupling coil and the SQUID, $M_{cs}$, as given by

$$\Phi_s = I_p M_{cs} = \frac{M_{cs}}{(l_p + l_s)} *(4\pi^2 f r_p^2 N_p M). \qquad 2.43$$

Previous work has shown that the maximum signal is attained when $l_p = l_s$, for a fixed sample size.[30] So to maximize the signal other factors must be considered as $l_s$ is fixed because the coil is manufactured with the SQUID.

Assuming the ideal case,

$$l_p \propto r_p N_p^2, \qquad 2.44$$

the flux through the SQUID will increase approximately as $r^{3/2}$ for a given sample magnetization.[49, 50] The actual dependence is greater when it is realized that for larger samples the filling factor is better because the walls of the sample container are usually kept constant. However, we must balance the size of the pickup coil with the type of samples that we wish to study. Expensive or toxic samples may not be practical to use in large quantities. These considerations led to the spectrometer design described below.

## 2.3 The Spectrometer

In this section I will not attempt to describe the spectrometer in mechanical detail for that has been done before.[17, 18, 21] I do however want to give the reader a sense of the overall design and the method of operation for the experiments described in this thesis. There are some design and operational details that have been changed and I will discuss those in more detail.

### 2.3.1 Hardware Overview

Figure 2.7 shows an overall view of the SQUID spectrometer and Figure 2.8 presents a more detailed display of the lower portion of the SQUID spectrometer probe. The dc SQUID (BTi Model DP probe with Model DSQ DC Hybrid SQUID) is hermetically sealed inside a niobium shield. Two copper screws provide the means whereby the pickup coil leads can be attached to the coupling coil of the SQUID. The SQUID is connected to a room temperature feedback controller (BTi Model 400) which functions essentially as described above. The signal from the SQUID is passed through the feedback unit to the SQUID controller (BTi Model 40) where it is amplified (x1, x10, x100, x1000) and filtered (5 or 50 kHz bandwidth). That signal is then sent through a home built low-pass filter with a bandwidth from 200 to 0.02 Hz and a variable gain from 10 to 120. It is then transmitted into an AT clone computer through a digital oscilloscope (Rapid Systems Model R1000). The spectra can be stored and analyzed on the computer.

The pickup coil is supported on a macor form and is made of 10 turns of 0.5 cm diameter NbTi wire which is superconducting at liquid helium temperatures. Surrounding the pickup coil is a second form which contains two Helmholz rf coils. These two coils are orthogonal to one another and provide two channels of rf irradiation for the magnetic resonances experiments. They are connected to a programmable frequency sweeper (Hewlett-Packard 3326A Two Channel Synthesizer) which is also controlled by the AT clone computer. The sweeper can provide two separate rf channels for frequency sweeps of up to 13 MHz at an output level of up to 10 V with sweep times varying from 1 ms to 1000 s.

A third coil form supports a lead tube that is surrounded by a copper coil. Before the probe is cooled the copper coil is charged with current to produce a specific magnetic field (usually 10-150 Gauss). After the probe is placed in the liquid helium bath (4.2 K) the current is turned off. However, because the lead tube is now superconducting the

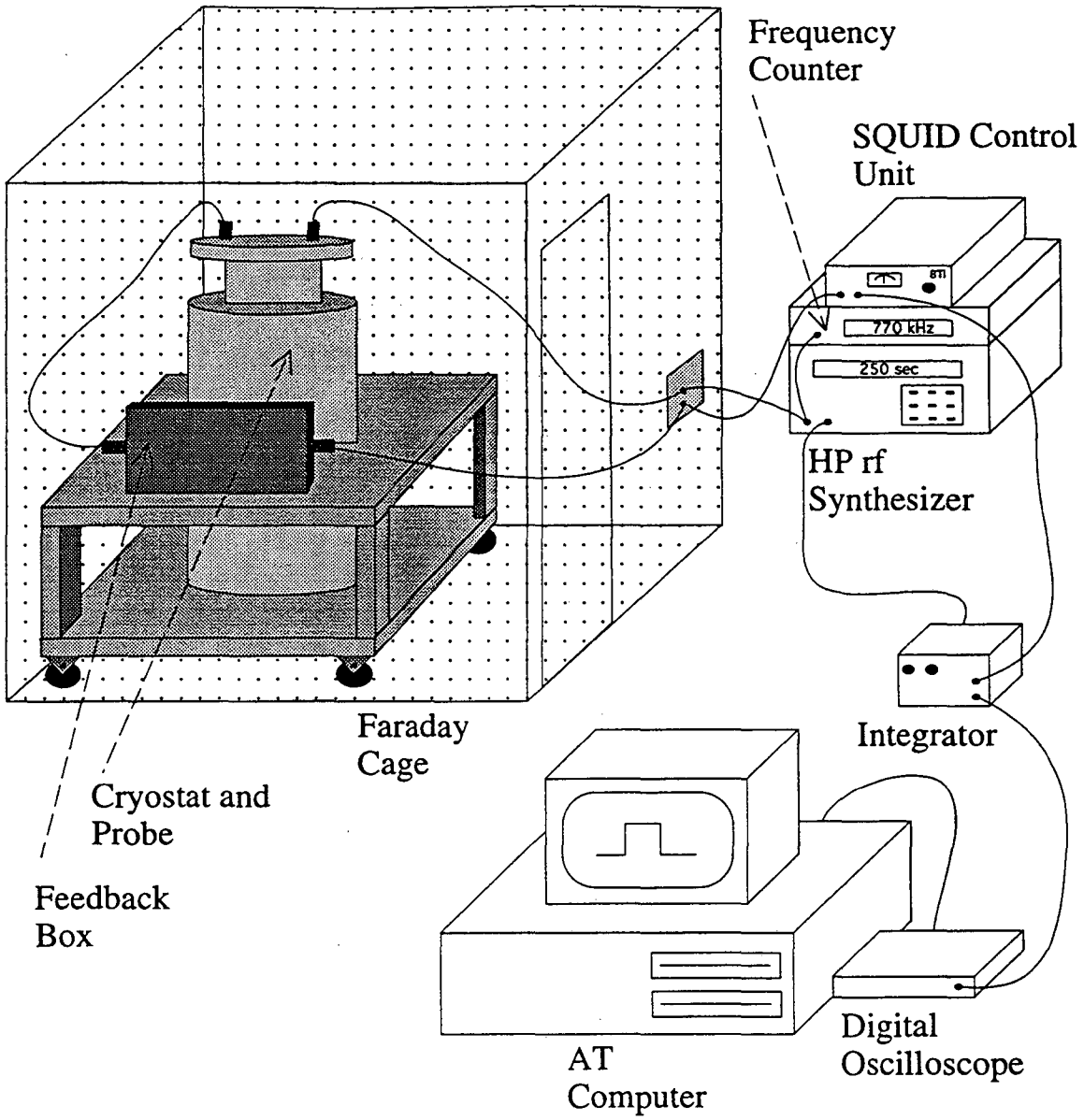


Figure 2.7. Schematic overview of the dc SQUID spectrometer.

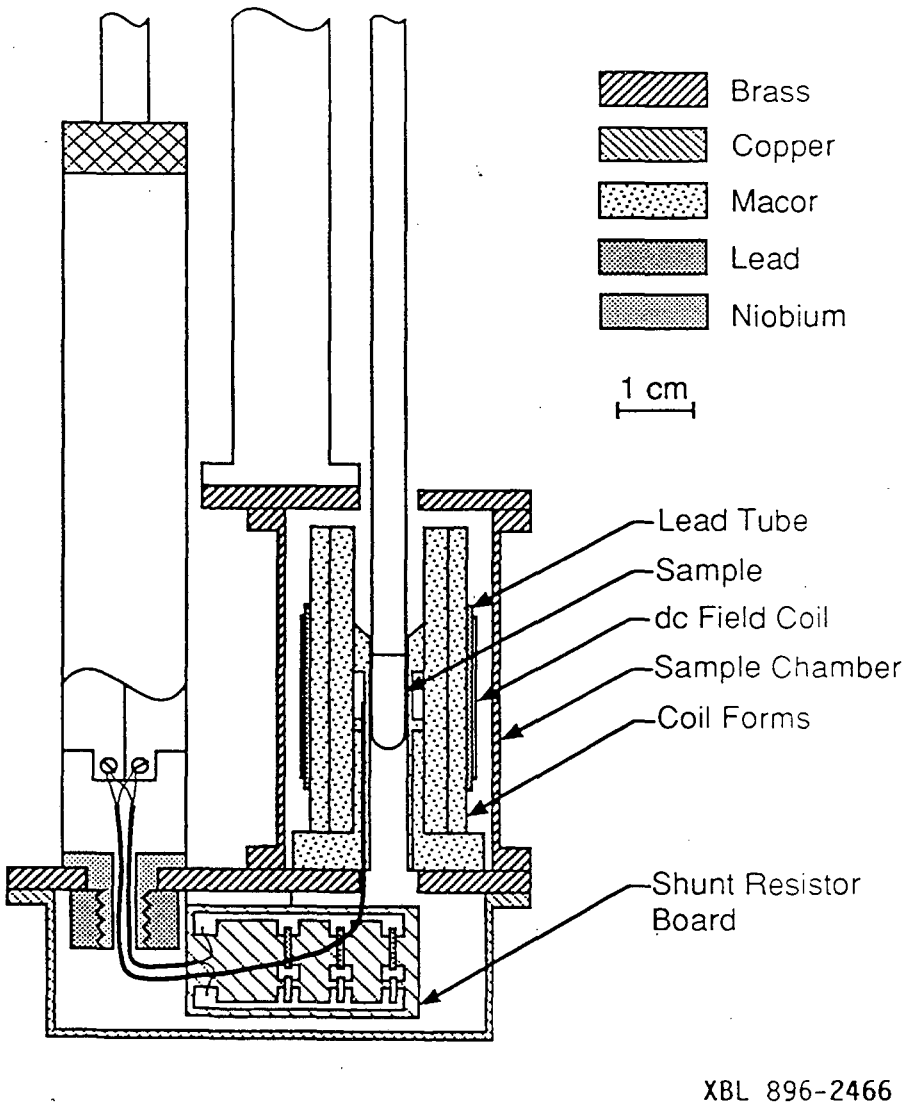


Figure 2.8. Cross-section of the low-temperature probe. The dc SQUID is on the left hand side.

magnetic field due to the previous current in the coil is kept constant (as described in Section 2.1.2). This provides a variable magnetic field of up to at least 300 Gauss. The field can be easily changed by lifting the probe slightly above the helium bath so that the lead tube is no longer superconducting, applying a new current to the copper coil, and returning the probe to the liquid helium where the lead tube is again superconducting. This seems to have no detrimental effect on the SQUID if it is turned off during this operation.

The rf field is on during detection and is coupled by mutual inductance into the pickup coil. Thus, a low pass filter must be used to eliminate the coupled rf and retain the signal (which is near dc).[51, 52] This places a limit on the rf frequency that can be used for irradiation. In this spectrometer, the rf must be greater than approximately 100 kHz to be effectively filtered. Also, a lead lined brass can surrounds the coil form, which serves as a superconducting filter of stray magnetic and rf fields.[53]

The entire probe is placed into a cryostat so that the SQUID, probe, and sample are all at 4.2 K. We now use a much larger and better cryostat which allows us to run the experiment for 10+ hours per helium fill.

## 2.3.2 Software Improvements

I have rewritten both the data acquisition and processing software to make it more user friendly with menus and better graphics. The data processing software can now display up to 10 spectra simultaneously for easy comparison. Also resonance frequencies can be read directly from the screen rather than manually calculated as before. The acquisition program also writes the sweep start and stop frequencies, sweep time, and rf strength onto the data file for reference during processing.

All this improves the data handling aspect of the experiment, but the biggest advances are in the actual control of the spectrometer. The software is now designed to use the second channel on the HP sweeper (when it is not needed for rf irradiation) to control

the output signal level by adjusting the dc offset of that signal. This allows the computer to maintain the signal within the range of the digital oscilloscope by resetting the dc offset after each scan, which had to be done manually before. We can now set the spectrometer to do multiple sweeps without constant human oversight. This allows for efficient averaging. Also, up to 20 different scans (with separate sweep parameters) can be run sequentially. The overall savings in time and effort for this experiment are significant.

### 2.3.3 Operation

In a typical experiment the sweep is usually between 100 to 500 kHz in length and 50 to 250 seconds in duration. We typically use around 3 volts of rf from the sweeper. This value is a compromise. We want to use as much rf as possible to completely saturate the resonance, but more rf means more noise. Also, the HP sweeper switches synthesizer switches circuits for voltages above 3 volts and this higher voltage circuit is much noisier. Three volts does however seem to be enough, as will be shown in the next chapter, to saturate most resonances.

There is also a two channel mode where two separate frequency sweeps can be initiated simultaneously. If the sweeps are over the same region circularly polarized rf can be produced. However, more useful is the simultaneous sweep over a frequency region while applying another specific irradiation frequency. This type of experiment is especially important in the double irradiation scheme presented for $^{14}N$ NQR (Section 5.3.4).

This spectrometer allows us to do many NMR and NQR experiments at low frequency and in low field that are normally very difficult to accomplish by other means. This advantage makes the SQUID spectrometer a valuable asset in the field of magnetic resonance.

# Chapter 3
# Z-Axis cw NMR and NQR

This chapter provides the basic theoretical description of the NMR and NQR techniques utilized in these experiments. More specialized theory and techniques will be discussed in chapters 5 and 6. I will begin by detailing the Hamiltonians that are used to describe the spin system, after which there will be a section on relaxation phenomena. The third part of the chapter will describe z-axis cw NMR and NQR detection. And, finally, there is a short discussion of experimental lineshapes and intensities. Table 3.1 is included as a reference to the relevant constants associated with the nuclei studied in this thesis.

## 3.1 Hamiltonians

Several Hamiltonians describe the basic interactions studied in NMR and NQR experiments. The first is the quadrupolar Hamiltonian which arises from the electrostatic interaction between an electric field gradient and the electric quadrupole moment of a nucleus. Such nuclei are non-spherical in shape and have a spin, I, greater than 1/2. This is the primary Hamiltonian in NQR. For NMR experiments the Zeeman Hamiltonian is the most important. It characterizes the interaction of the nuclear magnetic moment with an external magnetic field. For the experiments described in this thesis a magnetic field is applied even in the NQR case (which is atypical of most NQR techniques). Thus the Zeeman interaction is also present in our NQR experiments, although it is typically only a small but, as we will see, necessary perturbation of the quadrupolar Hamiltonian.

Two other Hamiltonians are also required to describe the experimental situation: the dipole-dipole Hamiltonian, which represents the interaction between the magnetic moments of neighboring nuclei, and the rf field Hamiltonian which characterizes the excitation of the

| Nucleus | Spin | Natural Abundance (%) | NMR Frequency at 1 Gauss (Hz) | Quadrupole Moment ($e \cdot 10^{-24}$ cm $^2$) |
|---|---|---|---|---|
| $^{1}H$ | 1/2 | 99.99 | 4258 | NA |
| $^{11}B$ | 3/2 | 80.1 | 1366 | +0.04065 |
| $^{14}N$ | 1 | 99.63 | 308 | +0.0156 |
| $^{23}Na$ | 3/2 | 100 | 1126 | +0.101 |
| $^{27}Al$ | 5/2 | 100 | 1109 | +0.140 |
| $^{51}V$ | 7/2 | 99.75 | 1119 | -0.052 |
| $^{55}Mn$ | 5/2 | 100 | 1050 | +0.40 |

Table 3.1 Properties of the nuclei discussed in this thesis.

nuclear spins by rf irradiation in order to detect signals. Each of these Hamiltonians will be described in the following sections.

### 3.1.1 The Quadrupolar Hamiltonian

The quadrupolar Hamiltonian arises from the interaction between the electric quadrupole moment of a nonspherical nucleus (one with I>1/2) and the surrounding electric field gradient as shown in Figure 3.1.[1] The bonding electrons are the typical source of the unsymmetric distribution of charge surrounding the nucleus which creates the electric field gradient.[3, 6, 54] Ions and other electric field anomalies, such as defects in the lattice, can also contribute. The quadrupolar interaction provides information about the local bonding configuration such as the coordination number, the symmetry of the molecular bonding, the symmetry of the lattice, and the effect of defects on the environment of the nucleus. Non-crystalline structures such as those in glasses can also be studied.[55, 56]

The electric field gradient, $V_{ab}$ (where a, b = x, y, or z), is typically described in terms of a principal axis system, which is defined such that all off-diagonal terms are zero and $V_{zz} > V_{yy} > V_{xx}$. The magnitude of the electric field gradient, eq, is designated as

$$eq = V_{zz} \qquad 3.1$$

and the asymmetry parameter, $\eta$ , as

$$\eta = \frac{V_{xx} - V_{yy}}{V_{zz}}. \qquad 3.2$$

When this is combined with the Laplace equation,

$$V_{zz} + V_{yy} + V_{xx} = 0, \qquad 3.3$$

the value of $\eta$ is restricted to the range between 0 and 1.

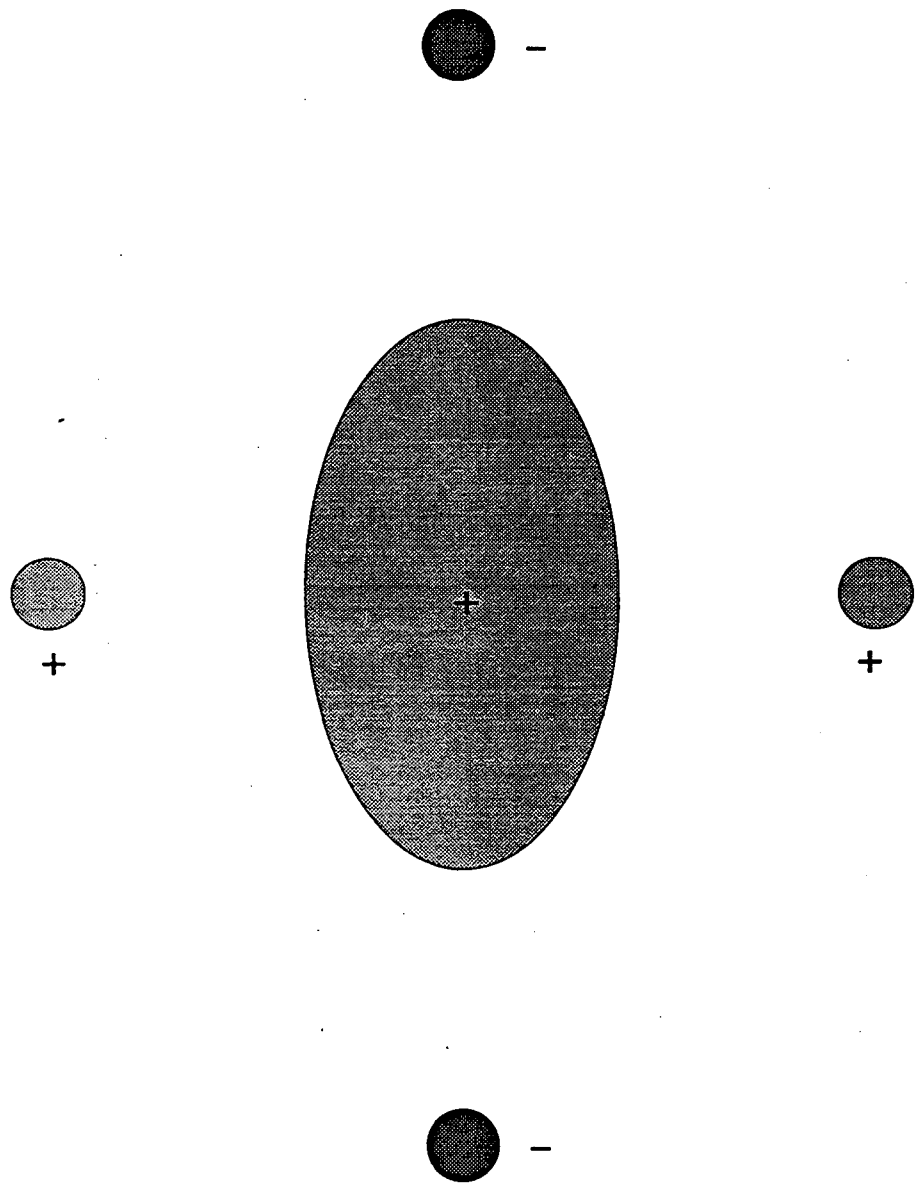


Figure 3.1 A nonspherical quadrupolar nucleus (center) has a preferred orientation in an electric field gradient. This gradient is usually due to the unsymmetrical distribution of bonding electrons, but can also arise from nearby ions and defects.

$\eta$ characterizes the degree of symmetry of the electric field gradient. If $\eta$ equals zero then the z-axis has $C_3$ or better symmetry.[2] If $\eta$ equals 1 then $V_{xx} = 0$ and the electric field gradient is limited to the zy plane with the symmetry of the color group, $C_4$. If there are two perpendicular $C_3$ or better symmetry axes then $V_{zz} = V_{yy} = V_{xx} = 0$ and thus no electric field gradient. One of the well-known cases for such an occurrence is the cubic lattice such as in NaCl. There is no quadrupolar interaction for sodium or chlorine in this sample except where the material deviates from perfect cubic symmetry, such as near a defect site.

The quadrupolar Hamiltonian can be written in its principal axis system as

$$H_Q = \frac{e^2qQ}{4I(2I-1)}[3I_z^2 - I^2 + \frac{\eta}{2}(I_+^2 + I_-^2)], \qquad 3.4$$

where eQ is the electric quadrupole moment of the nucleus. Typical energy level diagrams are displayed in Figures 3.2 and 3.3. Figure 3.2 presents a half odd integer spin system, in this case I = 7/2, but a similar diagram can be drawn for I = 3/2, 5/2,... In all cases the energy levels are doubly degenerate in zero field. Figure 3.3 shows the I = 1 energy level diagram. Again a similar diagram can be drawn for I = 2, 3,... Integer spin energy levels are only degenerate when $\eta = 0$. All nondegenerate levels for integer spin nuclei have a vanishing magnetic moment as indicated in the spin-1 energy level diagram.[57] This presents an important problem for the direct detection of integer spin NQR signals by the SQUID spectrometer which will be discussed in detail in Chapter 5.

$\frac{e^2qQ}{h}$ is commonly referred to as the quadrupole coupling constant ($C_Q$) and describes the strength of the quadrupolar interaction. $\eta$ and $C_Q$ are the two parameters that are calculated from the quadrupolar resonances and completely characterize the electric field gradient. Figures 3.4 and 3.5 plot the relative splittings expected for nuclei with I=3/2, 5/2, 7/2, 9/2, and 1 as a function of $\eta$.

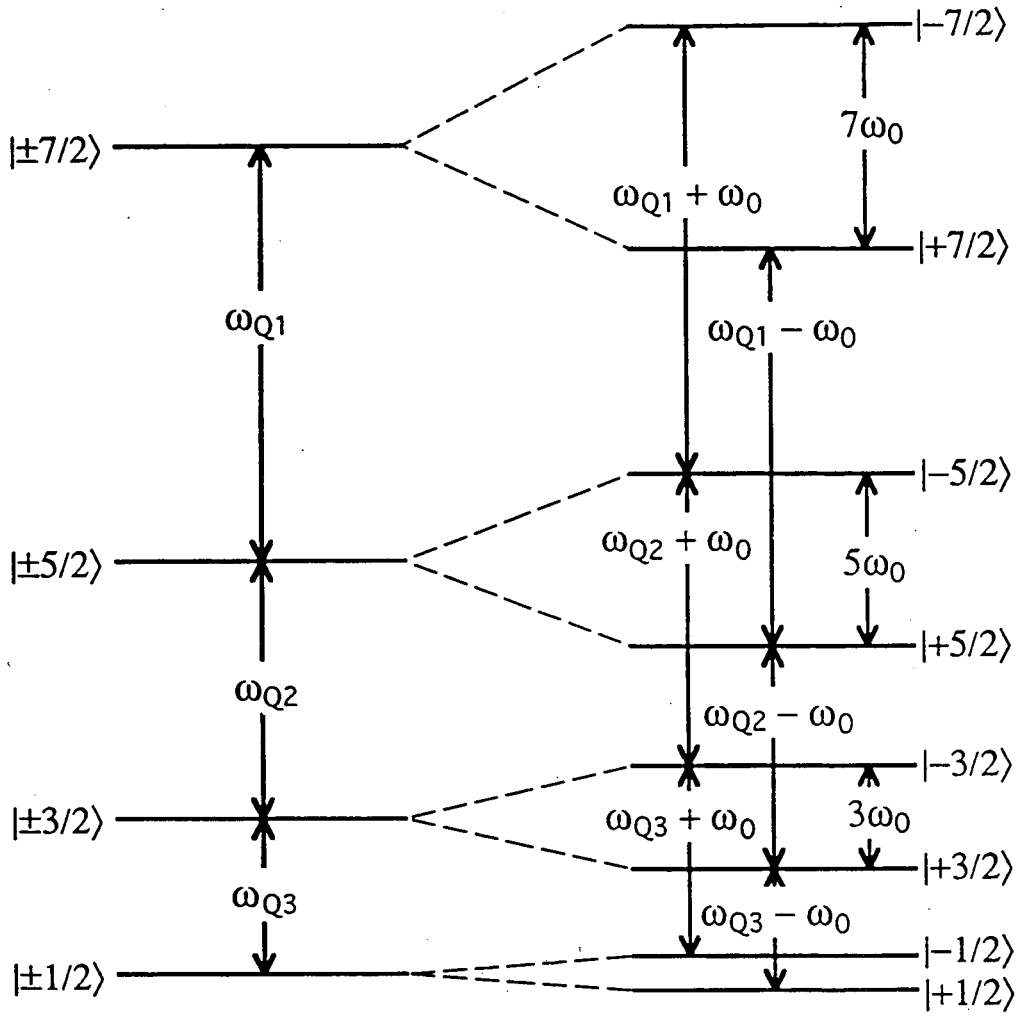


Figure 3.2. The energy level diagram for a spin 7/2 nucleus in both zero (left) and nonzero (right) magnetic fields. The $\omega_Q$'s are the quadrupolar frequencies, which in this case must be numerically calculated from the quadrupolar parameters, $C_Q$ and $\eta$ . $\omega_0$ is the Zeeman splitting, $\gamma\hbar B_0$. Similar diagrams can be made for I = 3/2, 5/2, ... nuclei.

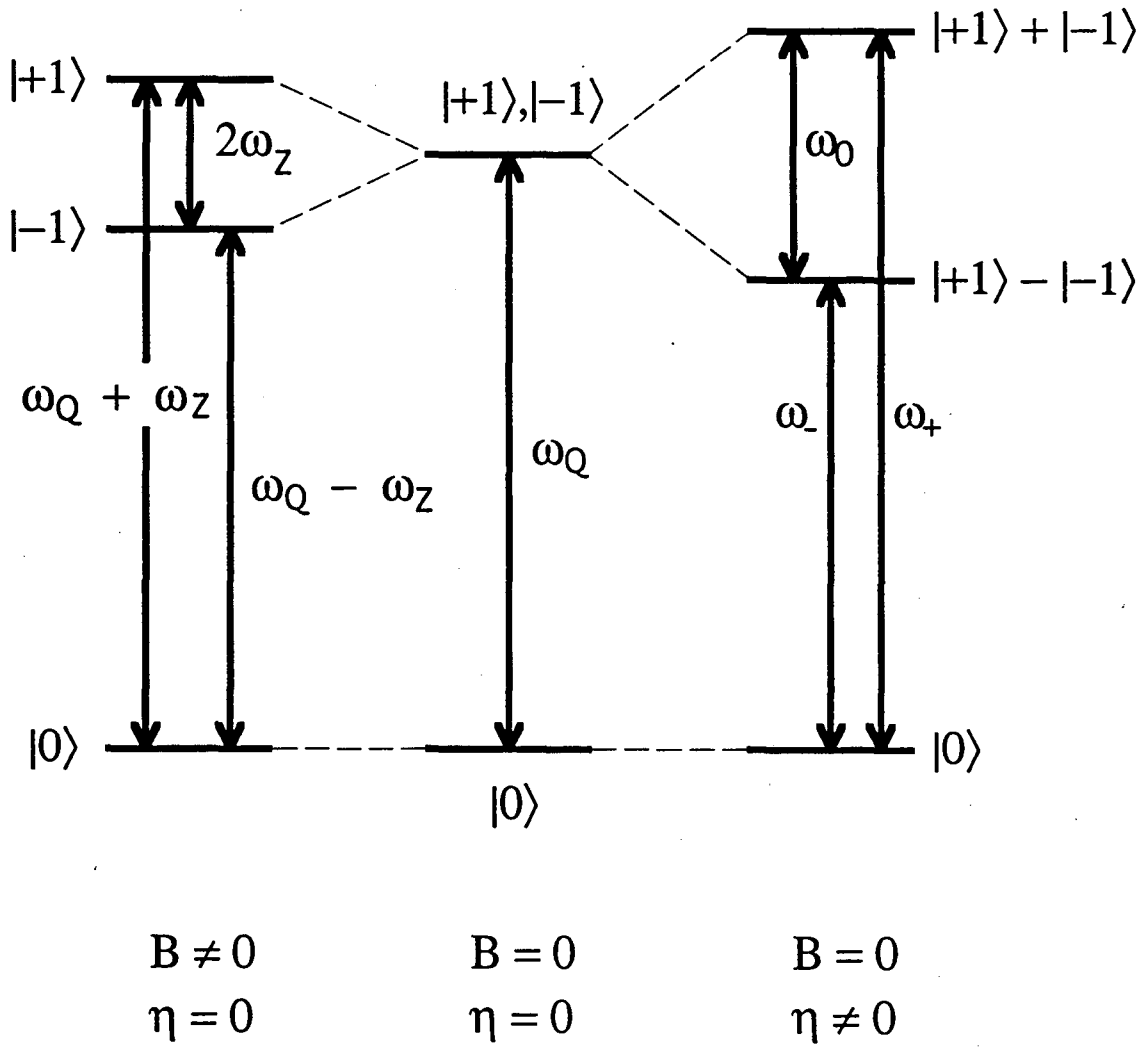


Figure 3.3. Energy level diagram for a spin-1 nucleus. Note that for the case where $\eta \neq 0$ all states have zero longitudinal magnetization.

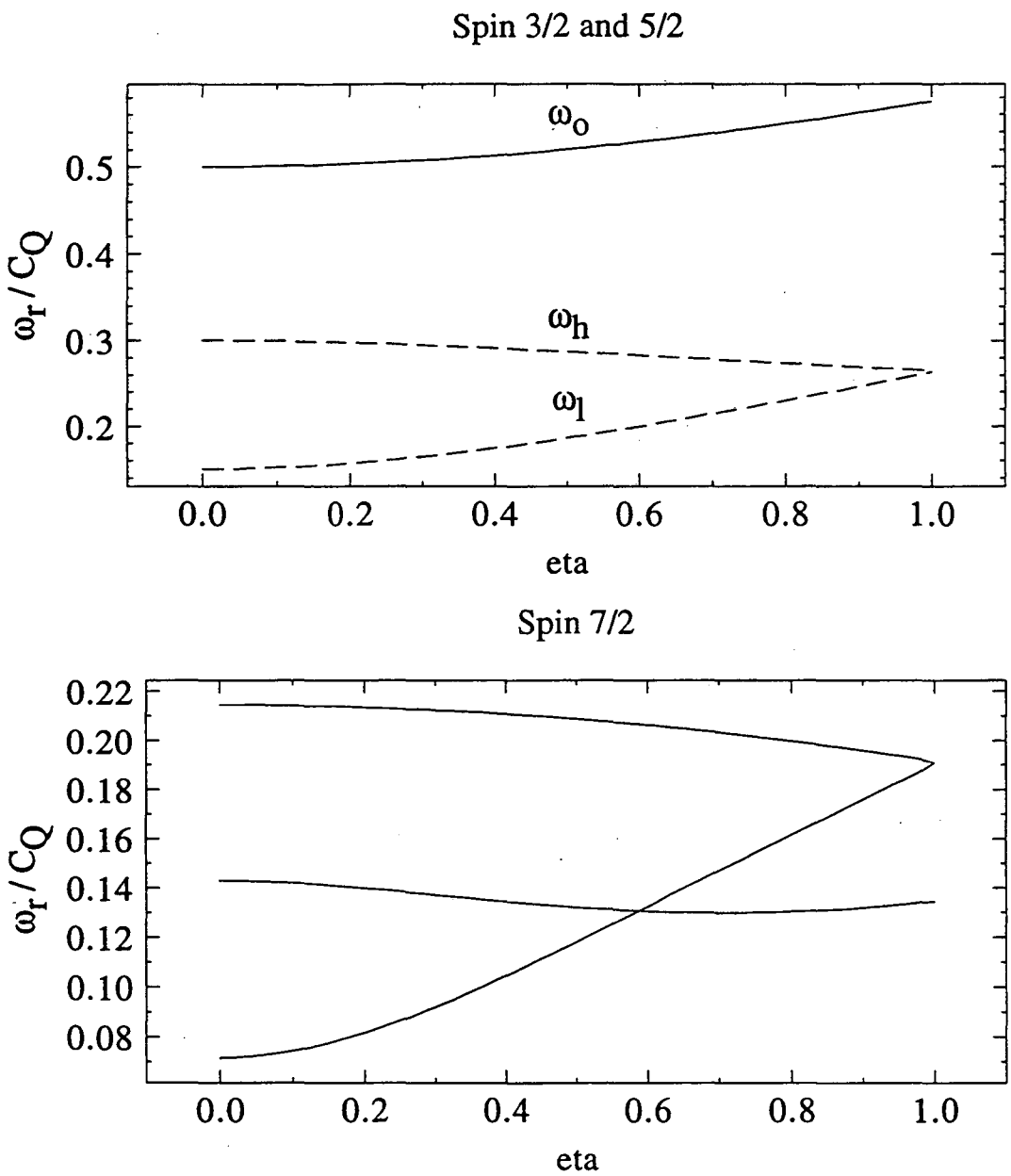


Figure 3.4. Plot of the relative splittings for resonance frequencies, $\omega_r$,with respect to the quadrupolar coupling constant, $C_Q$, as a function of $\eta$ for nuclei with I = 3/2, 5/2, and 7/2. In the top graph the solid line represents the single transition for the I = 3/2 case and the dotted lines characterize I = 5/2 nuclei.

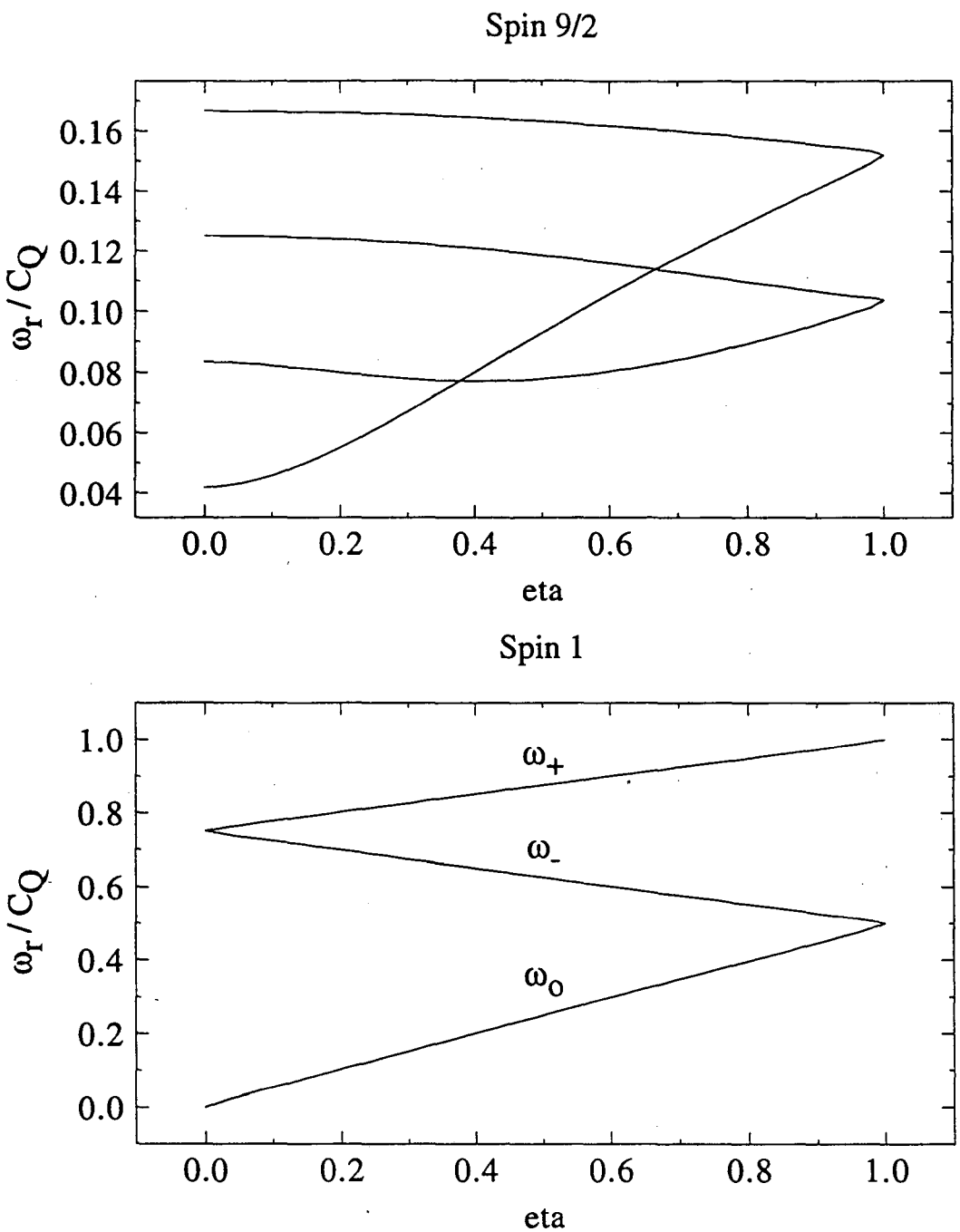


Figure 3.5. Plot of the relative splittings for resonance frequencies, $\omega_r$,with respect to the quadrupolar coupling constant, $C_Q$, as a function of $\eta$ for nuclei with I = 9/2 and 1.

The two quadrupolar parameters provide information about the surroundings of the nucleus. A detailed quantum electronic treatment would be necessary for an accurate calculation of these parameters, but at this time the precision of these calculations is not great enough for quantitative predictions. However, from the magnitudes of these two parameters we can obtain information such as the symmetry around the nucleus, the size of the deviation from a specified lattice symmetry, paramagnetism (paramagnetic atoms usually have a much larger $C_Q$), coordination number, the effect of impurities and lattice defects, and the distribution of sites in an amorphous material.

Although the electric quadrupole moments of most nuclei vary over only about 2 orders of magnitude, the quadrupolar frequencies can vary from less than 10 kHz to hundreds of MHz. The large quadrupolar frequencies are typically found for nuclei with very polarizable electrons, such as the halogens, or paramagnetic atoms, which include many transition metal compounds. As mentioned in Chapter 1, the SQUID is used to study NQR at the low frequency end of this range. This is the region for nuclei such as $^{11}B$, $^{14}N$, $^{23}Na$, $^{27}Al$, and nonparamagnetic transition complexes involving nuclei such as $^{51}V$ and $^{55}Mn$. The spectrometer could also be used to study slight deviations from cubic symmetry such as chlorine near defect sites in NaCl.

## 3.1.2 The Zeeman Hamiltonian

The Zeeman Hamiltonian describes the interaction between the nuclear magnetic moment and an external magnetic field. This is the principal Hamiltonian for NMR. In our NQR experiments the Zeeman interaction will serve as a perturbation of the pure quadrupolar Hamiltonian. For NMR, we write the Zeeman Hamiltonian as

$$H_z = -\gamma\hbar I_z B_0 \qquad 3.5$$

where $\gamma$ is the gyromagnetic ratio of the specific nucleus and $B_0$ is the applied magnetic field. This determines the z axis of the nuclear spin.

For our study of NQR, the Zeeman interaction is smaller than the quadrupolar interaction, so we must rewrite the Zeeman Hamiltonian in the principle axis system of the quadrupolar interaction:

$$H_z = -\gamma\hbar B_0(I_z\cos\theta + I_x\sin\theta\cos\phi + I_y\sin\theta\sin\phi). \qquad 3.6$$

The angles $\theta$ and $\phi$ relate the magnetic field axis to the quadrupolar principle axis system.

The Zeeman interaction alone provides no information. Rather, quantities such as the chemical shift of the Zeeman line are studied. In our experiments we use such small fields that this shift would be less than 10 Hz for protons, much too small to be resolved by this spectrometer. Instead we use the magnetic field primarily to split degenerate transitions. This will be discussed further in the section on NQR detection in this chapter as well as in Chapter 6 on methyl quantum tunneling. We also use the Zeeman interaction to match transitions of different nuclei. This application will be discussed further in Chapter 5 on $^{14}N$ NQR.

## 3.1.3 The Dipolar Hamiltonian

The dipole-dipole interaction describes the coupling between a nuclear spin and the magnetic moments of neighboring nuclei.[58] The strength of the interaction depends on the distance between the nuclei and their gyromagnetic ratios as shown in the Hamiltonian, $H_d$, which is written in terms of spherical coordinates related to the Zeeman or quadrupolar principle axis system as

$$H_d = \frac{\gamma_1\gamma_2\hbar^2}{r^3}(A+B+C+D+E+F) \qquad 3.7$$

where

$$A=(1 - 3\cos^2\theta)\, I_{1z}I_{2z}, \qquad 3.8a$$

$$B = -\frac{1}{4}(1 - 3\cos^2\theta)\,(I_1^+I_2^- + I_1^-I_2^+), \qquad 3.8b$$

$$C = -\frac{3}{2}\sin\theta\cos\theta\, e^{-i\phi}\,(I_1^+I_{2z} + I_{1z}I_2^+) \qquad 3.8c$$

$$D = -\frac{3}{2}\sin\theta\cos\theta\, e^{i\phi}\,(I_1^-I_{2z} + I_{1z}I_2^-) \qquad 3.8d$$

$$E = -\frac{3}{4}\sin^2\theta\, e^{-2i\phi}\,(I_1^+I_2^+) \qquad 3.8e$$

$$F = -\frac{3}{4}\sin^2\theta\, e^{2i\phi}\,(I_1^-I_2^-). \qquad 3.8f$$

The dipolar interaction can involve nuclei of the same (homonuclear) or of different (heteronuclear) types. If there is more than one neighboring nucleus with a dipole moment near the atom of interest, the dipolar interaction can be calculated for each case separately and summed for the total effect.

The dipolar Hamiltonian provides the major contribution to line broadening in NMR spectra and, along with the Zeeman interaction, in NQR spectra. The dipolar Hamiltonian is weaker than either of the two previous interactions in the experiments described in this work. For our proton NMR experiments it is about 5-10% of the strength of the typical Zeeman interaction. This is significantly different from the normal high field NMR experiments where the dipolar interaction is many orders of magnitude smaller than the Zeeman term. In that case only the "A" and "B" terms of the homonuclear and "A" term of the heteronuclear dipolar Hamiltonian are considered. These are known as the secular terms and describe energy conserving transitions. However, in our experiments the other terms can not be ignored and provide a driving force for several of the experiments in this thesis.

The "B" term of the dipole-dipole Hamiltonian is often called the flip-flop term. It describes an energy conserving transition if the nuclei are of the same type or if two different nuclei meet the level matching condition (see Chapter 5). This provides for efficient cross-relaxation and spin diffusion. The "C"-"F" terms allow mixing between

states that would be isolated in high field. This is especially important in the methyl tunneling experiments (Chapter 6) where the dipole-dipole coupling makes transitions between states of different symmetry slightly allowed. These tunneling transitions are forbidden in high field.

### 3.1.4 rf Irradiation

rf irradiation provides the means for the detection of NMR and NQR signals. As rf is swept through resonance, the irradiation causes spins to be excited from the more populated to the less populated state thereby inducing a change in the net magnetization of the sample. The Hamiltonian for linearly polarized rf along the x-axis of a principle axis system is

$$H_1 = -\gamma\hbar B_1 I_x \cos(\omega t). \qquad 3.9$$

where $\omega$ is the frequency of the rf field and $B_1$ is its strength. For circularly polarized rf the proper form is

$$H_1 = -\gamma\hbar B_1 (I_x \cos(\omega t) \pm I_y \sin(\omega t)) \qquad 3.10$$

where the sign of $I_y$ determines the direction (right or left) of circular polarization.

## 3.2 Relaxation

Relaxation effects also must be understood in order to characterize the spectra obtained in these experiments, especially in the case of $^{14}N$ NQR where it turns out to be a very important part of the detection scheme. Relaxation is usually not treated as a Hamiltonian operator, but rather as a decay process with a characteristic decay time, $T_1$ (spin-lattice relaxation) or $T_2$ (spin-spin relaxation). Although the relaxation processes in

these experiments are not strictly exponential we approximate them as such as that is good enough for our purposes.

### 3.2.1 Spin-lattice Relaxation

Relaxation between the spins and the lattice returns the entire spin system to the lattice equilibrium temperature, the typical starting point for magnetic resonance experiments. This process causes a change in the sample's longitudinal magnetization,[58] therefore the decay time, $T_1$, can be measured easily by the SQUID. An experimental example of this decay is shown in Figure 3.6.

$T_1$ determines how often the resonance can be swept for the spins must relax back to equilibrium in order to obtain the maximum signal intensity. This usually requires waiting for $5T_1$ between experiments. Herein lies one of the greatest limitations of the spectrometer. Many samples, especially inorganics, have $T_1$'s of tens of minutes to hours or longer at 4.2 K. Waiting for these samples to relax is impractical. One solution to this dilemma is to put the sample in a variable temperature container. Then the temperature can be raised to a point where the spin-lattice relaxation time is sufficiently short for the experiment to be practical. However, the signal intensity is inversely proportional to the equilibrium temperature so a sample at 77 K would have a signal approximately 18 times less intense than the same material at 4.2 K. At the present time most resonance signals would be lost in the noise at 77K. But with improvements in the detection circuitry and the sensitivity of the SQUID, we may overcome this problem.

On the other hand if $T_1$ is very short compared to the sweep time, the signal intensity is decreased because spins relax almost as fast as they are excited. This we have observed for some organic glasses, such as toluene which has been rapidly quenched to 4.2K.

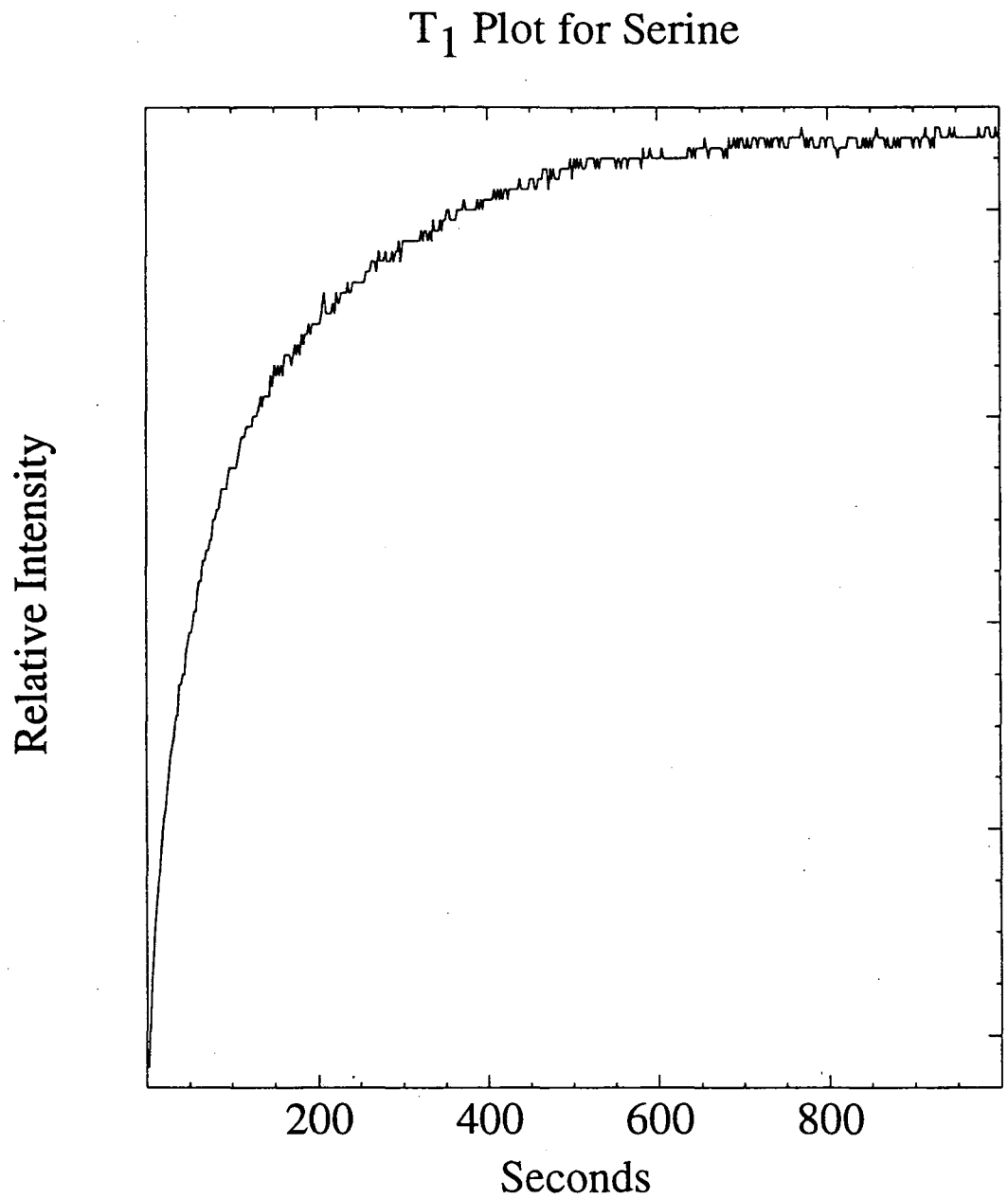


Figure 3.6. A sample relaxation decay of the protons in L-serine at 4.2 K.

The ideal sample for this spectrometer would be one with $T_1$ on the order of the sweep time of the experiment. This would allow for efficient signal averaging, but the lineshape of the resonance would not be significantly altered by ongoing relaxation (as discussed in section 3.5).

Fortunately, many interesting samples fit our $T_1$ requirements. Among these are organic molecules with methyl groups. The motion of the methyl group is enough to provide a convenient mechanism for coupling between the spin bath and the lattice. Also, all the borate glasses we have examined have had short $T_1$'s. Thus despite the limitations there are still many interesting samples to be investigated.

### 3.2.2 Spin-spin Relaxation (Cross-relaxation)

Spin-spin relaxation is the process whereby the spins exchange energy amongst themselves. I wish to focus here on cross-relaxation, or spin diffusion, which is an energy conserving process that involves mutual transitions of two or more spins.[59, 60] Cross-relaxation takes place between two levels that are close to or exactly in resonance with each other. The dipole-dipole interaction facilitates this transfer in polarization. In the case of NMR, spin diffusion is accomplished by the "B" or so called "flip-flop" term of the dipole-dipole Hamiltonian. It involves an exchange in polarization between two spins with no net change in magnetization.

Another type of cross-relaxation is depicted in Figure 3.7 between two quadrupolar nuclei with I = 3/2. In this case the "E" and "F" terms of the dipolar interaction facilitate this exchange.[58] This type of cross-relaxation is important for NQR of half odd integer spin nuclei. The zero field transitions are doubly degenerate so cross-relaxation is energy conserving. In this case there is no net change in magnetization and therefore nothing for the SQUID to detect, despite irradiation of the transitions. Thus a magnetic field is necessary to separate the resonance frequencies.[36] When a field is added, the two

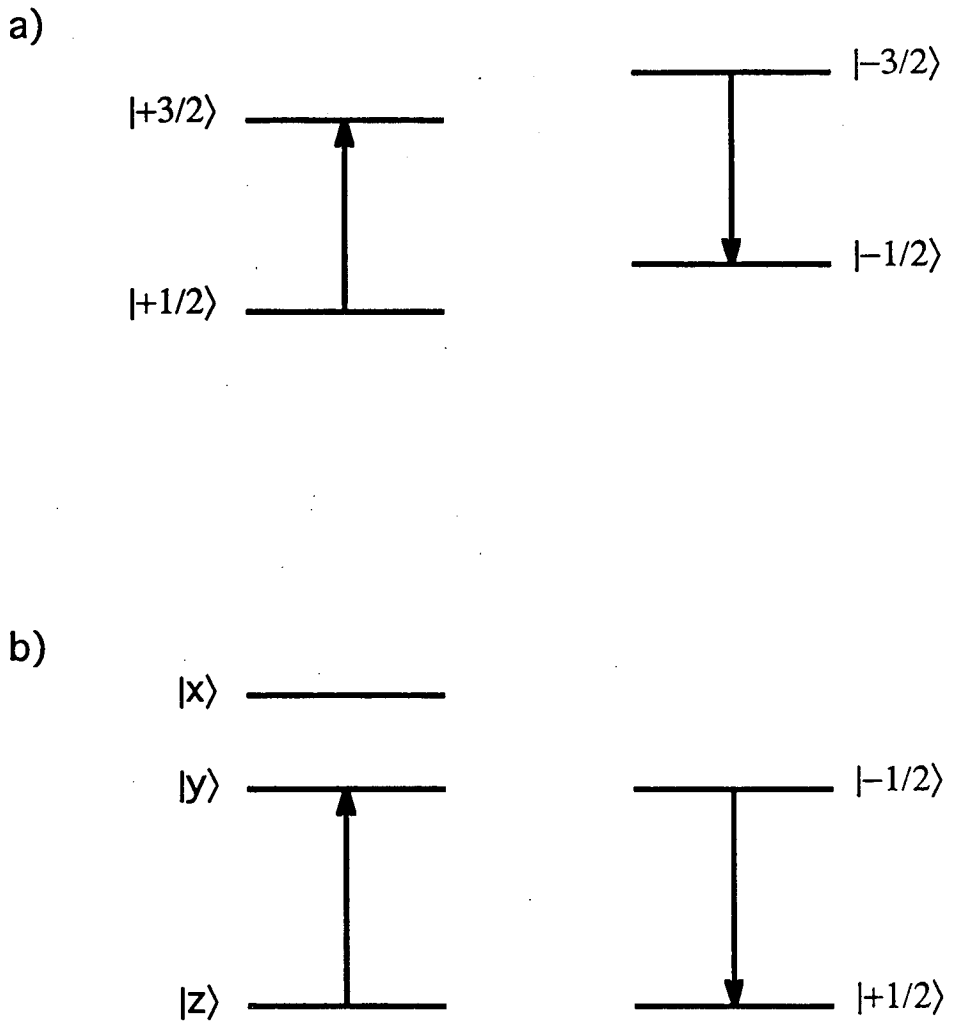


Figure 3.7. Samples of cross-relaxation between a) quadrupolar states, mediated by the "E" and "F" terms of the homonuclear dipole coupling, and b) a quadrupole nucleus (I=1) and Zeeman split states of a spin-1/2 system, promoted by the "B" term of the heteronuclear dipolar Hamiltonian.

previously degenerate transitions now become $\omega_Q \pm \omega_z$ (for a single crystal sample) where $\omega_Q$ is the quadrupolar frequency and $\omega_z$ is the Zeeman splitting. Cross-relaxation is no longer energy conserving. This solution, however, is limited for powder samples, because the signal intensity will be spread over the entire region from $\omega_Q - \omega_z$ to $\omega_Q + \omega_z$. For these samples one must balance the decrease in cross-relaxation versus the decrease in intensity caused by the spreading of the signal over a wide frequency range.

The final type of cross-relaxation that I wish to address is that between two different nuclei. This is especially important for our $^{14}N$ experiments as will be described in detail in Chapter 5. If conditions are such that energy level splittings for two different nuclei are equal, we have what we call a level matching condition. This situation is shown in Figure 3.7 for the quadrupolar splitting of $^{14}N$ and the Zeeman splitting of $^{1}H$. This condition is easily met by simply applying a magnetic field such that the proton splitting is exactly equal to a $^{14}N$ quadrupolar transition frequency. Cross-relaxation occurs between the protons and nitrogens via the heteronuclear dipole-dipole coupling provided that the atoms are in close proximity to each other. In this case, a net magnetization change in the sample (from the protons) occurs during cross-relaxation which provides the basis for detecting $^{14}N$ resonances.

## 3.3 Z-axis cw Magnetic Resonance

### 3.3.1 Single Crystal NMR (I=1/2)

To describe z-axis cw NMR, I begin with the simplest case, that of a single crystal with isolated (no dipolar coupling) spin-1/2 nuclei in a magnetic field.[50] I will also ignore relaxation effects.

This is a simple two level system as depicted in Figure 3.8 with an energy splitting of $\hbar\omega_z$. The populations of the two levels, using the high temperature approximation, are

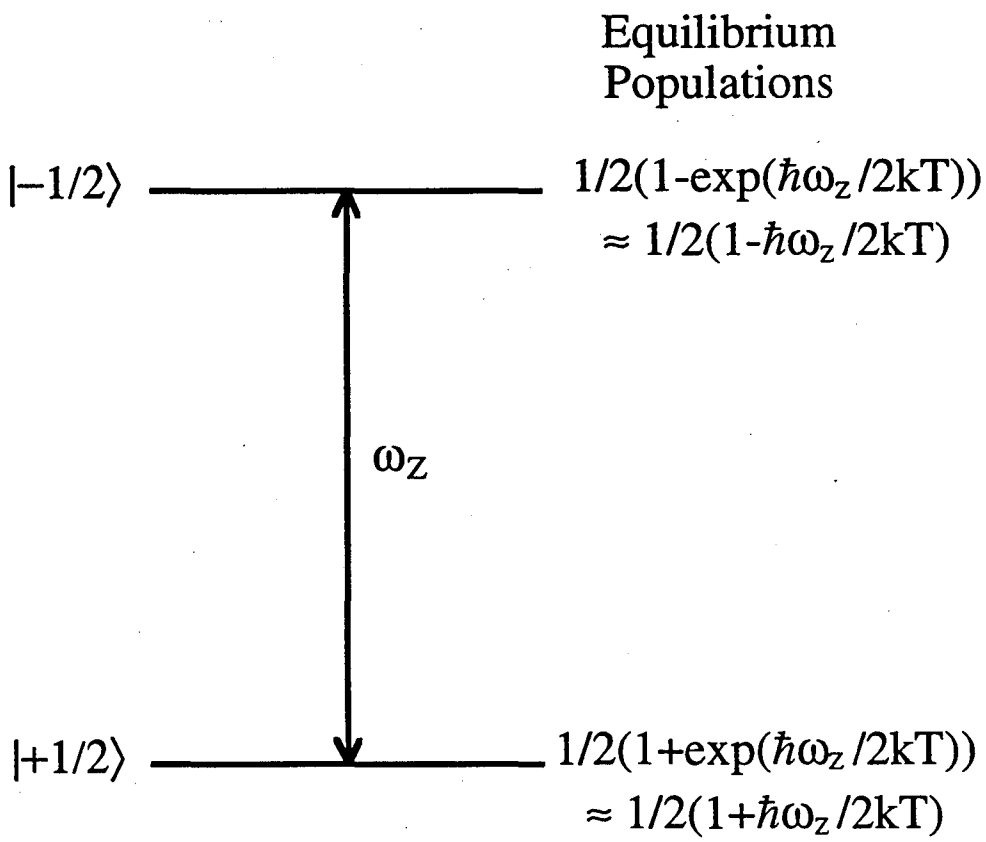


Figure 3.8. Energy level diagram and equilibrium populations of a spin-1/2 nucleus in a magnetic field, $B_0 = \frac{\omega_z}{\hbar\gamma}$.

$$P_{-1/2} = \frac{1}{2}(1 - \frac{\hbar\omega_z}{2kT}) \qquad 3.11a$$

$$P_{+1/2} = \frac{1}{2}(1 + \frac{\hbar\omega_z}{2kT}). \qquad 3.11b$$

The longitudinal magnetization of the sample can be calculated by summing the products of the populations of each level multiplied by its respective $I_z$ value,

$$M_z = N\gamma\hbar \sum_i (P_i I_{zi}) \qquad 3.12$$

where N is the number density of the spins. For this case ,

$$M_z = \frac{N\gamma\hbar^2\omega_z}{4kT}. \qquad 3.13$$

The SQUID will measure the change in sample magnetization as rf is swept through resonance. Under ideal saturating conditions the populations of the two levels will equalize,

$$P_{-1/2} = P_{1/2} = \frac{1}{2}. \qquad 3.14$$

This will leave a longitudinal magnetization value of

$$M_z = 0. \qquad 3.15$$

Therefore, the net change in magnetization that the SQUID measures is

$$\Delta M_z = \frac{N\gamma\hbar^2\omega_z}{4kT}. \qquad 3.16$$

This is shown in Figure 3.9 as a single step at the resonance frequency.

Several factors distort this idealized spectrum. Dipole-dipole coupling to nearby nuclei will split the line and provide a manifold of states about the original energy level.[61] These separate splittings are typically not seen due to efficient cross relaxation and overlap

Theoretical Single Crystal Signals

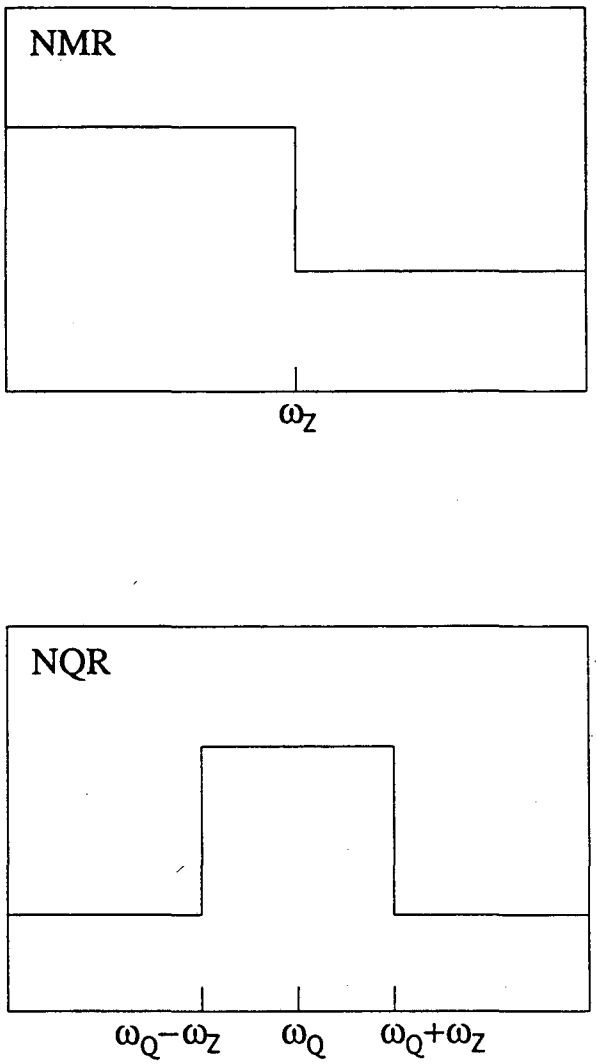


Figure 3.9. Simple theoretical examples of single crystal NMR and NQR spectra. The quadrupolar resonance frequency of the NQR example is calculated by simply averaging the frequencies of the two transitions.

between the dipolar split states. Also, spin lattice relaxation will be manifest as a return to the original equilibrium value of magnetization if the spin-lattice relaxation time, $T_1$, is of the same order or shorter than the sweep time. This is one of the primary reasons why it is necessary to combine equal numbers of sweeps in different directions (high to low frequency and low to high frequency) in order to avoid biasing the spectrum and the resulting experimental resonance frequency by the direction of the sweep.

## 3.3.2 Half Odd Integer Spin Single Crystal NQR

As shown in Figure 3.2 , the ±m states in these systems are degenerate in the absence of a magnetic field. If transitions are excited in this situation we would find no signal because both transitions would be simultaneously irradiated with a net change in longitudinal magnetization of zero. For this reason a magnetic field is applied. The field splits the two transitions by an amount proportional to the field strength. Each resonance can then be separately excited.

For a detailed example let's look at a spin-3/2 nucleus with an axially symmetric electric field gradient ($\eta = 0$) as depicted in Figure 3.10.[1, 62] The energy levels in this system are

$$E_{\pm 3/2} = \frac{e^2qQ}{4} \mp 3/2(\gamma\hbar B_0) \qquad 3.17a$$

$$E_{\pm 1/2} = -\frac{e^2qQ}{4} \mp 1/2(\gamma\hbar B_0) \qquad 3.17b$$

with NQR resonances at $\omega_{Q,\mp n} = \omega_Q \pm \omega_z$ where $\omega_Q = \frac{e^2qQ}{\hbar}$ and $\omega_z = \gamma B_0$.

The equilibrium populations of the spin states, applying the high temperature approximation,[58] are

$$P_{-3/2} = \frac{1}{4}(1 - \frac{\hbar\omega_Q}{4kT} - \frac{3\hbar\omega_z}{2kT}), \qquad 3.18a$$

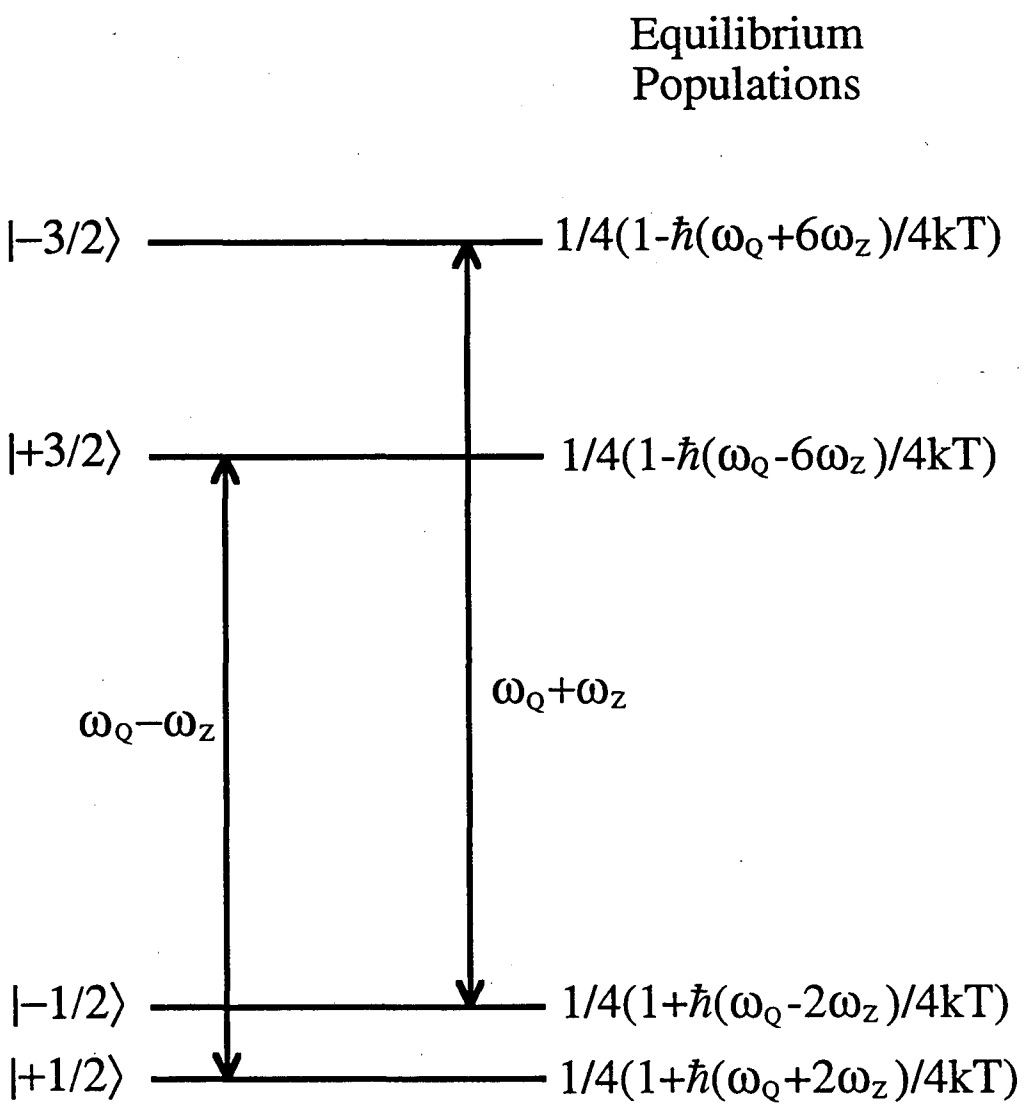


Figure 3.10. Energy level diagram and equilibrium populations of a spin-3/2 nucleus in a magnetic field, $B_0 = \frac{\omega_z}{\hbar\gamma}$.

$$P_{+3/2} = \frac{1}{4}(1 - \frac{\hbar\omega_Q}{4kT} + \frac{3\hbar\omega_z}{2kT}), \qquad 3.18b$$

$$P_{-1/2} = \frac{1}{4}(1 + \frac{\hbar\omega_Q}{4kT} - \frac{\hbar\omega_z}{2kT}), \qquad 3.18c$$

$$P_{+1/2} = \frac{1}{4}(1 + \frac{\hbar\omega_Q}{4kT} + \frac{\hbar\omega_z}{2kT}). \qquad 3.18d$$

At thermal equilibrium the total magnetization of the sample is, according to equation 3.12,

$$M_z = \frac{N\gamma\hbar^2}{4kT}\frac{10\omega_z}{2}. \qquad 3.19$$

For any half odd integer spin system equation 3.19 generalizes to

$$M_z = \frac{N\gamma\hbar^2}{(2I+1)kT}\omega_z \sum_i m_i^2. \qquad 3.20$$

As rf is swept from low to high frequency, it first saturates the +1/2 → +3/2 transition resulting in an equalization of the populations of those two levels,

$$P'_{+3/2} = P'_{+1/2} = \frac{1}{4}(1 + \frac{\hbar\omega_z}{kT}). \qquad 3.21$$

The longitudinal magnetization is now

$$M'_z = \frac{N\gamma\hbar^2}{4kT}(\frac{9\omega_z}{2} + \frac{\omega_Q}{4}) \qquad 3.22$$

which generalizes for any transition, m → m ± 1 (except +1/2 → -1/2 which is not a quadrupolar transition) as

$$M'_z = \frac{N\gamma\hbar^2}{(2I+1)kT}(\left(\sum_i m_i^2 - 1/2\right)\omega_z + \frac{6m \pm 3}{8I(2I-1)}\omega_Q) \qquad 3.23$$

where $\omega_Q$ is the frequency of the quadrupolar resonance excited. Because $\omega_Q$ is much larger than $\omega_z$ a dramatic change in the sample magnetization occurs when an NQR transition is excited.

As the sweep continues through the -1/2 → -3/2 transition and equalizes the populations of those two levels, the final magnetization is found to be

$$M_z'' = \frac{N\gamma\hbar^2}{4kT}\frac{8\omega_z}{2}. \qquad 3.24$$

Again this generalizes to

$$M_z'' = \frac{N\gamma\hbar^2}{(2I+1)kT}\,\omega_z(\sum_i m_i^2 - 1). \qquad 3.25$$

There is also a change in the magnetization on the order of $\omega_Q$ but now in the opposite direction of the first transition. These calculations lead directly to the theoretical signal shown in Figure 3.9. The quadrupole frequency is then simply the average of the two transition frequencies. Note that this theoretical signal is also broadened and changed by the dipolar couplings and relaxation effects as described in the previous section.

## 3.3.3. Integer Spin NQR

There is a very fundamental problem when one is working with integer spin nuclei. Nondegenerate quadrupole levels have no longitudinal magnetization in zero field.[57] This is easily seen in the case of the spin-1 nucleus. When $\eta = 0$ the $|\pm 1\rangle$ levels are degenerate and split from the $|0\rangle$ level by the quadrupolar coupling constant. This is similar to the previous case and we can use a magnetic field to split the levels and obtain the quadrupolar information. However when $\eta \neq 0$ then the two levels split into what we call the $|x\rangle$ and $|y\rangle$ states. These are an equal admixture of the $|\pm 1\rangle$ states: $|+1\rangle + |-1\rangle$ and $|+1\rangle - |-1\rangle$.[53] These states have no z-axis magnetization and any transition between the three quadrupolar levels will result in no net change in the sample magnetization and therefore no signal is detected. A magnetic field resulting in a Zeeman splitting on the order of the asymmetry splitting will correct this problem, but typically those fields are much to large and perturb the spectrum

so that the quadrupolar information is difficult to extract. Thus, direct detection of integer spin quadrupolar splittings is limited to the case of $\eta$ close to zero. However, there is an indirect method that will be presented in Chapter 5.

### 3.3.4 Powder Samples

As usual the situation becomes more complex when powder or amorphous materials are used instead of single crystal samples. (This is not the case for zero field NQR however). In NMR experiments, the reason is that the dipolar interactions are randomly oriented with respect to the magnetic field. Thus, there is a range of splittings leading to the typical powder pattern.

In NQR, the quadrupolar principle axis system (PAS) is also randomly aligned with respect to the laboratory static magnetic field. To see what happens, we will look at the case where the quadrupolar interaction is much larger than the Zeeman splitting (which is true in all our NQR experiments). First, we truncate the Zeeman Hamiltonian (equation 3.6) to $H_z = -\gamma\hbar B_0 I_z \cos\theta$ where $\theta$ is the angle between the quadrupolar and Zeeman z-axes. The energy levels of the quadrupolar states are now shifted by $\Delta E(\pm m) = \mp\gamma\hbar B_0 m\cos\theta$. It is not as simple for the $\pm 1/2$ states which are also mixed by the $I_x$ and $I_y$ terms of equation 3.6 to give two new states,[1]

$$|+\rangle = +\sin\alpha\,|+1/2\rangle + \cos\alpha\,|-1/2\rangle \qquad 3.26a$$

$$|-\rangle = -\cos\alpha\,|+1/2\rangle + \sin\alpha\,|-1/2\rangle \qquad 3.26b$$

where $\tan\alpha = (\frac{f+1}{f-1})^{1/2}$ and $f = \{1 + (I+1/2)^2\tan^2\theta\}^{1/2}$. The resulting energy level shifts are $\Delta E = \mp\frac{f}{2}\gamma\hbar B_0\cos\theta$. Thus different crystallites in the sample will have different resonance frequencies depending on their orientation. The intensity of the transition is thus spread out over the range between $\pm m\gamma\hbar B_0$ rather than at two distinct transition

frequencies. Figure 3.11 displays the difference between single crystal and powder spectra for $^{27}Al$ in sapphire.

The range of splittings is not the only factor in the decreased intensity of powder signals. Because the energy levels are split by a smaller effective field, $B_{eff} = B_0 \cos\theta$ the cross relaxation rate is increased for quadrupolar nuclei not aligned with the magnetic field.

Also, as the pickup coil and rf coils are aligned in the laboratory frame (as is the magnetic field) they are less effective in detecting or irradiating quadrupolar nuclei not aligned with the magnetic field.[63, 64] The pickup coil is designed to measure changes in longitudinal magnetization as defined by the static magnetic field. For a nucleus with the quadrupolar z-axis not aligned with the magnetic field only the projection of its magnetization (and thus only the projection of its change in magnetization) on the laboratory z-axis affects the pickup coil. This indicates that nuclei perpendicular to the magnetic field contribute little intensity to the signal.

For much the same reason rf irradiation is less effective in promoting transitions for nuclei not correctly aligned. Thus complete saturation of the resonance is not necessarily accomplished by employing the same rf strength as used in the single crystal experiment.

Finally, the filling factor of the sample is much less for a powder than a single crystal occupying the same volume. There is much empty space between crystallites in a powder.

Despite all of the problems associated with the signal intensity of powder samples the main advantage is accessibility. Single crystals of many substances can simply not be obtained. We must therefore be satisfied with powders and seek to increase the signal to noise ratio to compensate for the loss in intensity. It should also be pointed out that for amorphous materials, such as glasses, there is no analog to a single crystal and they likewise suffer all of the problems described above, as well as often having a distribution in quadrupolar parameters causing an even larger spread in resonance frequencies and resulting in even less intense signals.

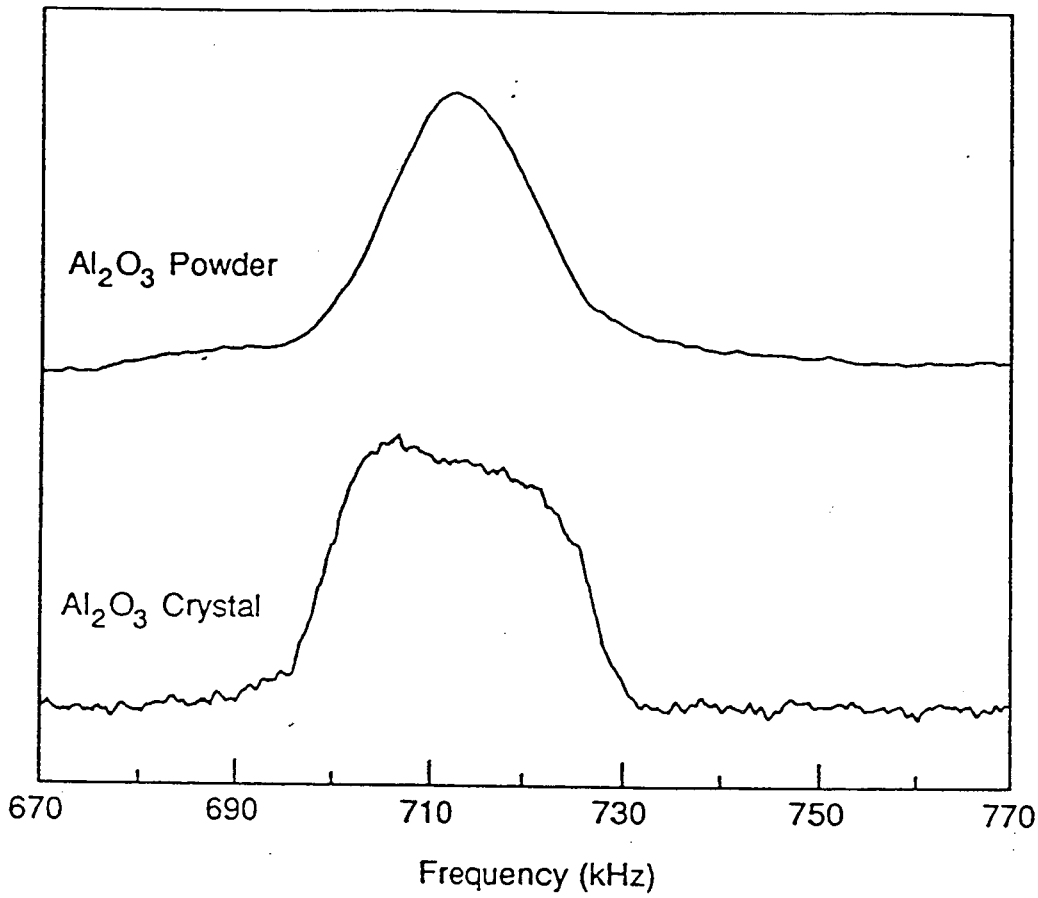


Figure 3.11. Comparison of powder and single crystal $^{27}Al$ NQR spectra of sapphire. The upper spectrum is an average of 8 scans and the lower is from 3 scans. The spectra are normalized to the same height, but the powder spectrum is actually has only about 15% of the intensity of the crystal spectrum.

## 3.4 Experimental Lineshapes and Intensities

Several experimental parameters affect the lineshapes of the observed resonances. Although we do not simulate any of these lineshapes to obtain additional information, it is worthwhile to understand the expected shape because that will affect the way the data is processed as well as the ideal sweep parameters.

The first effect considered is from spin lattice relaxation (see also section 3.2.1). If $T_1$ is much longer than the sweep time then the theoretical lineshapes described in sections 3.3.1-2 are good guides to the experimental shapes. However, if $T_1$ is on the order of the sweep time the experimental lineshape is significantly altered. Figure 3.12 shows simulated lineshapes for NMR experiments. NQR lineshapes are similar, with relaxation effects observed for both transitions. Often rf absorption and spin-lattice relaxation are occurring at comparable rates, so the measured transition frequency of a single spectrum can be shifted. In order to obtain the correct value it is imperative to combine spectra of sweeps in opposite directions (low to high frequency and high to low frequency). An experimental rule of thumb for this combination is to add the spectra if $T_1$ is less than the sweep time and subtract the spectra otherwise. Contemplation on the effect of relaxation on the lineshape proves this provides the largest signal intensity in all cases. Also, if at all possible, the sweep time should be made less than $T_1$. However, this can not always be done and still provide a saturating rf field.

If $T_1$ is on the order of or less than the time actually spent sweeping through the resonance, the signal intensity is often reduced. It is diminished because both rf absorption and relaxation are now directly competing at approximately the same rate and it becomes harder to saturate the transition. The only solution is to sweep faster and average many spectra. We have not found many samples that fit in this category other than organic

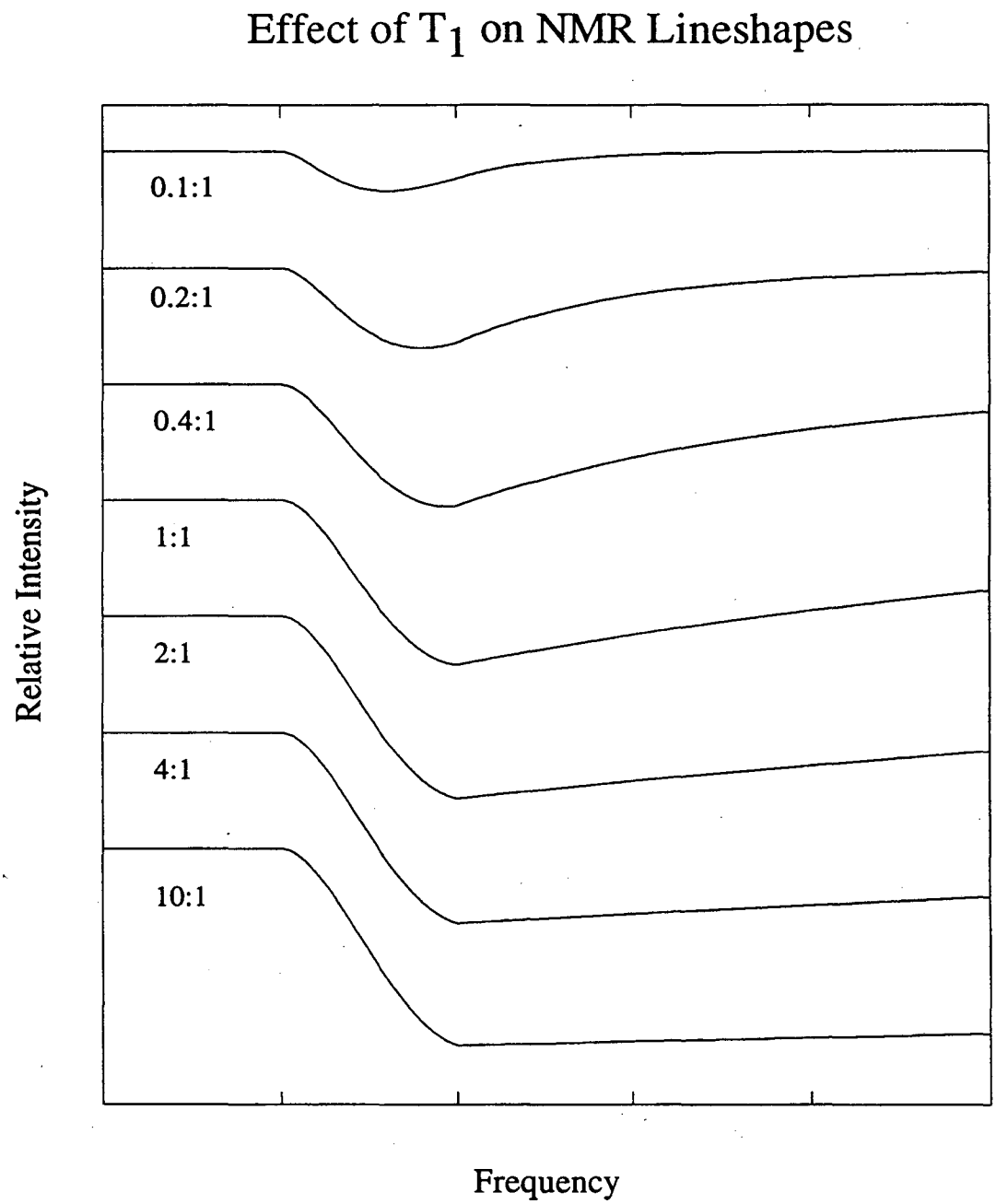


Figure 3.12. Simulated NMR spectra for different ratios of $T_1$ to sweep time. Note the change in lineshape and intensity as $T_1$ becomes shorter.

glasses, such as rapidly quenched toluene and bromoalkanes. At 4.2 K, short $T_1$'s are a rarity and the opposite, very long $T_1$'s, prove to be a more intractable problem.

The intensity of the signal is also obviously dependent on how many spins are excited. In the previous calculations, I have assumed saturation (i.e. the populations of the two states involved are equalized) however, this need not be the case. The number of spins that flip is experimentally controlled by the rf field strength and the sweep rate.[65] Figures 3.13 and 3.14 demonstrate both effects. As mentioned above, the optimal sweep rate is often limited by the relaxation rate. The rf field strength is restricted by the noise it generates in the pickup coil. Thus a saturating field can not always be obtained. The ideal sweep parameters are a balance between all of these effects.

For the $^{14}N$ experiments one more parameter enters into the picture. This is the cross relaxation time between the protons and the nitrogen (see Chapter 5 for the details of the experiment). Figure 3.15 shows spectra with varying sweep time. Comparing this with Figure 3.14, it becomes plain that the cross relaxation process is slower than rf absorption and therefore stronger rf fields or longer sweep times are needed for these experiments.

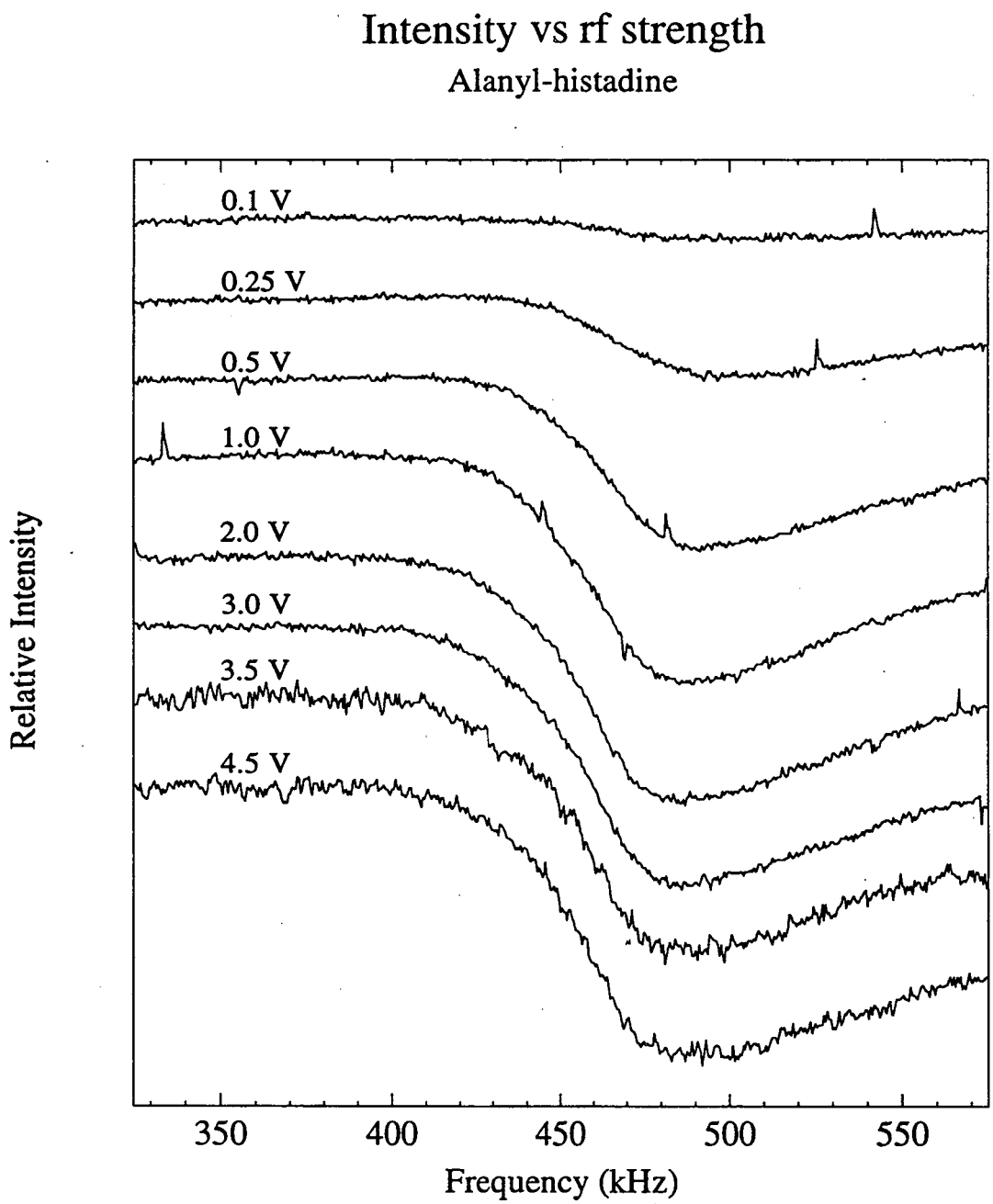


Figure 3.13. Experimental spectra of the $^{1}H$ resonance in L-alanyl-L-histadine for varying rf strengths with a constant sweep time of 100 seconds. The resonance appears to be saturated with 2.0 volts of rf.

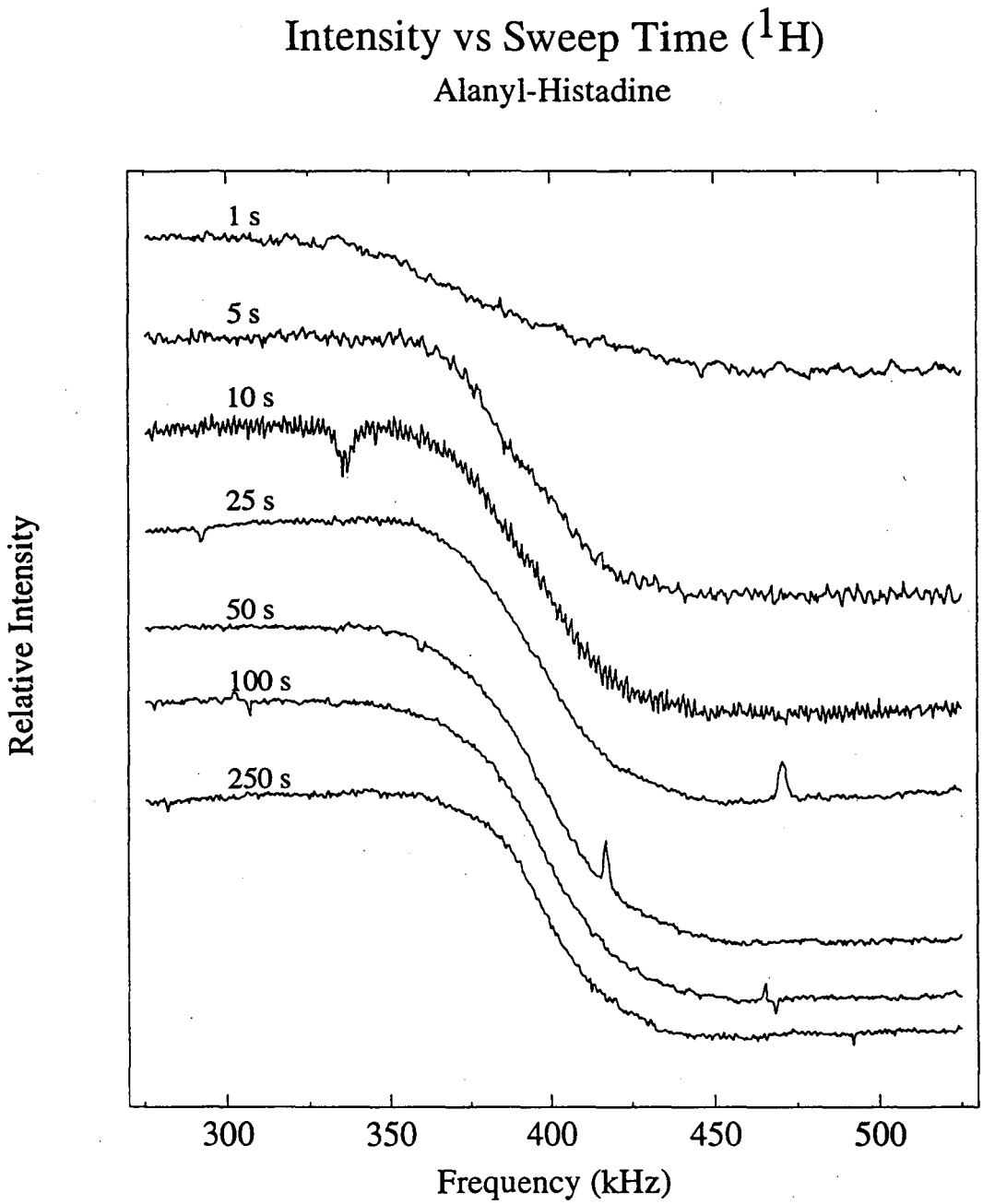


Figure 3.14. Experimental spectra of the $^1$H resonance in L-alanyl-L-histadine for varying sweep times with 3.0 volts of rf. The resonance appears to be saturated with a sweep time of 10 seconds.

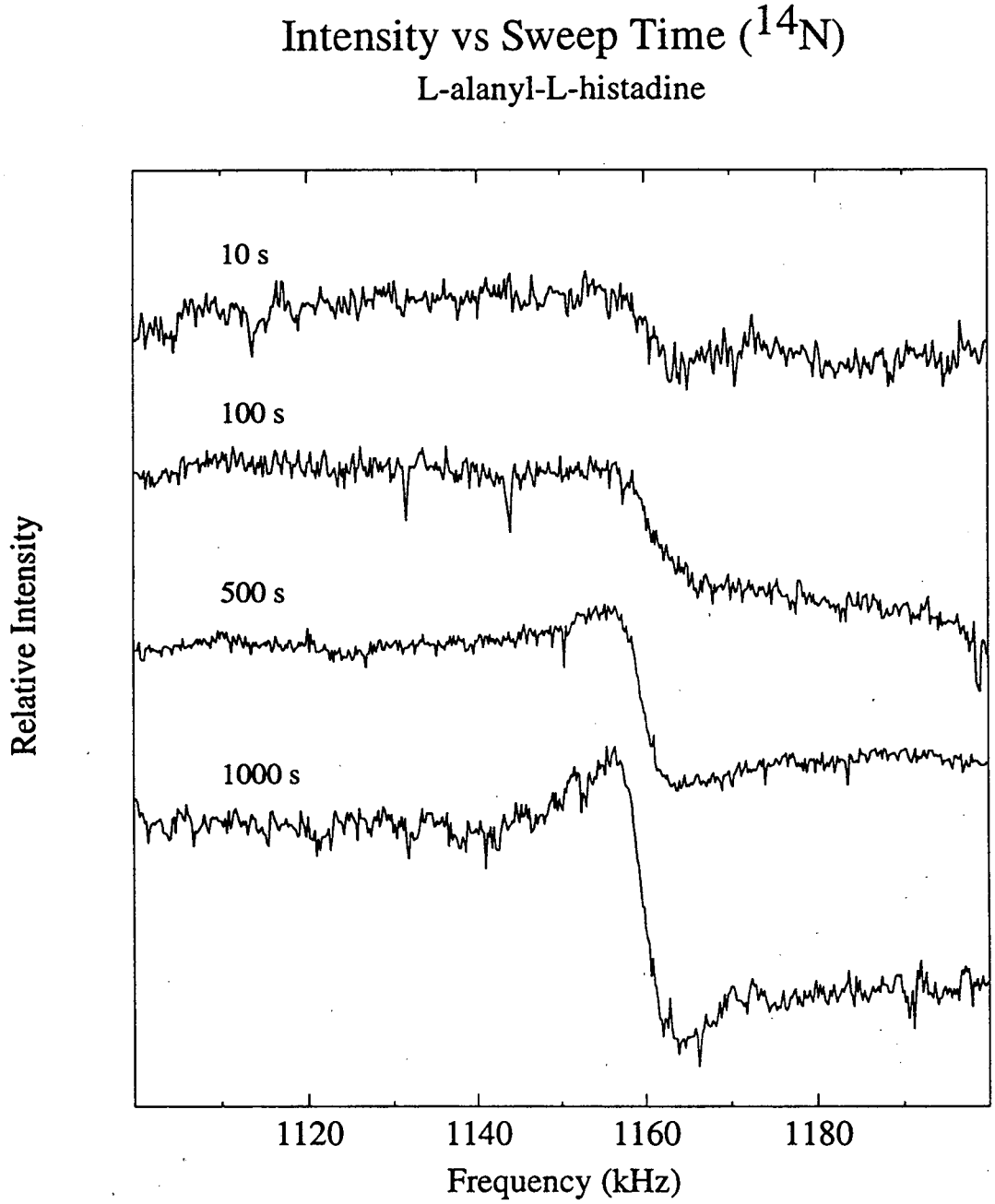


Figure 3.15. Experimental spectra of the $^{14}N$ resonance in L-alanyl-L-histadine for varying sweep times with 3.0 volts of rf. Compare these spectra to those for proton saturation (Figure 3.14).

# Chapter 4
# NQR of I=3/2, 5/2, and 7/2 Nuclei

## 4.1 Boron-11 (I = 3/2)

The SQUID spectrometer has proven its usefulness in studying $^{11}B$ quadrupole spectra for such powder samples as BN, $B_2O_3$ and its hydrated forms (such as boric acid, $H_3BO_3$), as well as $B_2O_3$ glass.[21, 22] The glass compounds are of particular interest in that there is a distribution of sites due to the amorphous nature of the sample that broadens the resonance. For binary glasses such as $xNa_2O{\cdot}B_2O_3$, studies can also be made detailing the change in crystal structure and borate species as the composition is varied. Bray and coworkers have accomplished much in this field.[66-70]

The one drawback of $^{11}B$ NQR is that there is only one resonance for each site. Because of this we can not uniquely determine the quadrupolar parameters by zero field NQR. However, when a small magnetic field is applied the powder lineshape is modified to reveal features from which the quadrupolar parameters can be calculated.[71]

I will present data from the SQUID spectrometer that suggest the important potential it has for the study of both binary borate glasses and the measurement of spin-3/2 quadrupolar parameters by means of NQR in a small magnetic field.

### 4.1.1 Sodium Borate Glass

Sodium borate glasses can be made by heating NaOH and $H_3BO_3$ to the melting point and then rapidly quenching the mixture. I made samples where x = 0, 0.11, 0.12, and 0.33. $^{11}B$ spectra of these samples are shown in Figure 4.1. Although these are poorly made samples, due to incomplete melting of the components, the spectra still show

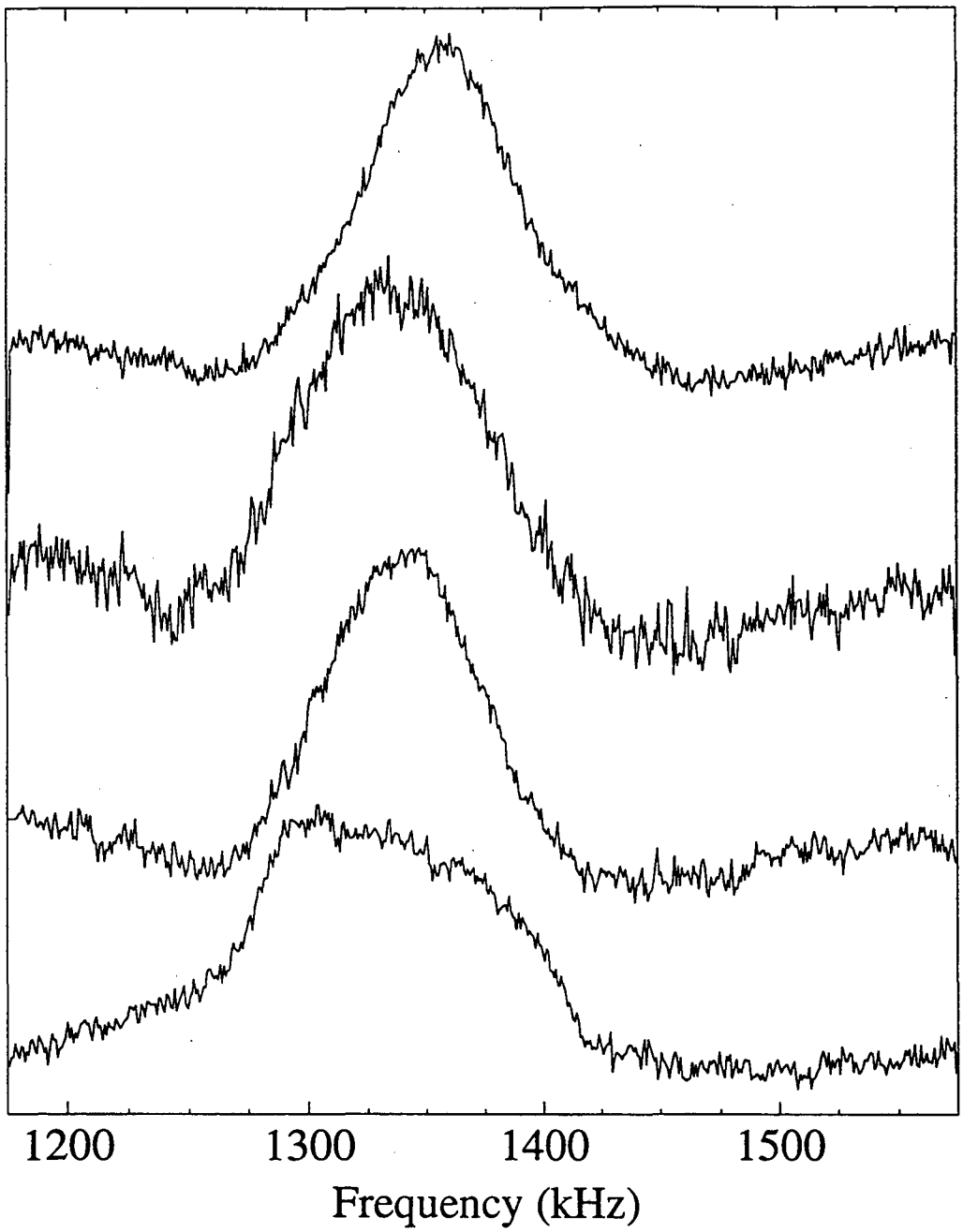


Figure 4.1 A series of quadrupolar spectra of vitreous $xNa_2O{\cdot}B_2O_3$ where x = 0, 0.11, 0.12, and 0.33 (top to bottom). A second peak grows at 1310 kHz, probably due to diborate and tetraborate structures, at the expense of the 1360 kHz boroxol peak as the sodium concentration increases.

an overall change as the sodium concentration increases. A second peak grows in around 1310 kHz at the expense of the 1360 kHz peak that is also found in $B_2O_3$ glass. Bray and coworkers have conducted similar experiments on a wider range of samples and find the same pattern.[66, 69, 70] $B_2O_3$ glass consists primarily of boroxol structures[66, 68] which would account for the 1360 kHz line. Bray suggests that the other resonance of $xNa_2O{\cdot}B_2O_3$ comes from either tetraborate or diborate structures.[70] Finding these two separate signals implies that different boron-oxygen structures can be resolved by NQR methods.

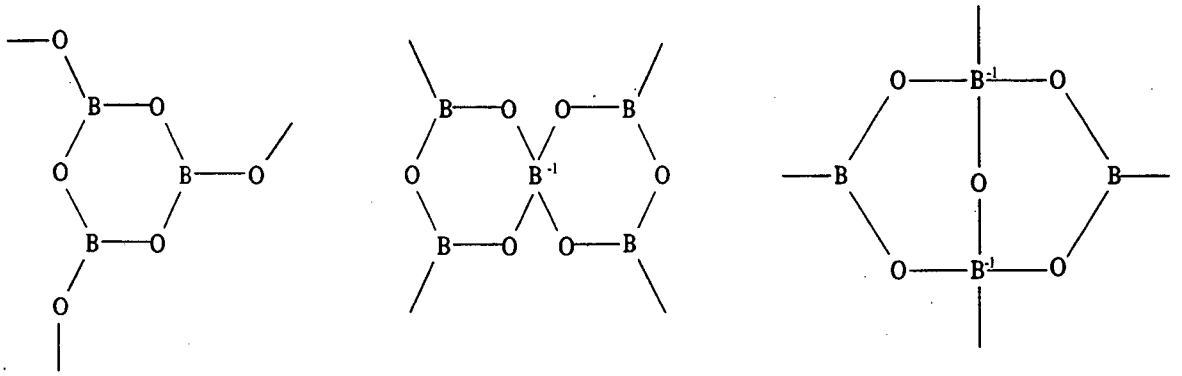

Boroxol Tetraborate Diborate

To continue this study we obtained quadrupolar spectra of the ternary glass system, $xNa_2O{\cdot}ySiO_2{\cdot}B_2O_3$. According to Bray, there should be many different types of borate structures,[67, 72-75] but we observed only one resonance in each case. This could very well be due to extensive overlapping among the lines so they could not be separately resolved. A potential solution to this problem is $^{10}B$ (I=3) NQR, which contains many more lines per site. These resonances would not necessarily overlap even when the $^{11}B$ transitions do.

### 4.1.2 Boron Nitride

One very real problem of spin-3/2 nuclei is the existence of only one quadrupolar transition. Thus the quadrupolar parameters can not be independently determined by zero field NQR. However, there is a solution based on calculations and experiments with chlorine NQR done by Morino and Toyama.[71] If a weak magnetic field is applied (weak meaning that the Zeeman interaction is much smaller than the quadrupole as in these experiments) then sharp features in the powder spectrum should be found at $\pm(1 \pm \eta)\frac{\gamma H_z}{2\pi}$. Figure 4.2 displays a spectrum of BN from the SQUID spectrometer in a field of approximately 60 gauss. Measurements from the spectra indicate features at 1330, 1378, 1566, and 1615 kHz with $\frac{\gamma H_z}{2\pi} = 150$ kHz. From this, $\eta \leq 0.13$ can be calculated. This value of $\eta$ near zero is substantiated by the crystal structure of BN at this temperature. The material is essentially an analog to graphite with hexagons made of alternating boron and nitrogen atoms.[76] This structure has a $C_3$ symmetry axis which would then indicate that $\eta$ should be zero.

The results of this analysis are encouraging for the future of spin-3/2 NQR. The SQUID spectrometer could be used to obtain an accurate frequency measurement at a lower field and then $\eta$ information from a higher field spectrum. Because a magnetic field must be supplied anyway, experiments of this type would require no extra effort, but yield the extra information needed to determine the quadrupolar parameters.

## 4.2 Sodium-23 (I = 3/2)

Sodium is an important element in many ionic compounds. Most of these materials, however, have symmetry that preclude the quadrupole interaction, such as the

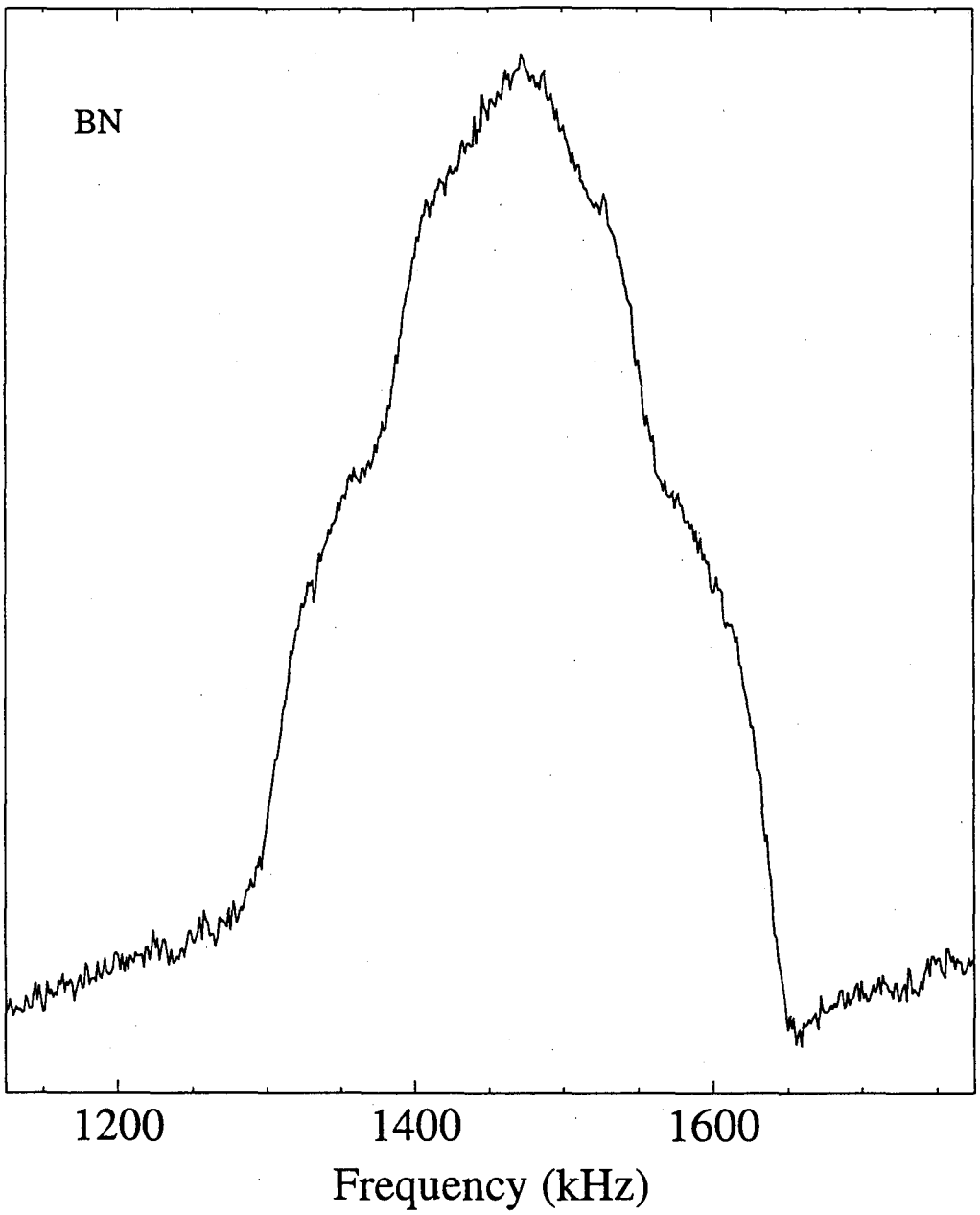


Figure 4.2 The $^{11}B$ NQR spectrum of BN in a field of 60 Gauss.

cubic lattice of NaCl. $NaBrO_4$ is not among that group and has been extensively studied by NMR lineshape analysis of single crystal samples.[77-79] I measured the NQR resonance of $^{23}Na$ for a powder sample of $NaBrO_4$ and found it to be 444 ± 12 kHz which agrees with the literature value of 443 kHz at 4 K.[77] The spectrum is displayed in Figure 4.3. Because $^{23}Na$ is a spin-3/2 nucleus only one transition frequency can be measured. However, from single crystal NMR studies it is found that $\eta = 0$. Thus, our transition frequency would lead to a quadrupolar coupling constant of 888 ± 24 kHz.

## 4.3 Aluminum-27 (I = 5/2)

### 4.3.1 Sapphire ($\alpha$-$Al_2O_3$) Crystal

Sapphire has become the primary test material for the SQUID spectrometer. We have both a single crystal and powder samples of sapphire. Spectra of both samples are shown in Figure 3.11. Sapphire consists of aluminum sitting in a distorted octahedron formed by six oxygen atoms. It can be thought of as an aluminum atom sitting asymmetrically between two equilateral triangles with an oxygen atom at each apex.[80] This model would indicate that $\eta = 0$ due to the $C_3$ symmetry axis. From the resonance frequencies of 357 ± 2 kHz and 714 ± 2 kHz, the quadrupolar parameters are calculated to be $C_Q = 2.38 \pm 0.01$ MHz and $\eta = 0.00 \pm 0.06$, which supports this model.[20] However, these findings have recently been disputed by Bray and coworkers. They use an NQR spectrometer with a Robinson oscillator for detection and obtain resonance frequencies of 361.6 ± 0.4 kHz and 715.5 ± 0.7 kHz with corresponding quadrupolar parameters of $C_Q = 2.389 \pm 0.002$ MHz and $\eta = 0.091 \pm 0.007$.[66]

They also proceeded to calculate quadrupolar parameters from SQUID data in Figure 3 of reference 20 which they claim gives $\eta = 0.12 \pm 0.03$. However, it must be noted that the figure displayed a spectrum obtained in only one sweep direction and so

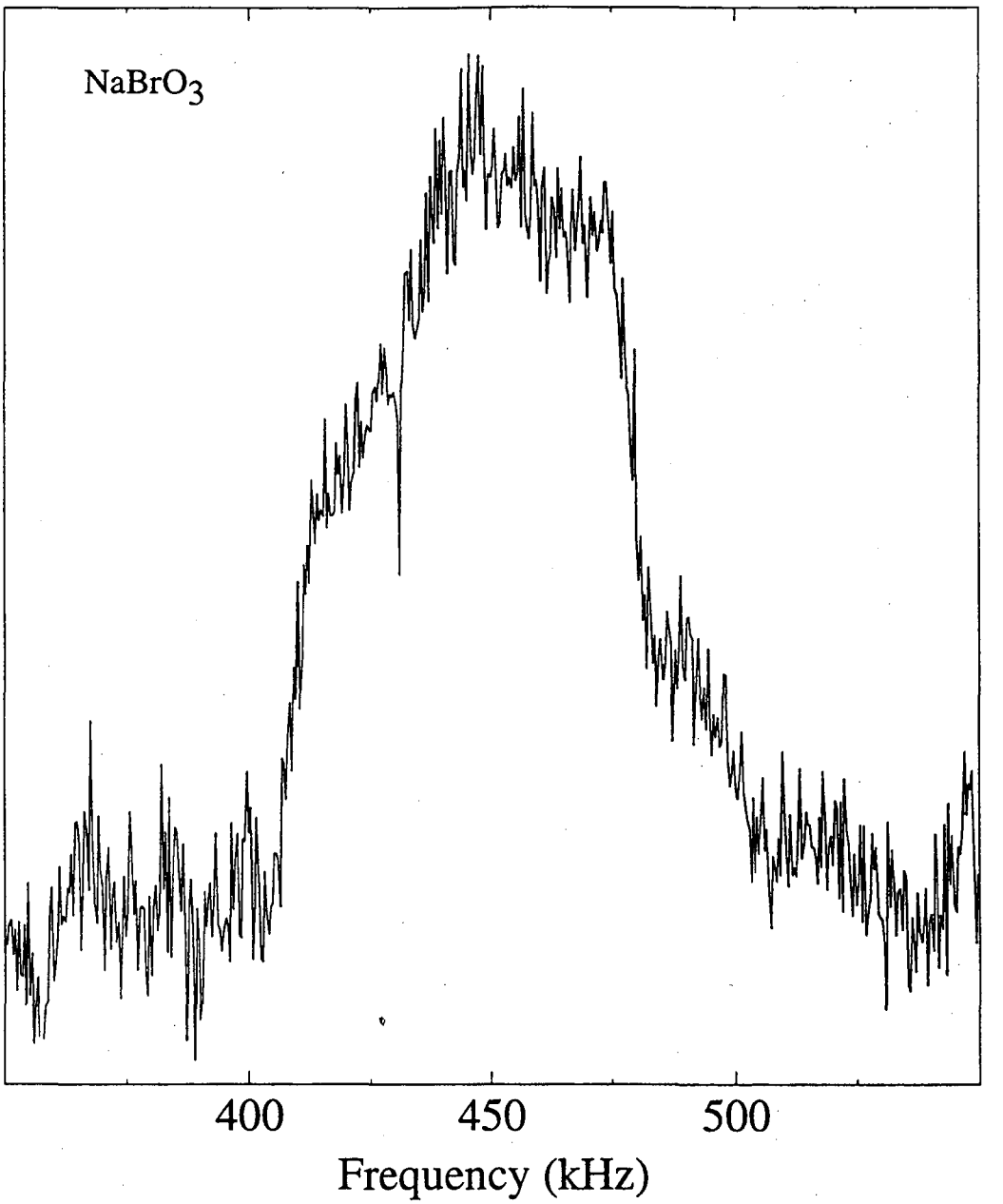


Figure 4.3 $^{23}Na$ NQR spectrum of $NaBrO_4$ in a field of approximately 15 Gauss. A resonance is found at 444 ± 12 kHz.

therefore should not be relied upon to give accurate frequency information due to distortions caused by relaxation and saturation effects.

They suggest that the deviation between our SQUID results and their values is due to our use of a magnetic field. Of course, in this experiment a magnetic field is necessary to separate the degenerate quadrupolar states and minimize cross relaxation. To test their hypothesis, I measured the quadrupolar resonances at different field strengths. Figure 4.4 displays the results. There was no change in the frequency of either resonance despite a change in the field by a factor of 2.5.

A more recent paper by Bray lists new values of the quadrupolar parameters, $C_Q$= 2.386 ± 0.002 MHz and $\eta$ = 0.034 ± 0.016.[81] Note that the two values of eta from Bray are not within the experimental error of each other. Perhaps the error can be found in the fact that their spectra are obtained in only one sweep direction and so may be biased by relaxation and saturation effects. Alternately, their relatively fast sweep rates/time constant could cause a distortion in the line. Bray's experiments give ratios of 8.1 kHz/time constant and 3.4 kHz/time constant for the low and high frequency regions respectively.[66] Our experiments typically have a range between 0.2 - 0.5 kHz/time constant. This ratio expresses approximately the frequency range of signal that is averaged for each point in the spectrum. Because the differences in the two sets of resonance frequencies are about half the ratio of Bray's experimental sweep rates/time constant, $\Delta\nu_l$ = 4.6 kHz and $\Delta\nu_h$ = 1.5 kHz, it seems possible that this may have affected the measurement of the resonances. The correct answer is still unknown, but we are preparing experiments that will measure these transitions using a pulsed SQUID spectrometer. Because those experiments require no magnetic field, they may be able to provide a resolution to this debate.

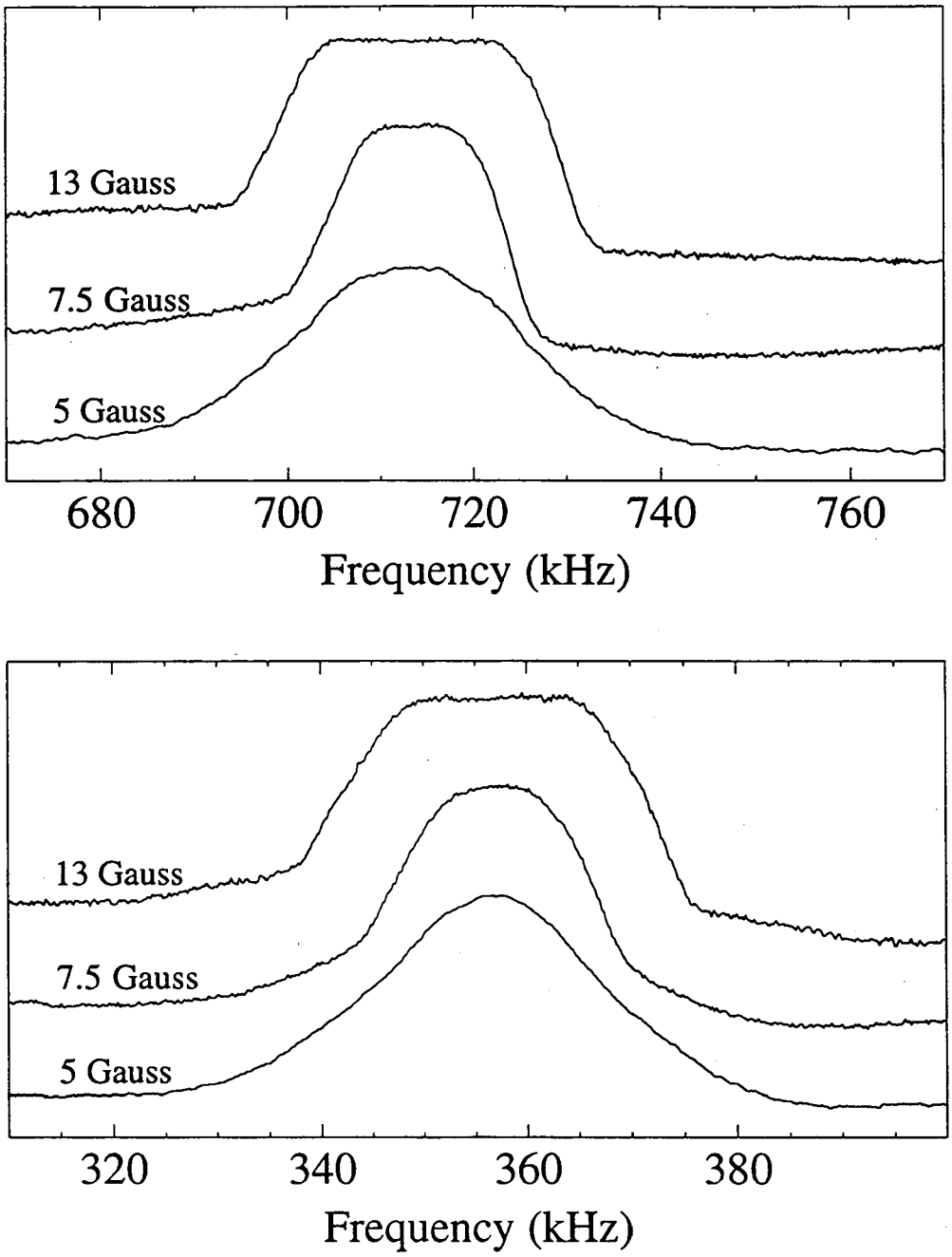


Figure 4.4 A series of quadrupolar spectra taken at fields of approximately 5, 7.5, and 13 Gauss. Note that in all three spectra the resonances remain at 357 ± 2 kHz and 714 ± 2 kHz. Thus these frequencies are not a function of the magnetic field strength.

## 4.3.2 Petalite

Petalite is a naturally occurring polycrystalline lithium aluminosilicate. It has only one distinct aluminum site, which is a distorted $AlO_4$ tetrahedron with Al-O bond distances of 1.742 and 1.732 Å.[82] Figure 4.5 shows the $^{27}Al$ quadrupolar spectra of petalite with two resonances at 834 ± 5 kHz and 1314 ± 5 kHz. The quadrupolar parameters are calculated to be $C_Q = 4.56 \pm 0.01$ MHz and $\eta = 0.47 \pm 0.1$. These values agree with those later found by dynamic angle spinning (DAS) experiments: $C_Q = 4.62 \pm 0.05$ MHz and $\eta = 0.48 \pm 0.03$.[83]

The linewidths of these spectra are relatively large (100 - 200 kHz) as compared to the sapphire powder (20 kHz) and are most likely due to the polycrystalline nature of the sample. Structural disorder can lead to broadened lines as found in this sample and in glasses. This is due to a distribution of electric field gradient values resulting from variation in the structural parameters.

## 4.4 Vanadium-51 (I = 7/2)

Vanadium-51 provides the first example of a transition metal compound and a nucleus with I = 7/2. As mentioned in Chapter 3, low frequency quadrupolar resonances can be found for transition metals only in nonparamagnetic states or in compounds which deviate only slightly from symmetry that would eliminate the quadrupolar interaction. In this case, I obtained a compound, ammonium metavanadate ($NH_4VO_3$), with a V(V) configuration. V(V) is not paramagnetic and many examples of such compounds have been studied previously by lineshape analysis and Bray's Robinson oscillator spectrometer.[70, 84, 85] $NH_4VO_3$ has been observed by both of these methods. Figure 4.6 displays the $^{51}V$ resonances obtained by the SQUID spectrometer. The transitions at 388 ±

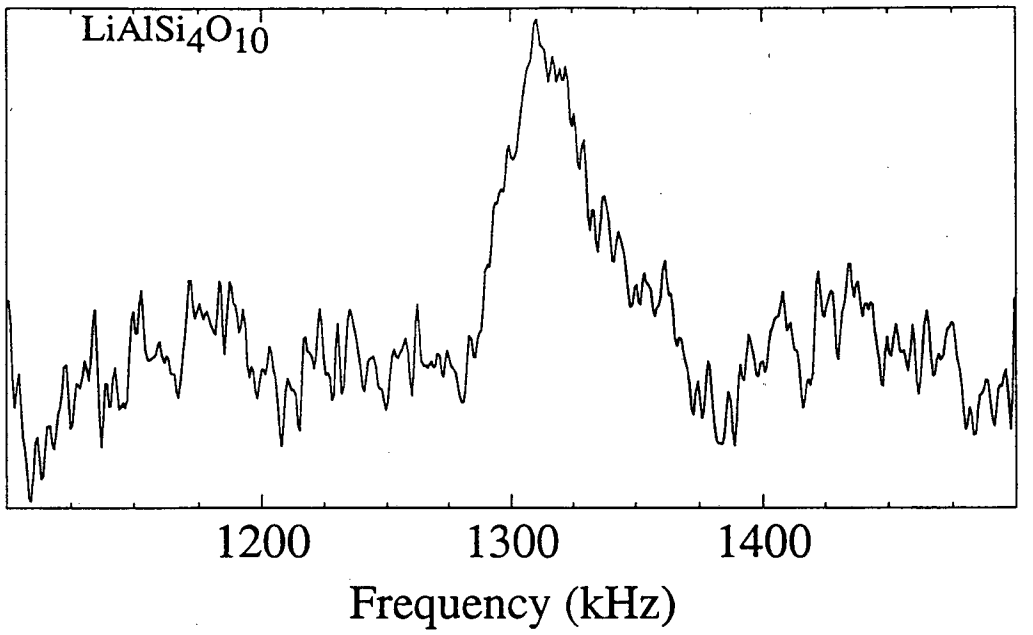


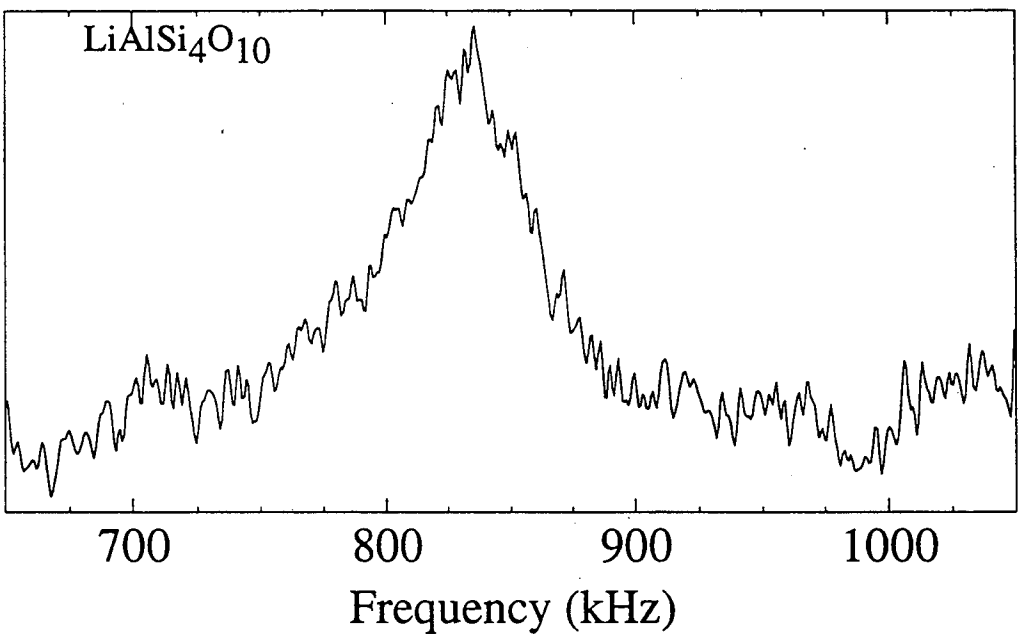


Figure 4.5 $^{27}$Al NQR spectra of petalite in a field of approximately 10 Gauss. Resonances are found at 834 ± 5 kHz and 1314 ± 5 kHz. The quadrupolar parameters are calculated to be $C_Q$ = 4.56 ± 0.01 MHz and $\eta$ = 0.47 ± 0.1.

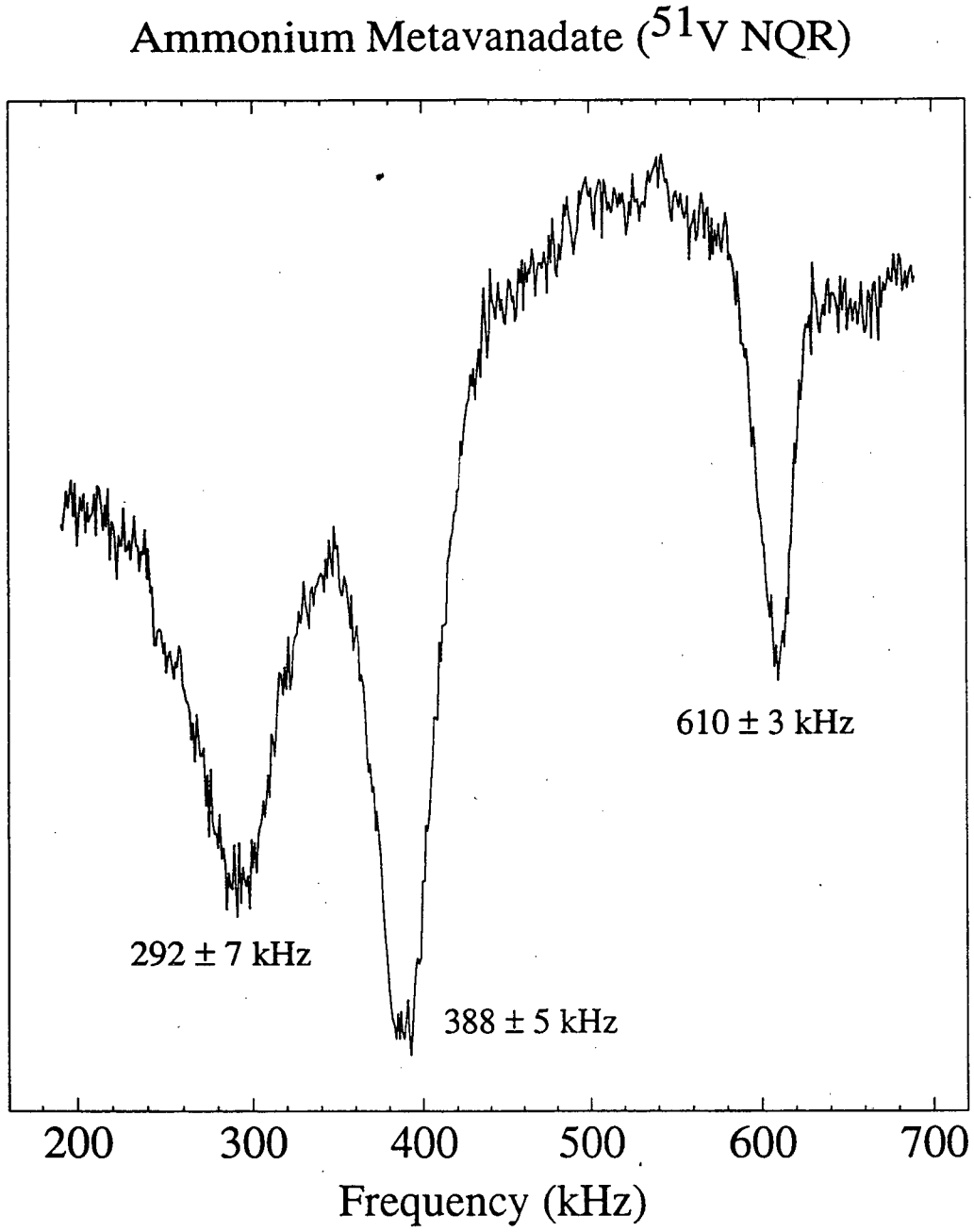


Figure 4.6 $^{51}$V NQR spectra of $NH_4VO_3$ in a field of approximately 7.5 Gauss. Resonances are found at 292 ± 7 kHz, 388 ± 5 kHz, and 610 ± 3 kHz. The quadrupolar parameters are calculated to be $C_Q = 2.88 \pm 0.04$ MHz and $\eta = 0.38 \pm 0.03$.

5 kHz and 610 ± 3 kHz agree well with those found by Bray (388.4 ± 0.5 kHz and 606.3 ± 0.3 kHz).[85] They were not able to detect the lowest frequency transition which we find at 292 ± 7 kHz.

For spin-7/2 nuclei there is no analytical solution for the quadrupolar parameters, $C_Q$ and $\eta$. The secular equation (with $E = hC_Q/28$),

$$E^4 - 42(1 + \frac{\eta^2}{3})E^2 - 64(1 - \eta^2)E + 105(1 + \frac{\eta^2}{3})^2 = 0, \qquad 4.1$$

must be solved numerically (see Figure 3.4). Doing this gives values of $C_Q = 2.88 \pm 0.04$ MHz and $\eta = 0.38 \pm 0.03$. These agree with Bray's results of $C_Q = 2.868 \pm 0.005$ MHz and $\eta = 0.363 \pm 0.013$.[85] (He correctly assumes that the resonances he measured were the two higher frequency transitions.)

Attempts were made to study other vanadium compounds, most notably vanadium oxide as a catalyst on a silica surface. However, no resonances were found. This may be due to one or more of the following causes. First, there may not have been enough vanadium in the sample for detection or it may have been in the wrong oxidation state. Also, $V_2O_5$ has a very small quadrupolar coupling constant and so the transitions may have been to low in frequency for detection. Or $T_1$ may have been to long. Further investigations into these catalysts could, however, be profitable given their importance in chemistry.

## 4.5 Manganese-55 (I = 5/2)

Another transition metal nucleus which I have studied is $^{55}Mn$. The only nonparamagnetic oxidation state of this element is Mn(VII) which forms the basis for the permanganates, $XMnO_4$. One problem with these samples is their light sensitivity. So care was taken to recrystallize the materials and then avoid as much exposure to light as possible.

## 4.5.1 Potassium Permanganate

The first sample is $KMnO_4$, the most common of the permanganate family. Resonances were measured on two separate occasions with transitions detected at 374 ± 7 kHz and 730 ± 7 kHz as shown in Figure 4.7. From this data, the quadrupolar parameters are calculated to be $C_Q = 2.44 \pm 0.02$ MHz and $\eta = 0.1 \pm 0.1$. Previous measurements from an NMR lineshape analysis of a room temperature sample found $C_Q = 1.70 \pm 0.07$ MHz and $\eta < 0.05$.[86] The difference between the quadrupolar parameters in these two experiments may come from several sources. First, a structure change between room temperature and 4.2 K could easily account for the difference. Or, perhaps the samples were not prepared under similar conditions so that again crystal structures are not equivalent. With this in mind I conducted two sets of experiments with different samples, both times after recrystallization of $KMnO_4$. I obtained the same resonance values each time.

The one area of agreement for both sets of data is the value of $\eta$. From room temperature crystal structure data it is found that the $MnO_4^-$ group is a nearly regular tetrahedron with Mn-O distances of 1.622, 1.625, 1.634, and 1.635 Å.[87] Thus the electric field gradient arises primarily from the electric charges of the ions in the orthorhombic crystal structure. This leads to the high degree of symmetry evidenced by $\eta \approx 0$.

## 4.5.2 Silver Permanganate

In the second sample, $AgMnO_4$, this symmetry is lacking. Experimental resonances were found at 2309 ± 15 kHz and 1451 ± 10 kHz and are shown in Figure 4.8. The calculated quadrupolar parameters are $C_Q = 7.99 \pm 0.06$ MHz and $\eta = 0.462 \pm 0.016$. At least part of the difference between the two permanganates can be attributed to the much

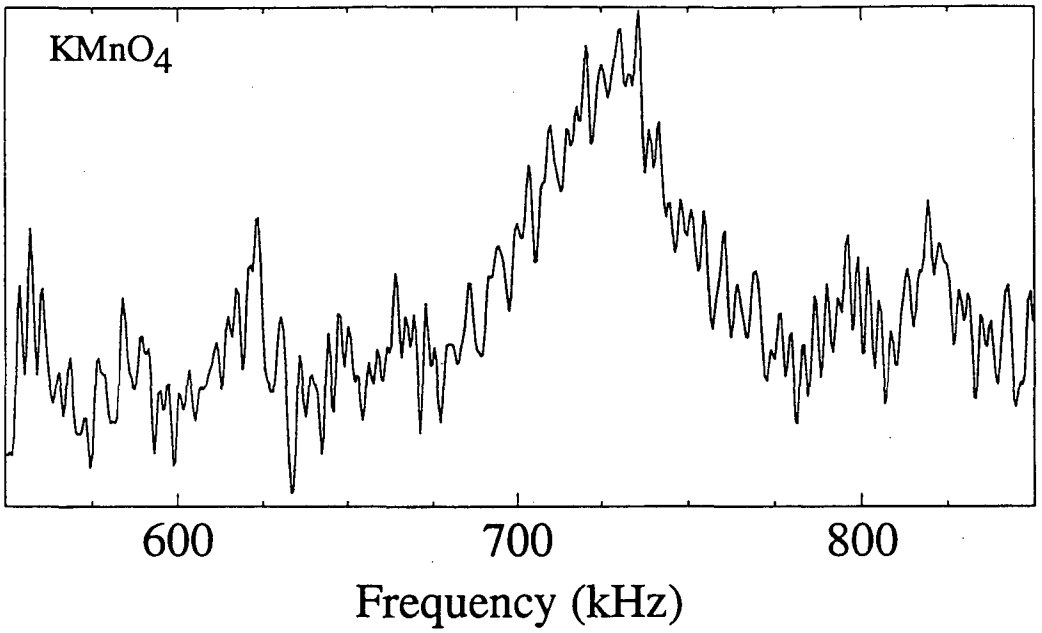


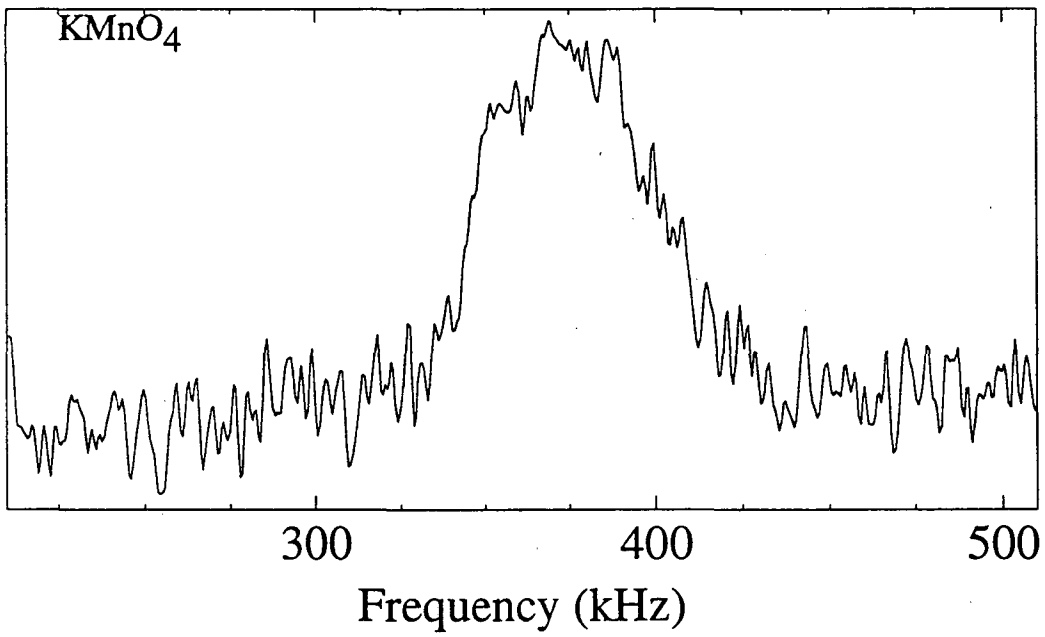


Figure 4.7 $^{55}Mn$ NQR spectra of $KMnO_4$ in a field of approximately 13 Gauss. Resonances are found at 374 ± 7 kHz and 730 ± 7 kHz. The quadrupolar parameters are calculated to be $C_Q = 2.44 \pm 0.02$ MHz and $\eta = 0.1 \pm 0.1$.

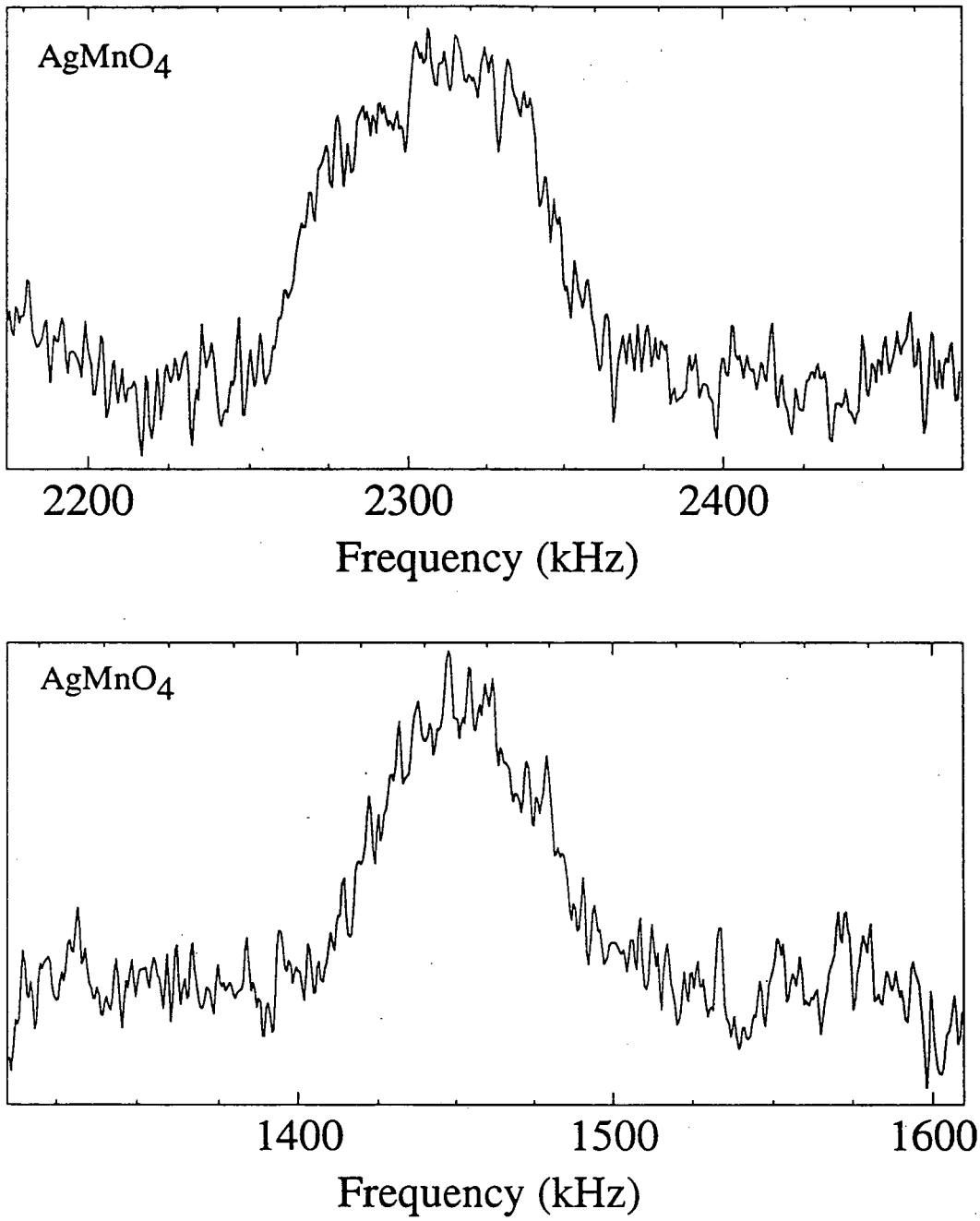


Figure 4.8 $^{55}$Mn NQR spectra of $AgMnO_4$ in a field of approximately 13 Gauss. Resonances are found at 2309 ± 15 kHz and 1451 ± 10 kHz. The quadrupolar parameters are calculated to be $C_Q = 7.99 \pm 0.06$ MHz and $\eta = 0.462 \pm 0.016$.

larger deviation from a perfect tetrahedron of the $MnO_4^-$ unit in $AgMnO_4$. Here the Mn-O distances are found to be 1.612, 1.631, 1.625, and 1.571 Å[88] which show larger differences among the bond lengths than those found for $KMnO_4$. This can easily change the value of $\eta$ from its symmetric value of zero. It would also increase the strength of the electric field gradient, and therefore $C_Q$, because it deviates more from the symmetric tetrahedron which would have no electric field gradient. Also, because it is more covalently bonded, the molecular volume of $AgMnO_4$ is 15% smaller than $KMnO_4$. This could also increase the electric field gradient due to the closer proximity of the valance electrons.

Further studies of permanganates as a function of the cation could be very interesting. Perhaps a comparison of quadrupolar parameters with the ionicity of the cation-$MnO_4^-$ bond should be investigated. Also, information about the effect of crystal structure changes and deviations in basic units such as $MnO_4^-$ could be gained.

# Chapter 5
# NQR of Nitrogen-14 (I=1)

As mentioned in Chapter 2, the case of integer spin nuclei is special. Only under unusual circumstances can these resonances be directly detected. I will begin this chapter with a detailed explanation of the problem in detection of integer spin NQR. Then I will present some data on solid $\alpha$-$N_2$ which has been directly detected and illustrates the special case where $\eta$ is close to 0. Following that I will introduce the indirect method of detection which involves level matching between a proton NMR transition and a nitrogen NQR resonance. Finally, I will describe some samples that we have studied, among which are amino acids and small peptides, to demonstrate the method and show what information we can learn.

## 5.1 The Integer Spin Problem

Integer spin systems present a problem because all nondegenerate states of the system have a vanishing magnetic moment in zero magnetic field.[57] I will focus on the I = 1 case because that includes the most important nuclei: $^2$D and $^{14}$N. The same ideas will also apply to other integer spin systems, such as I = 3 ($^{10}$B) and I = 5 ($^{50}$V).

The vanishing magnetic moment can be derived in two distinct but equivalent ways. First, the brute force method requires the calculation of eigenvalues and eigenstates from the quadrupolar Hamiltonian;

$$H_Q = \frac{e^2qQ}{4I(2I-1)}[3I_z^2 - I^2 + \frac{\eta}{2}(I_+^2 + I_-^2)]. \qquad 5.1$$

For I=1 this leaves eigenstates;

$$|x\rangle = |+1\rangle + |-1\rangle, \qquad 5.2a$$

$$|y\rangle = |+1\rangle - |-1\rangle, \qquad 5.2b$$

$$|z\rangle = |0\rangle, \qquad 5.2c$$

with eigenvalues;

$$\frac{hC_Q}{4}(1 + \eta), \qquad 5.3a$$

$$\frac{hC_Q}{4}(1 - \eta), \qquad 5.3b$$

$$-\frac{hC_Q}{2}, \qquad 5.3c$$

respectively, where $C_Q = \frac{e^2qQ}{h}$. This leads to three possible transitions;

$$\nu_+ = \frac{C_Q}{4}(3 + \eta), \qquad 5.4a$$

$$\nu_- = \frac{C_Q}{4}(3 - \eta), \qquad 5.4b$$

$$\nu_0 = \frac{C_Q}{2}\eta. \qquad 5.4c$$

The corresponding energy level diagram for this situation is found in Figure 5.1. Note that all three eigenstates have no magnetic moment (i.e. $\langle\Psi^*|I_z|\Psi\rangle = 0$).

Another way to show that the magnetic moment must vanish is through the use of group theory and time reversal symmetry. An electric field is in not affected by time reversal, but a magnetic field would be reversed as it is created by charges traveling in a specific direction. Therefore, a set of energy levels that results from an electric field, such as the nuclear quadrupole levels, will not be changed by the reversal of time.

The Schrödinger equation,

$$H\Psi = -i\hbar\frac{\partial\Psi}{\partial t} \qquad 5.5$$

is invariant under time reversal if 1) H is time reversal invariant and 2) we reverse time ($t \rightarrow -t$) and take the complex conjugate ($i \rightarrow -i$ and $\Psi \rightarrow \Psi^*$). Because a nondegenerate

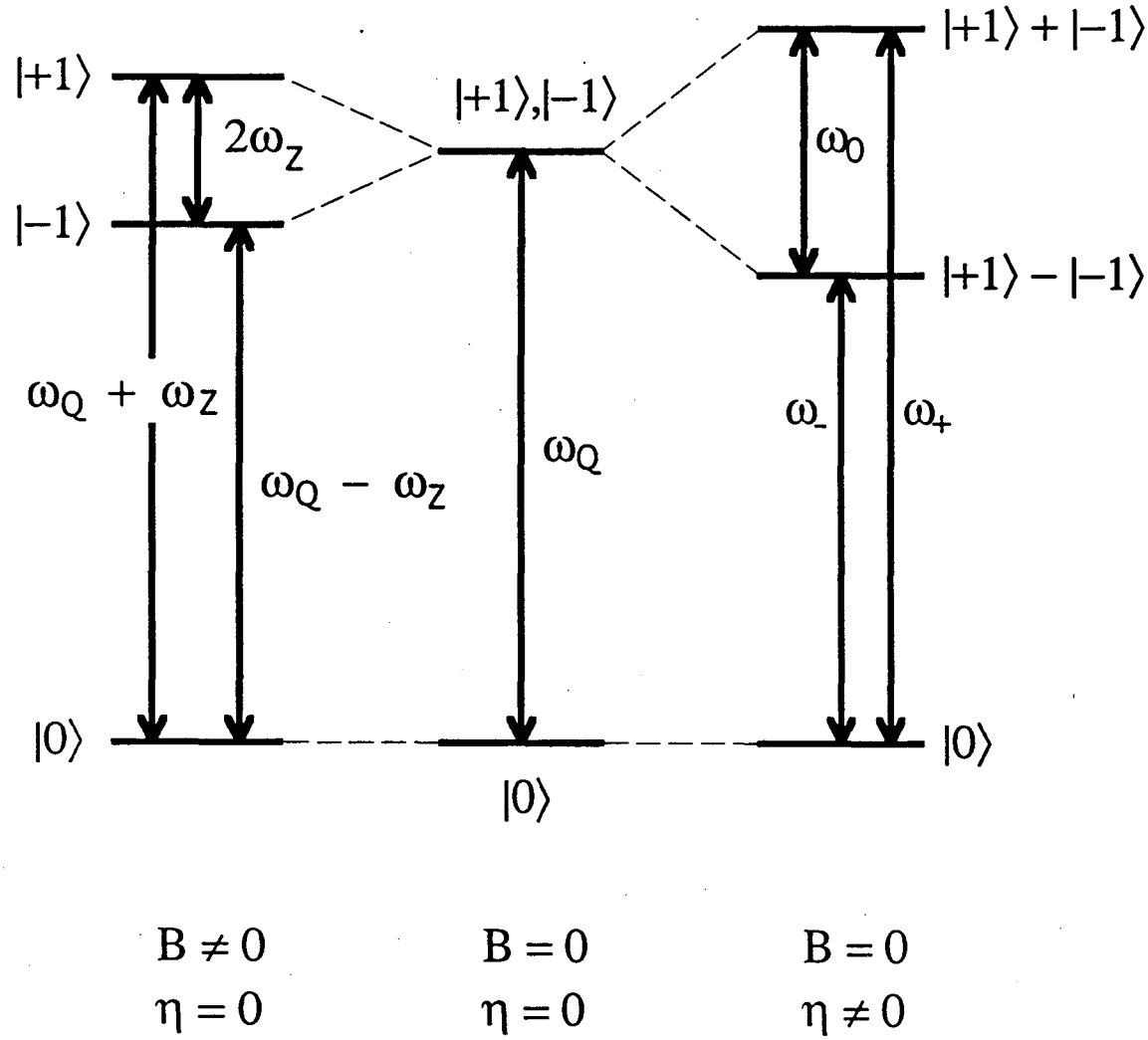


Figure 5.1. Energy level diagram for a spin-1 nucleus. Note that for the case where $\eta \neq 0$ all states have zero longitudinal magnetization.

state produced by an electric field can in no way be altered by time reversal but must be changed to its complex conjugate due to the Schrödinger equation condition;

$$\Psi = \Psi^*. \qquad 5.6$$

Therefore $\Psi$ is real. However, an angular momentum operator, for example

$$\langle L_z \rangle = -i\hbar(x\frac{\partial}{\partial y} - y\frac{\partial}{\partial x}), \qquad 5.7$$

is imaginary and can not be time reversal invariant unless its eigenvalue, $L_z$, is zero. Thus the expectation value of an angular momentum operator (and therefore a magnetic moment) of a nondegenerate state in a quadrupole system must be zero in the absence of a magnetic field.

Both of these arguments demonstrate that the nondegenerate states of an integer spin nucleus have no magnetic moment. There is no net change in magnetization with rf irradiation at a resonance frequency despite a change in the spin populations of the various levels. Because the SQUID measures such changes in magnetization, we see that there is no signal to detect.

## 5.2 Direct Detection

We could, however, apply a magnetic field to break the time reversal symmetry and thereby obtain a magnetic moment. To calculate this magnetic moment we will assume the most favorable of conditions, a single crystal sample with the magnetic field aligned along the quadrupolar z axis. The Hamiltonian is then

$$H_Q + H_z = \frac{e^2qQ}{4I(2I-1)}[3I_z^2 - I^2 + \frac{\eta}{2}(I_+^2 + I_-^2)] - \gamma\hbar I_z B_0. \qquad 5.8$$

Solving this Hamiltonian leads to eigenvalues,[89-91]

$$E_x = \frac{e^2qQ}{4}[1 + \eta(1 + f^2)^{1/2}], \qquad 5.9a$$

$$E_y = \frac{e^2qQ}{4}[1 - \eta(1 + f^2)^{1/2}], \qquad 5.9b$$

$$E_z = -\frac{e^2qQ}{2}, \qquad 5.9c$$

with eigenstates

$$|x\rangle = \cos\theta|+1\rangle + \sin\theta|-1\rangle, \qquad 5.10a$$

$$|y\rangle = \sin\theta|+1\rangle - \cos\theta|-1\rangle, \qquad 5.10b$$

$$|z\rangle = |0\rangle, \qquad 5.10c$$

where

$$\cos\theta = \frac{1}{\sqrt{2}}[1 + f^2 + f(1 + f^2)^{1/2}]^{-1/2}, \qquad 5.11a$$

$$\sin\theta = \frac{1}{\sqrt{2}}[1 + f^2 - f(1 + f^2)^{1/2}]^{-1/2}, \qquad 5.11b$$

$$f = \frac{\gamma B_0}{\frac{e^2qQ\eta}{4h}}. \qquad 5.11c$$

We see that the magnetic moment is no longer zero, but a function of the parameter, f. If we calculate the expectation values of the wavefunctions we find that

$$\langle I_x\rangle = \langle I_y\rangle = 0, \qquad 5.12a$$

$$\langle z|I_z|z\rangle = 0, \qquad 5.12b$$

and

$$\langle x|I_z|x\rangle = -\langle y|I_z|y\rangle = -\frac{f}{(1 + f^2)^{1/2}} = -F(f). \qquad 5.13$$

This factor, F(f), is the magnetic moment of the $|x\rangle$ and $|y\rangle$ states. This is what the SQUID will measure when a nucleus is excited from, for example, the $|z\rangle$ to the $|x\rangle$ state. Figure 5.2 shows a plot of F(f) for typical values of our NQR experiments.

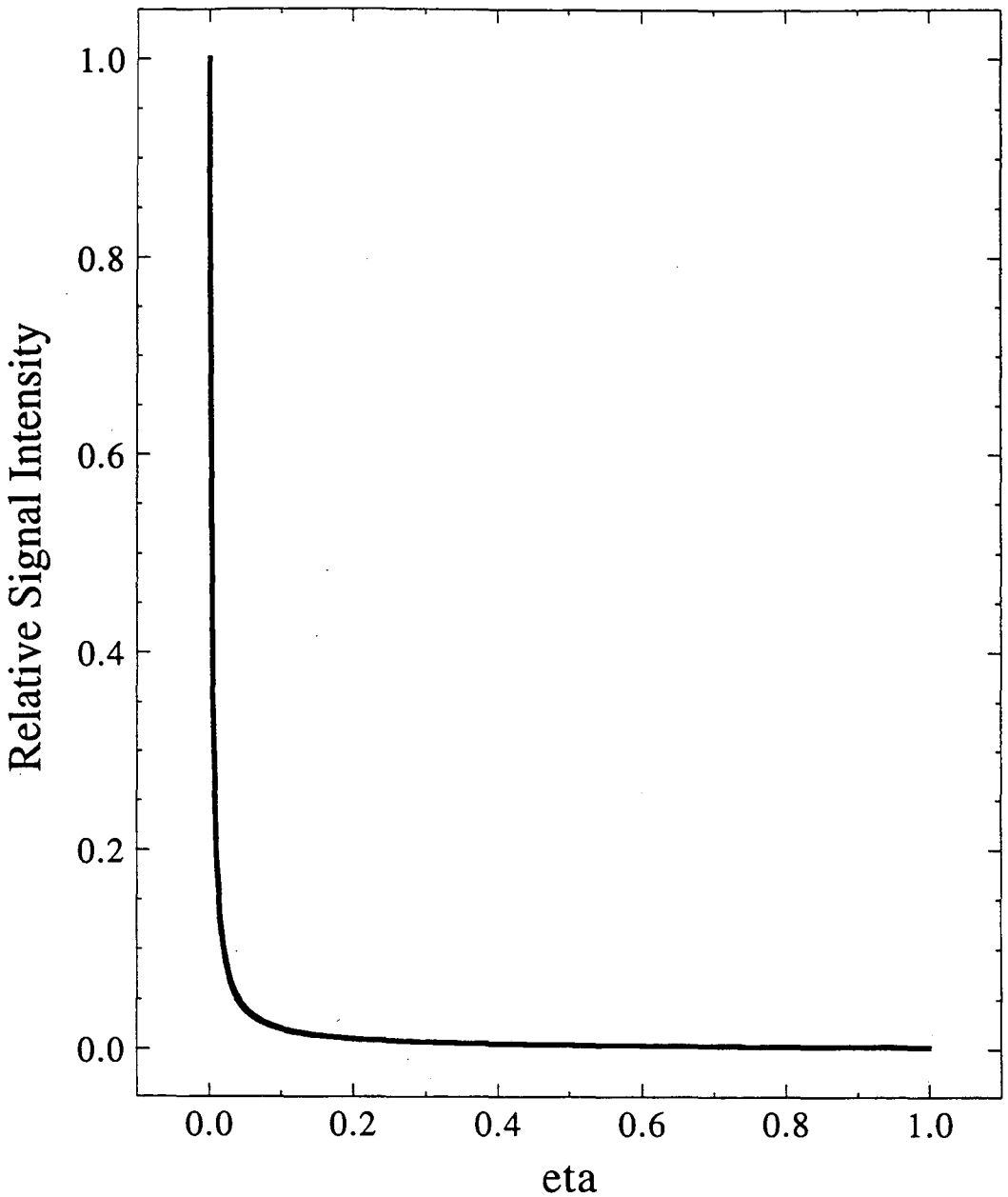


Figure 5.2. Signal intensity vs. $\eta$ with $\gamma B_0 = 11$ kHz and $\frac{e^2qQ}{h} = 5000$ kHz.

From this diagram it is easily seen the magnetic moment is nearly zero unless $\eta \approx 0$. One could increase the field, but for powder samples this would mean spreading the signal over a larger frequency range making the corresponding signal intensity smaller. So we arrive at the conclusion that direct detection of $^{14}N$ NQR by the SQUID is limited to samples with $\eta \approx 0$. Here the magnetic field serves to split the $|+1\rangle$ and $|-1\rangle$ states, analogous to the case of the half odd integer spins (see section 3.3.2).

### 5.2.1 Solid $\alpha$-$N_2$

We have been able to directly detect integer spin NQR in one sample, solid $\alpha$-$N_2$. According to the literature, $\eta$ for this sample is identically or very close to zero. Figure 5.3 shows the $^{14}N$ NQR spectrum of this material in a 35 G field. The resonance frequency was determined to be 3488 ± 2 kHz and agrees well with previous measurements of 3487.73 ± 0.03 kHz at 4.2 K.[92, 93]

The linewidth can be used to place an upper limit on the value of $\eta$. This width comes from two sources; 1) the splitting due to the magnetic field, which is $\gamma B_0$, and 2) the splitting between states due to $\eta$, which is $\frac{e^2qQ}{2h}\eta$. The observed splitting in this spectrum puts an upper limit on the value of $\eta$ of 0.006, which corresponds well to a literature limit from Scott of $\eta < 0.00016$.[93]

## 5.3 Indirect Detection

Because direct detection of $^{14}N$ NQR is limited to circumstances where $\eta = 0$, we need to find a way of indirect detection. It should be noted that the detection of $^{14}N$ NQR through standard means is not typically inhibited by the vanishing magnetic moment but rather by the low frequency of $^{14}N$ transitions (typically < 5 MHz), so indirect methods

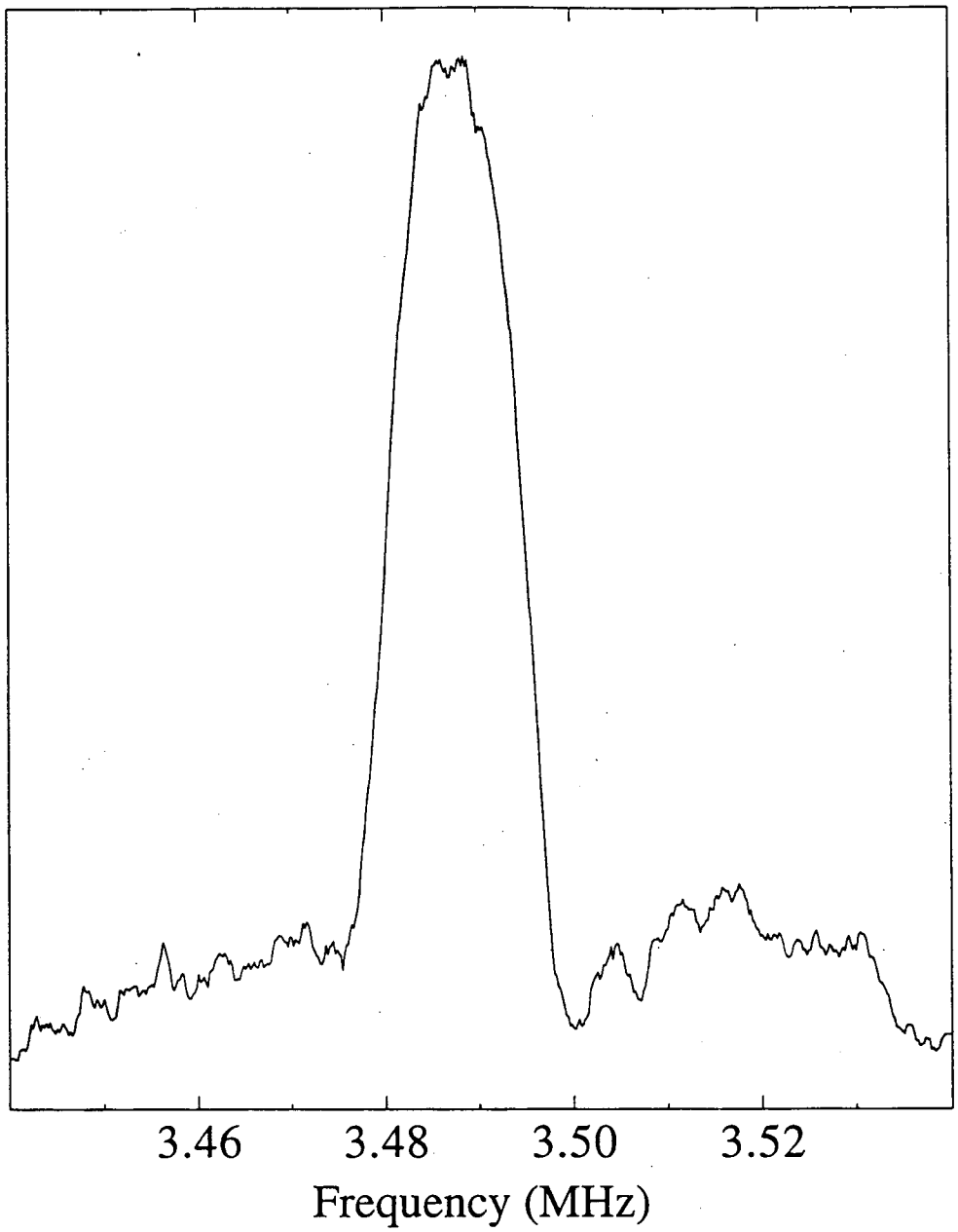


Figure 5.3. Spectrum of solid $\alpha$-$N_2$. This sample was made by blowing nitrogen gas into the sample container which was placed into liquid helium. The very low asymmetry parameter of this sample allows for reasonable signal intensity.

must also be used. Techniques have been developed to study $^{14}N$ NQR using field cycling. Several of the most productive of these techniques exploit level crossings between the proton and the nitrogen spins of a sample during field cycling.[57, 94-97] A typical experiment would involve three phases: 1) preparation, 2) irradiation, and 3) detection.

During the preparation phase the sample is placed in a large magnetic field for a time sufficient for both spin species to reach equilibrium with the lattice (i.e. the proton and nitrogen spin temperatures and the lattice temperature are the same). The sample is then removed from the magnet to an area where the magnetic field is essentially zero. While the field is changing, the proton spins will interact with the nitrogen spins at level crossings. These occur when the proton Zeeman splitting (due to the field) is equal to one of the nitrogen quadrupolar frequencies. When this happens, the heteronuclear dipolar coupling can induce energy conserving spin flips between the two systems. However, since both systems are at the same spin temperature, there can be no net change in the polarization of either spin bath.

At low field, rf irradiation is applied at a specific frequency. If this frequency corresponds to a quadrupolar resonance then the nitrogen spin system will absorb energy. While returning to high field for detection the protons will again interact with the nitrogen spins. If the nitrogen bath has absorbed energy during the irradiation some of that energy will be transferred to the protons during the level crossing.

In the final phase, the proton magnetization is measured at high field. If the irradiation frequency corresponded to a nitrogen quadrupolar transition then the proton magnetization will have decreased due to the energy absorbed during the level crossings. This cycle is repeated with incremental stepping of the irradiation frequency until the entire spectrum is mapped out. Many such cycles must be carried out in order to obtain a single N-14 NQR spectrum.

Other techniques have also been developed that differ from the one described above in either the way of providing contact between the two spin baths or in the property of the

proton spins which is measured during the detection period. However, they all provide a coupling between the protons and the nitrogens and then measure the effect of this coupling on the protons.

Our technique does essentially the same thing, but no longer involves any field cycling. I call it the level matching method. Essentially, we keep the protons in constant contact with the nitrogen spin system during the entire experiment rather then only intermittent contact as in the experiment described above. This is done by picking a magnetic field such that the proton Larmor frequency, $\nu_h$, or a multiple of the Larmor frequency (usually $2\nu_h$) is equal to a nitrogen quadrupolar frequency: $\nu_0$, $\nu_-$, or $\nu_+$.

In this experiment, one of the non level matching NQR transitions is excited with rf. This irradiation changes the population of one of the spin states involved in the level matching transition. Thus the nitrogen spin reservoir associated with the level matching resonance is either heated or cooled. Through cross-relaxation between the nitrogen and nearby protons, mediated by the heteronuclear dipole-dipole interaction, the protons are correspondingly warmed or cooled to finally achieve an equilibrium spin temperature for the level matching states. This change in the magnetization of the protons creates a detectable signal for the SQUID spectrometer. One of the advantages of this method is that the entire spectrum can be obtained in one scan, with, typically, a considerable savings in time over the field cycling methods.

## 5.3.1 Single Sweep

I will begin by describing the simplest of the level matching methods, the single sweep experiment. To describe this mathematically I will begin with a discussion on the concept of spin temperature.

A spin temperature can be mathematically defined for any two level in the following way,[58]

$$\frac{P_1}{P_2} = \exp(-\frac{h\nu_{12}}{kT_{12}}) \qquad 5.14$$

where $P_1$ and $P_2$ are the populations of the two states, $\nu_{12}$ is the frequency difference between states, and $T_{12}$ is the spin temperature of the system. For quadrupolar nuclei, one spin temperature may not describe the entire system. For I=1, a maximum of two spin temperatures are required but at thermal equilibrium only one is needed. In this discussion, the only nitrogen spin temperature that we use is derived from the ratio of the populations of the two states that define the level matching transition.

In NMR, $h\nu \ll kT$ for $T>1K$ so we can use the high temperature limit.[58] This allows the exponential to be expanded in a series where all but the first two terms are ignored. Thus equation 5.14 can be written as

$$\frac{P_1}{P_2} \approx 1 - \frac{h\nu_{12}}{kT_{12}}. \qquad 5.15$$

The spin temperature is then simply

$$\frac{1}{T_{12}} \approx \frac{k}{h\nu_{12}}\left(1 - \frac{P_1}{P_2}\right). \qquad 5.16$$

If cross-relaxation between the proton and nitrogen spin baths is complete, then at all times

$$T_{proton} = T_{nitrogen} \qquad 5.17$$

where $T_{nitrogen}$ is the spin temperature derived from the two level matching states. From equations 5.16 and 5.17 we derive that

$$\frac{1}{\nu_p}(1 - \frac{P_{p1}}{P_{p2}}) = \frac{1}{\nu_n}(1 - \frac{P_{n1}}{P_{n2}}) \qquad 5.18$$

where $\nu_p$ and $\nu_n$ are the proton and nitrogen level matching frequencies respectively and $P_{p1}$, $P_{p2}$, $P_{n1}$, and $P_{n2}$ are the populations of the states involved in the level matching. This will provide a condition for our calculation of the signal intensity below.

For the next part of the discussion I will use the situation shown in Figure 5.4 as an example of a system with N nitrogens and P protons. These results will then lead to generalized solutions. At thermal equilibrium with the lattice we can write the populations of the three nitrogen levels as

$$N_z = \frac{N}{3}, \qquad 5.19a$$

$$N_y = \frac{N}{3}(1\text{-}a), \qquad 5.19b$$

$$N_x = \frac{N}{3}(1\text{-}b) \qquad 5.19c$$

where

$$1\text{-}a = \exp(-\frac{h\nu_-}{kT}) \approx 1 - \frac{h\nu_-}{kT} \qquad 5.20a$$

$$1\text{-}b = \exp(-\frac{h\nu_+}{kT}) \approx 1 - \frac{h\nu_+}{kT}. \qquad 5.20b$$

(Again the high temperature approximation has been used.) The populations of the two proton levels are

$$P_+ = \frac{P}{2} \qquad 5.21a$$

$$P_- = \frac{P}{2}(1\text{-}a). \qquad 5.21b$$

During the experiment the nitrogen $\nu_+$ transition is saturated by rf irradiation thus causing the transfer of $\frac{Ns}{3}$ spins from the $N_z$ level to the $N_x$ level. In the mean time, $\frac{Nr}{3}$ spins will relax from the $N_y$ level to the $N_z$ level as the protons equilibrate the spin temperature by means of cross-relaxation. This will mean that $\frac{PRr}{2}$ spins will be moved from the $P_+$ level to the $P_-$ level where

# Single Sweep

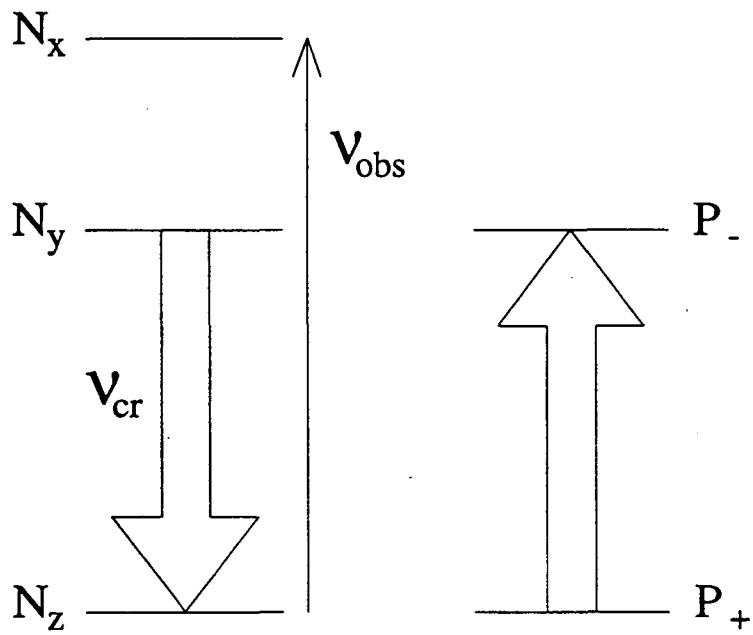


## Populations

| | Before | After |
|---|---|---|
| $N_x$ | N(1 - b)/3 | N(1 - b + s)/3 |
| $N_y$ | N(1 - a)/3 | N(1 - a - r)/3 |
| $N_z$ | N/3 | N(1 - s + r)/3 |
| $P_-$ | P(1 - a)/2 | P(1 - a + Rr)/2 |
| $P_+$ | P/2 | P(1 - Rr)/2 |

Figure 5.4. Example of the single sweep method. In this case, $\nu_+$ is the observed transition and the proton Zeeman frequency is matched to $\nu_-$ to provide efficient cross-relaxation.

$$R = \frac{N}{3}\frac{2}{P} = \frac{2}{3}\frac{N}{P}. \qquad 5.22$$

The final populations, assuming no spin-lattice relaxation, will be

$$N_z = \frac{N}{3}(1\text{-}s+r), \qquad 5.23a$$

$$N_y = \frac{N}{3}(1\text{-}a\text{-}r), \qquad 5.23b$$

$$N_x = \frac{N}{3}(1\text{-}b+s), \qquad 5.23c$$

$$P_- = \frac{P}{2}(1\text{-}a+Rr), \qquad 5.23d$$

$$P_+ = \frac{P}{2}(1\text{-}Rr). \qquad 5.23e$$

Two conditions exist at the end of the experiment. First, due to complete saturation by the rf,

$$N_z = N_x. \qquad 5.24$$

Second, thermal equilibrium between the proton and nitrogen spin baths due to cross-relaxation is maintained. Using equation 5.18 we find that

$$\frac{1}{\nu_h}(1 - \frac{P_-}{P_+}) = \frac{1}{\nu_-}(1 - \frac{N_y}{N_z}). \qquad 5.25$$

In this case, 5.25 reduces to

$$\frac{P_-}{P_+} = \frac{N_y}{N_z} \qquad 5.26$$

because $\nu_h = \nu_-$.

Substituting 5.23a and 5.23b into the first condition leads to

$$\frac{N}{3}(1\text{-}s+r) = \frac{N}{3}(1\text{-}b+s) \qquad 5.27$$

thus

$$s = \frac{(b+r)}{2}. \qquad 5.28$$

The second condition gives

$$\frac{\frac{P}{2}(1-Rr)}{\frac{P}{2}(1-a+Rr)} = \frac{\frac{N}{3}(1-s+r)}{\frac{N}{3}(1-a-r)}. \qquad 5.29$$

Doing the required algebra renders

$$s(1-a+Rr) = r(2-a+2R). \qquad 5.30$$

We realize, however, that the difference in populations in typical NMR experiments are actually very small (in the high temperature limit) which means that a,r<<1. Thus rewriting equation 5.30 and eliminating all the negligible terms gives

$$r = \frac{s}{(2+2R)} \qquad 5.31$$

Combining this result with 5.28 and 5.20b leaves

$$r = \frac{b}{(4R+3)} = \frac{\hbar\nu_+}{kT(4R+3)}. \qquad 5.32$$

$\frac{PRr}{2}$ is the number of proton spins that have flipped and therefore the magnetization change is

$$\Delta M = -\frac{\gamma\hbar PRr}{2} = -\frac{\gamma\hbar^2 PR\nu_+}{2kT(4R+3)}$$

$$= -\frac{\gamma\hbar^2 PR}{2}\frac{3}{4}\frac{e^2qQ(1+\frac{\eta}{3})}{kT(4R+3)}. \qquad 5.33$$

Thus,

$$\Delta M \propto \nu_+. \qquad 5.34$$

The generalization of this formula is

$$\Delta M \propto \pm\nu_{obs} \qquad 5.35$$

where the sign of the magnetization change is positive if $\nu_{obs}$ or $\nu_{cr}$ is $\nu_+$. The solid lines in Figure 5.5 display the calculated relative intensities in all experimental cases. Figure 5.6 is a spectrum of the $\nu_-$ (1972 ± 4 kHz) and $\nu_+$ (2590 ± 3 kHz) transitions of glycyl-glycine. This sample demonstrates both the method and the sign difference expected for different combinations of irradiation and level matching frequencies.

This calculation assumes that cross-relaxation amongst the protons and between the proton and nitrogen spin baths is faster than the time scale of the sweep through resonance. Where this does not occur, the full expected intensities of the signals will not be realized. This means that the ideal operating procedure for the spectrometer is to use long sweep times and as much rf power as possible.

## 5.3.2 Single Sweep ($\nu_{cr} = 2\nu_h$)

If, instead of the nitrogen level matching resonance equaling $\nu_h$, it matches $2\nu_h$ the following adjustments must be made to the derivation. Assuming the situation in Figure 5.7, the original populations (equations 5.19a-c and 5.21a) remain the same except

$$P_- = \frac{P}{2}(1-\frac{a}{2}). \qquad 5.21b'$$

The final populations, with $\frac{Ns}{3}$ spins transferred by the saturating rf, and $\frac{Nr}{3}$ spins relaxing in the nitrogen spin bath leaves the nitrogen spin populations (5.23a-c) the same but now

$$P_- = \frac{P}{2}(1-\frac{a}{2}+2Rr), \qquad 5.23d'$$

$$P_+ = \frac{P}{2}(1-2Rr). \qquad 5.23e'$$

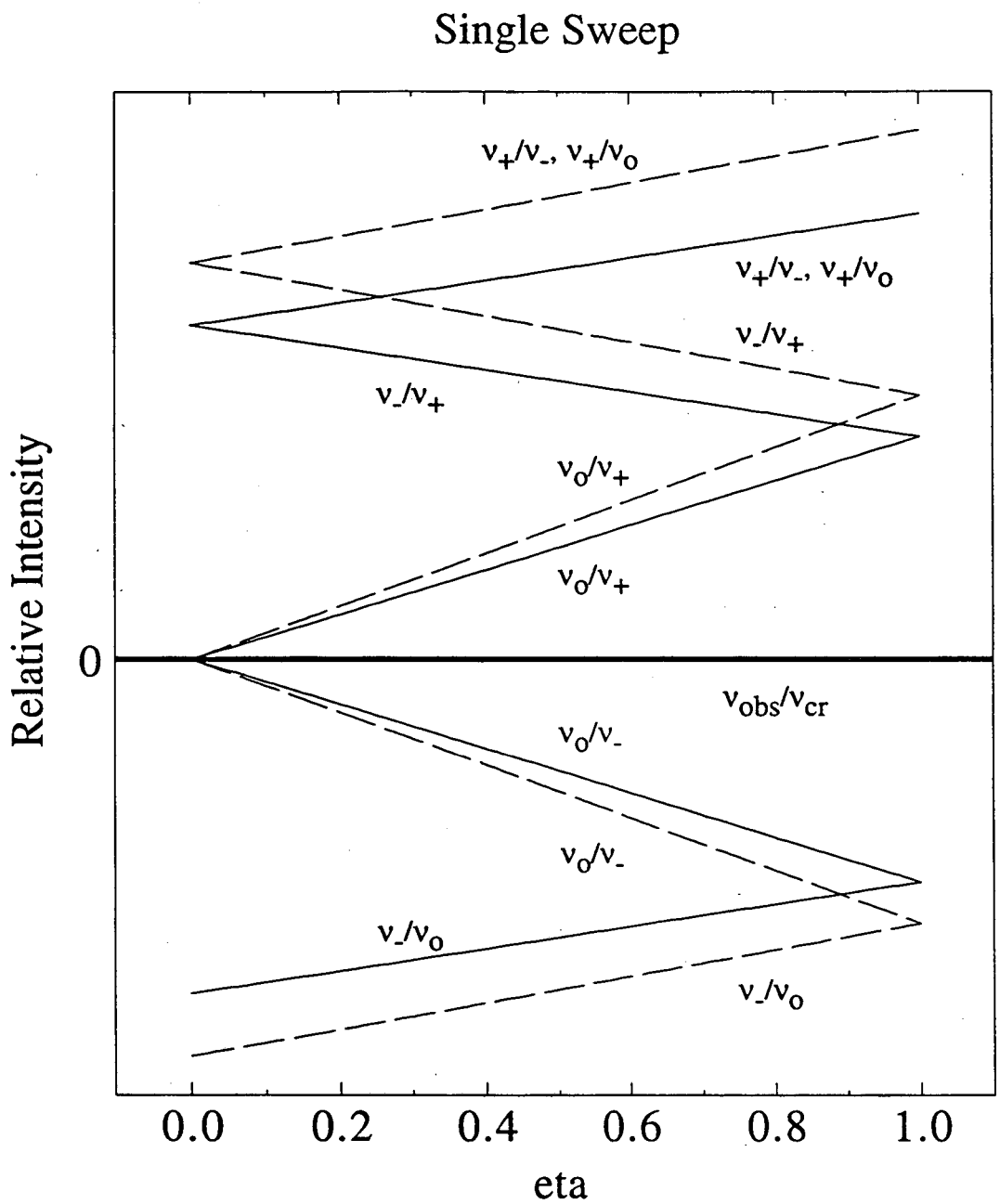


Figure 5.5. A plot of the relative intensities as calculated in sections 5.3.1 (solid lines) and 5.3.2 (dotted lines) for all different combinations of cross relaxing and observed transitions.

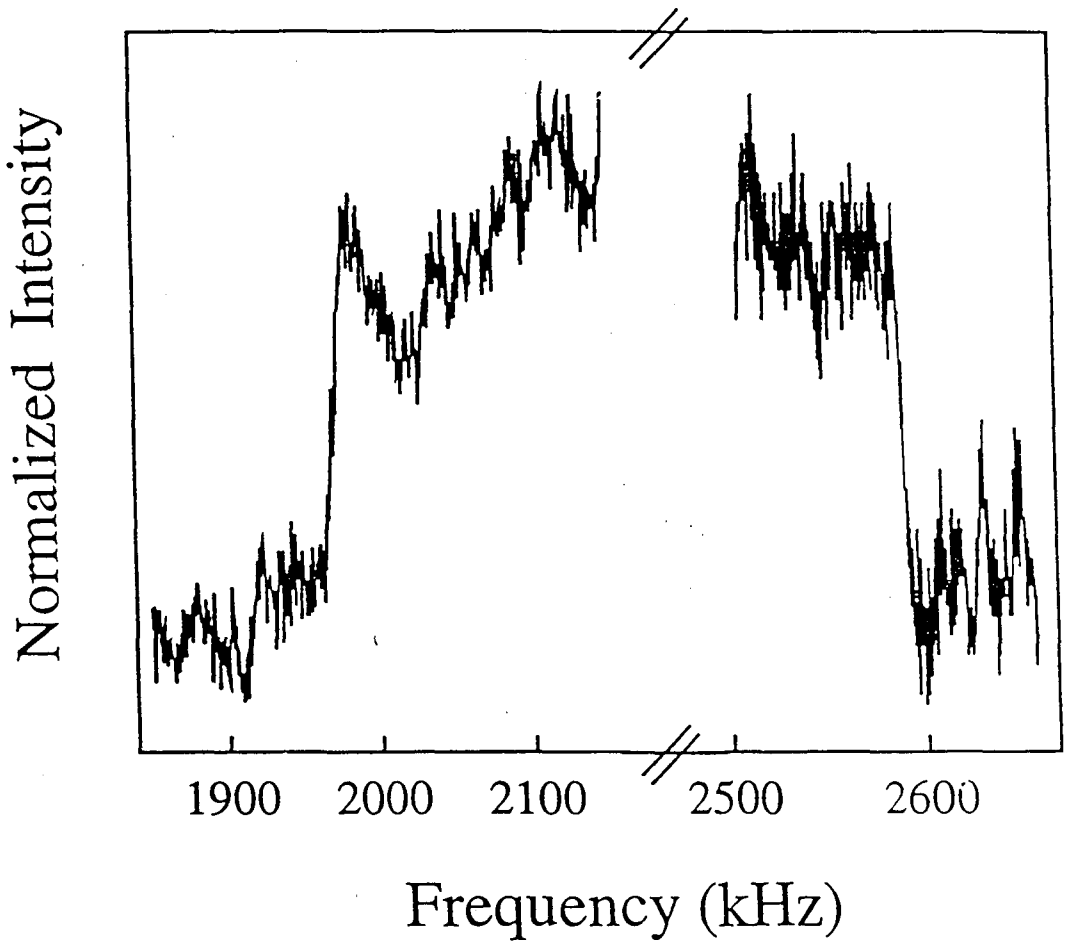


Figure 5.6. Spectra of diglycine taken by level matching the proton Larmor frequency with the $\nu_0$ frequency (618 kHz) of the amino acid nitrogen and sweeping over the $\nu_-$ (1972 kHz) and $\nu_+$ (2590 kHz) transitions.

# Single Sweep

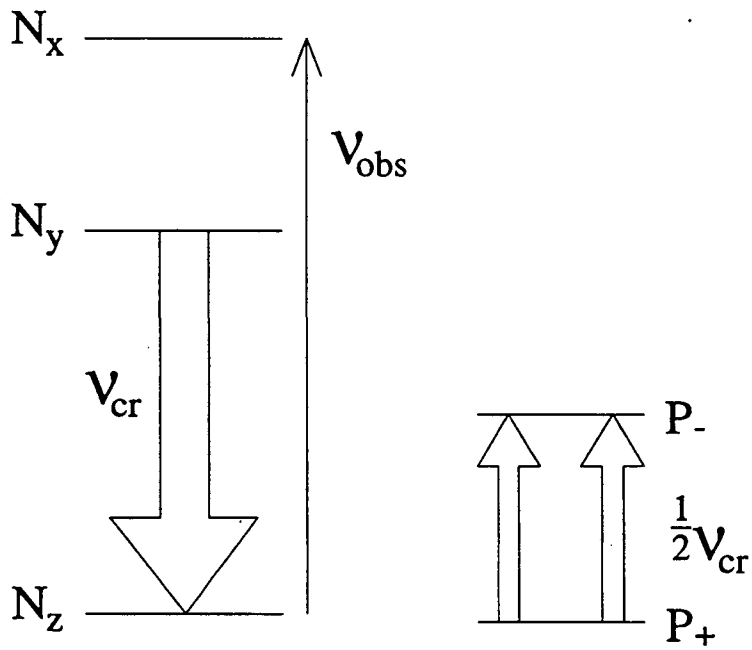


## Populations

| | Before | After |
|---|---|---|
| $N_x$ | N(1 - b)/3 | N(1 - b + s)/3 |
| $N_y$ | N(1 - a)/3 | N(1 - a - r)/3 |
| $N_z$ | N/3 | N(1 - s + r)/3 |
| $P_-$ | P(1 - a/2)/2 | P(1 - a/2 + 2Rr)/2 |
| $P_+$ | P/2 | P(1 - 2Rr)/2 |

Figure 5.7. Example of the single sweep method. In this case, $\nu_+$ is the observed transition and twice the proton Zeeman frequency is matched to $\nu_-$ to provide efficient cross-relaxation.

This is because two proton spins must now flip for every nitrogen spin relaxed. The saturation condition (eq. 5.24) is still met so equations 5.27 and 5.28 are correct. But the thermal equilibrium condition is

$$2(1 - \frac{P_-}{P_+}) = (1 - \frac{N_y}{N_z}) \qquad 5.25'$$

because $\nu_- = 2\nu_h$. Substitution of the populations gives

$$2(1 - \frac{\frac{P}{2}(1 - \frac{a}{2} + 2Rr)}{\frac{P}{2}(1 - 2Rr)}) = (1 - \frac{\frac{N}{3}(1 - a - r)}{\frac{N}{3}(1 - s + r)}). \qquad 5.29'$$

Working out the complex fractions produces

$$2(\frac{\frac{a}{2} - 4Rr}{1 - 2Rr}) = (\frac{a + 2r - s}{1 - s + r}). \qquad 5.30'$$

Again, r,s<<1 so this leaves

$$a - 8Rr = a + 2r - s \qquad 5.36$$

or

$$r = \frac{s}{8R + 2}. \qquad 5.31'$$

This leads to

$$r = \frac{b}{16R + 3}. \qquad 5.32'$$

The magnetization change due to the $\frac{2rRP}{2}$ proton spins that flip is then

$$\Delta M_{2vh} = -\gamma \hbar PrR = -\frac{\gamma \hbar^2 PR\nu_+}{kT(16R+3)}. \qquad 5.33'$$

Comparing this to equation 5.33 gives

$$\Delta M_{2\nu h} = \Delta M_{\nu h} \frac{2(4R + 3)}{16R + 3} \qquad 5.37$$

This will lead to a slight increase in signal as displayed in by the dotted lines in Figure 5.5. Because absolute intensity measurements are not very accurate with the SQUID system this slight increase has not been observed. It should also be noted that the transition matrix elements for this experiment should be smaller than in the previous case because higher order terms in the dipolar interaction would be needed, namely those involving 3 spins: 2 protons and 1 nitrogen. Thus the actual final intensities may be reduced.

## 5.3.3 Double Sweep

The next two methods are attempts to increase the signal intensity by also irradiating the third transition in the nitrogen spin system. These experiments are meant to accomplish two objectives. First, by increasing the signal intensity we will be able to observe weak signals such as the $\nu_0$ transition. Because intensity is proportional to frequency, the $\nu_0$ line usually is very weak due to its low frequency (typically 100 - 600 kHz) as confirmed in Figure 5.5.

The second goal is to connect transitions that are from the same nitrogen site. Polypeptides and even some amino acids have more than one nitrogen site, so it will be important to match transitions from the same nitrogen in order to calculate the quadrupolar parameters. This is easily done if the intensity of the signals can be selectively modified.

The double sweep method utilizes a sweep first through one resonance and then through the other while detecting the resultant signal as shown in Figure 5.8. In this case, $\nu_+$ is irradiated first and at the end of that sweep the final conditions in section 5.3.1 are achieved. Now $\nu_0$ is swept. $\frac{Ns'}{3}$ spins are transferred due to the rf and $\frac{Nr'}{3}$ spins are relaxed by the protons. At the end of this sweep, assuming no spin-lattice relaxation, the final populations are

# Double Sweep

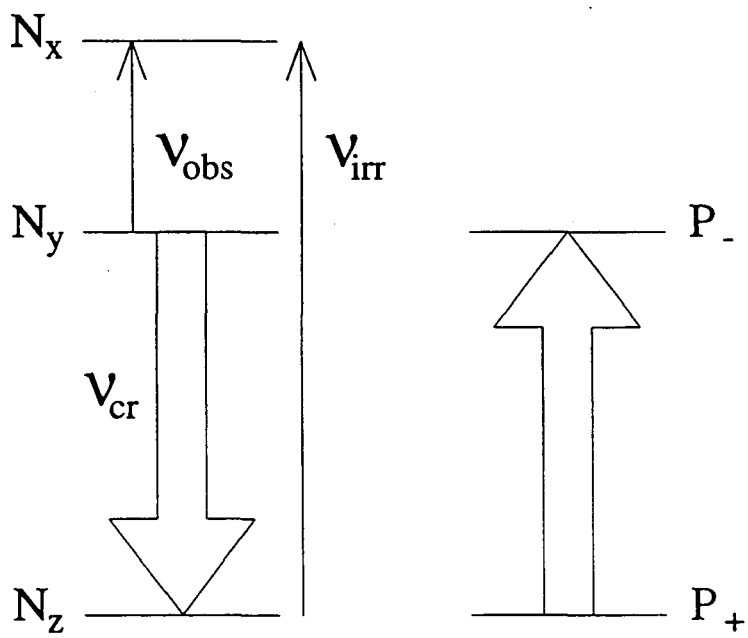


Populations

| | Before | Intermediate | After |
|---|---|---|---|
| $N_x$ | N(1 - b)/3 | N(1 - b + s)/3 | N(1 - b + s + s')/3 |
| $N_y$ | N(1 - a)/3 | N(1 - a - r)/3 | N(1 - a - s' - r - r')/3 |
| $N_z$ | N/3 | N(1 -s + r)/3 | N(1 - s + r + r') /3 |
| $P_-$ | P(1 - a)/2 | P(1 - a + Rr)/2 | P(1 - a + Rr + Rr')/2 |
| $P_+$ | P/2 | P(1 - Rr)/2 | P(1 - Rr - Rr')/2 |

Figure 5.8. Example of the double sweep method. In this case, $\nu_+$ is swept first and following that we sweep through $\nu_0$ for observation. The proton Zeeman frequency is matched to $\nu_-$ to provide efficient cross-relaxation.

$$N_z = \frac{N}{3}(1\text{-}s+r+r'), \qquad 5.23a''$$

$$N_y = \frac{N}{3}(1\text{-}a\text{-}r\text{-}r'\text{-}s'), \qquad 5.23b''$$

$$N_x = \frac{N}{3}(1\text{-}b+s+s'), \qquad 5.23c''$$

$$P_- = \frac{P}{2}(1\text{-}a+Rr+Rr'), \qquad 5.23d''$$

$$P_+ = \frac{P}{2}(1\text{-}Rr\text{-}Rr'). \qquad 5.23e''$$

The final conditions will be

$$N_y = N_x. \qquad 5.24''$$

$$\frac{1}{\nu_h}(1 - \frac{P_-}{P_+}) = \frac{1}{\nu_-}(1 - \frac{N_y}{N_z}). \qquad 5.25''$$

The same mathematics as applied in the previous section leads to

$$r = \frac{-(b\text{-}a) + \frac{b(2R+3)}{4R+3}}{(4R+3)}. \qquad 5.32''$$

So

$$\Delta M = -\frac{\gamma\hbar PrR}{2} = -\frac{\gamma\hbar^2 PR}{2kT}\left(\frac{-\nu_0 + \frac{2R+3}{4R+3}\nu_+}{4R+3}\right) \qquad 5.33''$$

The generalization of this formula is

$$\Delta M = -\frac{\gamma\hbar^2 PR}{2kT}\left(\frac{\pm\nu_{obs} \pm \frac{2R+3}{4R+3}\nu_{irr}}{4R+3}\right). \qquad 5.35''$$

The first sign is negative if $\nu_{obs}$ and $\nu_{cr}$ are a combination of $\nu_-$ and $\nu_0$. The second sign is negative if $\nu_{obs}$ is $\nu_+$ . A comparison of these intensities with those from the original method is shown by the dotted lines in Figure 5.9. An analysis of this figure indicates that in some, but not all, cases the signal is enhanced. This has not yet been confirmed experimentally.

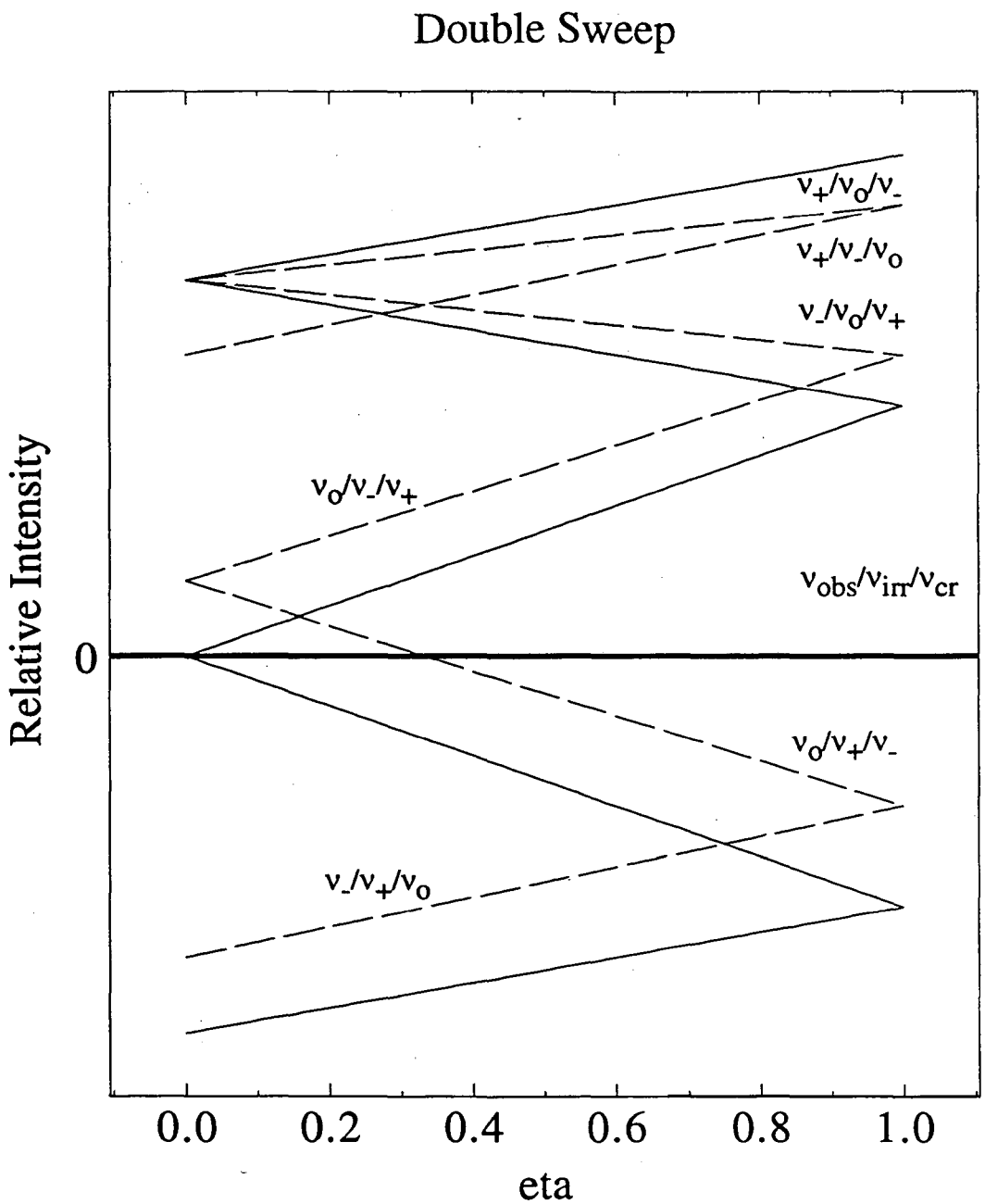


Figure 5.9. A plot of the relative intensities as calculated for the single sweep (solid lines) and double sweep (dotted lines) methods for all different combinations.

## 5.3.4 Double Irradiation

When two transition frequencies have been elucidated then another type of experiment can be done, namely double irradiation. This method enhances the intensity of any resonance and so can be used to detect difficult to find transitions (usually $\nu_0$ because of its low frequency and therefore low intensity) and also to connect transitions when more then one nitrogen site is present in the material.

In this experiment, shown in Figure 5.10, two rf irradiation frequencies are used. One, $\nu_{irr}$, is held constant at the frequency of a known transition. This transition is saturated before and during the experiment. The second rf channel is swept through a range containing the unknown or possibly connected resonance. Thus, we simultaneously irradiate the two non-level matching transitions. This leads to the following conditions:

$$N_z = N_x, \qquad 5.38a$$

$$N_x = N_y, \qquad 5.38b$$

$$\frac{P_-}{P_+} = \frac{N_y}{N_z} = 1. \qquad 5.38c$$

The proton spins are entirely saturated in the experiment, if we assume complete cross-relaxation. Thus the final populations of the states at the end of the experiment are

$$N_x = N_y = N_z = \frac{N}{3} \qquad 5.39a$$

$$P_+ = P_- = \frac{P}{2}. \qquad 5.39b$$

The number of proton spins flipped during detection is then the difference between the final population and the population after irradiation of $\nu_{irr}$:

$$P_-(\text{end}) - P_-(\text{intermediate}) = \frac{P}{2}\left(a - \frac{Rb}{4R + 3}\right). \qquad 5.40$$

# Double Irradiation

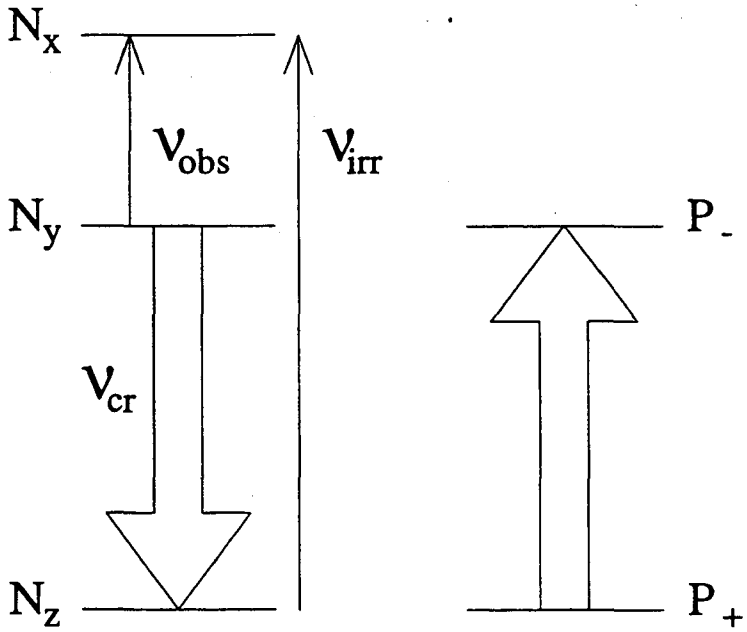


Populations

| | Before | Intermediate | After |
|---|---|---|---|
| $N_x$ | N(1 - b)/3 | N(1 - b + s)/3 | N/3 |
| $N_y$ | N(1 - a)/3 | N(1 - a - r)/3 | N/3 |
| $N_z$ | N/3 | N(1 -s + r)/3 | N/3 |
| $P_-$ | P(1 - a)/2 | P(1 - a + Rr)/2 | P/2 |
| $P_+$ | P/2 | P(1 - Rr)/2 | P/2 |

Figure 5.10. Example of the double irradiation method. In this case, $\nu_+$ is irradiated before and during the sweep through $\nu_0$ for observation. The proton Zeeman frequency is matched to $\nu_-$ to provide efficient cross-relaxation.

Thus the final magnetization is

$$\Delta M = -\frac{\gamma\hbar^2 PR}{2kT}\left(\nu_- - \frac{R\nu_+}{4R+3}\right) \qquad 5.33'''$$

and the generalized formula is

$$\Delta M = -\frac{\gamma\hbar^2 PR}{2kT}\left(\nu_{cr} \pm \frac{R\nu_{irr}}{4R+3}\right) \qquad 5.35'''$$

the minus sign occurring when $\nu_{cr}$ and $\nu_{irr}$ are a combination of $\nu_-$ and $\nu_0$. These intensities are compared to those for the single sweep method in Figure 5.11. The full effect of this enhancement has not been observed experimentally, but a significant increase in signal intensity has been seen as presented in Figure 5.12.

## 5.3.5 Level Matching Conditions

Figure 5.13 shows a series of derivative spectra of L-serine taken at different fields (the broadest transition is at twice the proton Larmor frequency, $2\nu_h$, which is proportional to the magnetic field strength). It demonstrates two possible level matching conditions. The first situation is where the proton frequency exactly matches the nitrogen quadrupolar frequency. In this case, the level matching transition is completely overwhelmed by the proton signal, but the other resonances are clearly visible.

In the second case, the frequency of the level matching transition deviates, within the range of the dipolar interaction of the protons, from the proton Zeeman splitting. Here the level matching signal can often be observed, especially if it is swept before saturating the proton resonance. Usually cross-relaxation is efficient enough to detect the other transitions. This allows us to find resonances although the exact level matching condition is not met and therefore makes the experiment less rigid as far as choice of magnetic field strength.

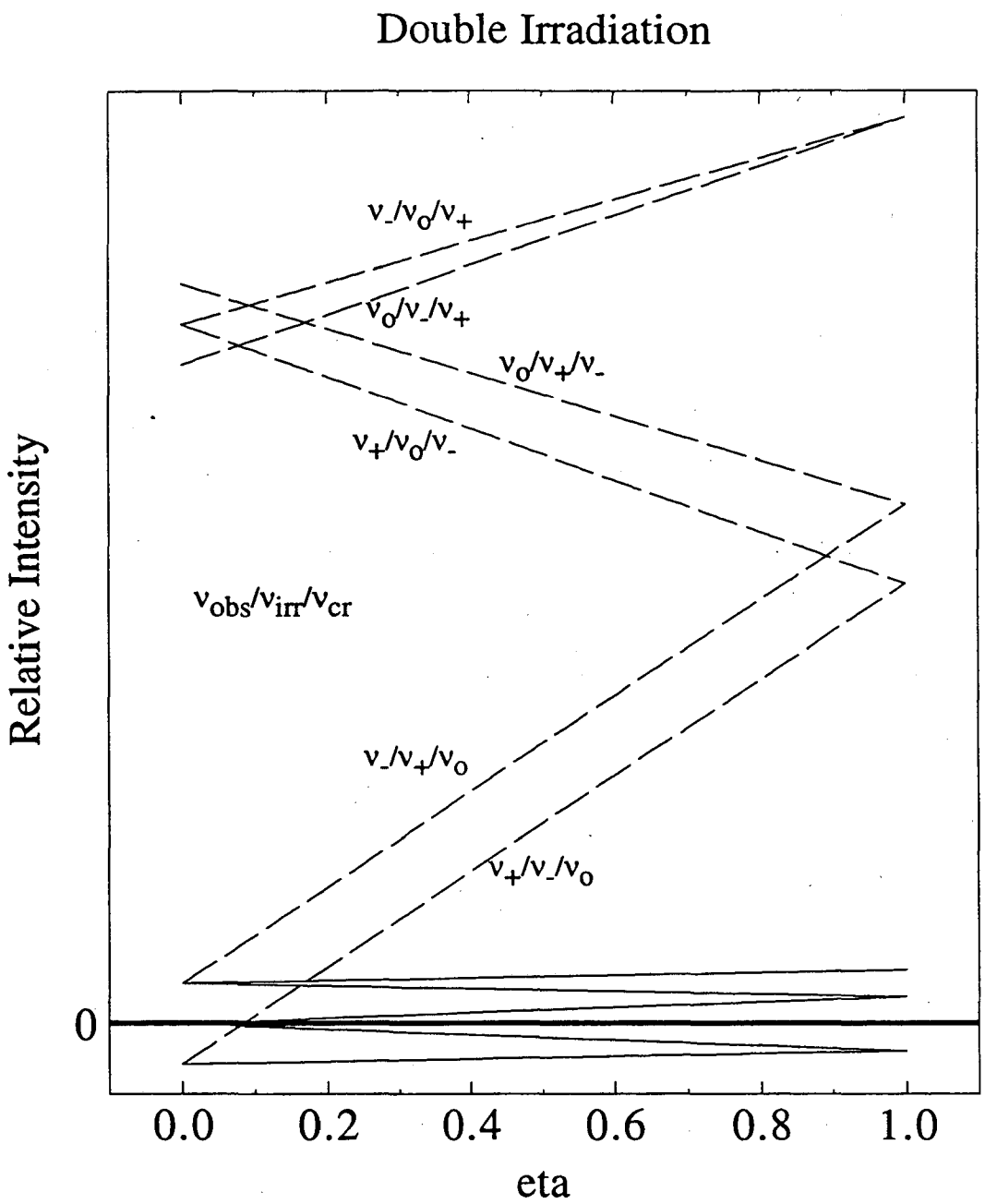


Figure 5.11. A plot of the relative intensities as calculated for the single sweep (solid lines) and double irradiation (dotted lines) methods for all different combinations.

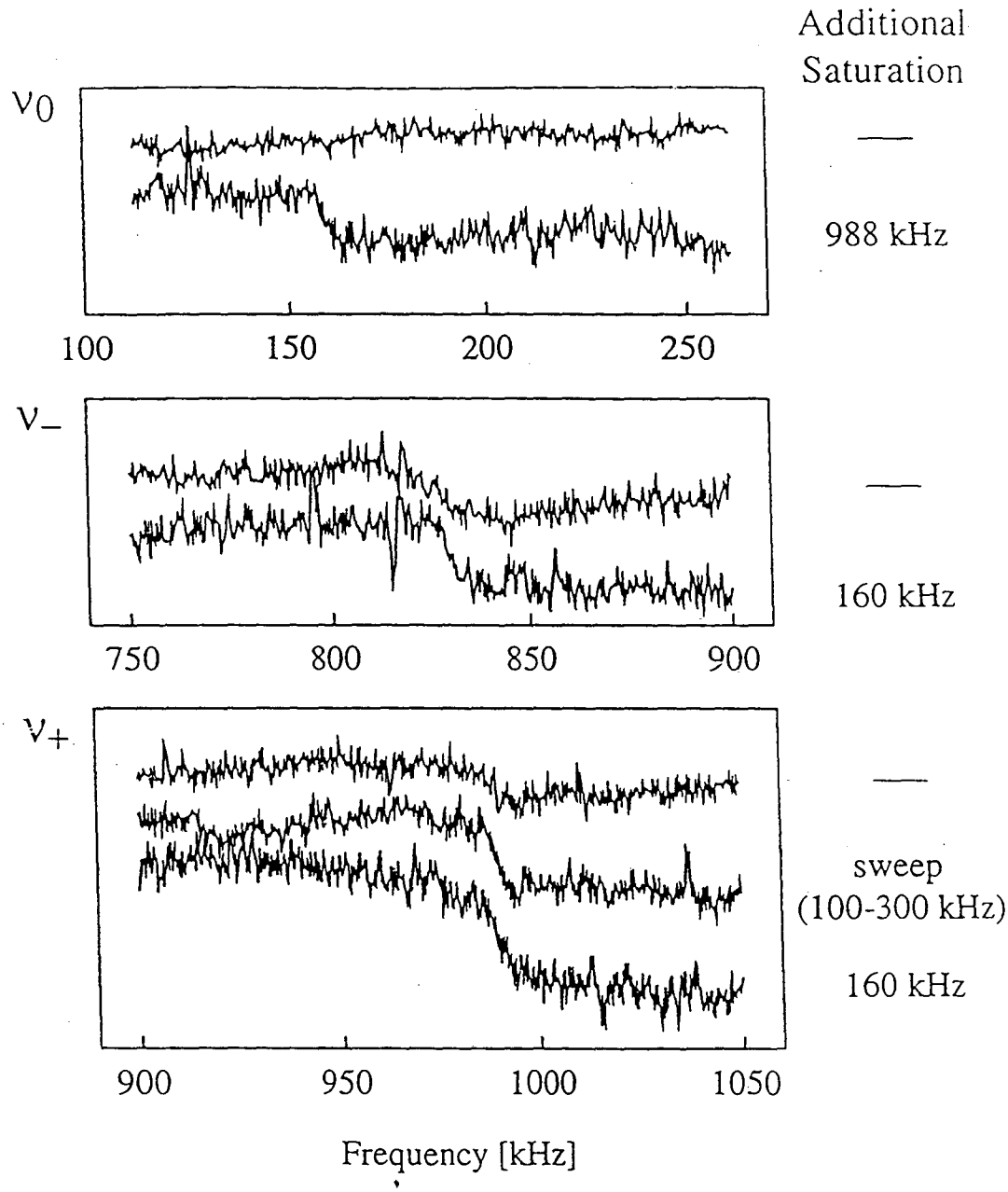


Figure 5.12. Comparison of the three nitrogen transitions of L-alanine ( $\nu_0$ = 160 kHz, $\nu_-$ = 828 kHz, and $\nu_+$ = 988 kHz) under single and double irradiation.

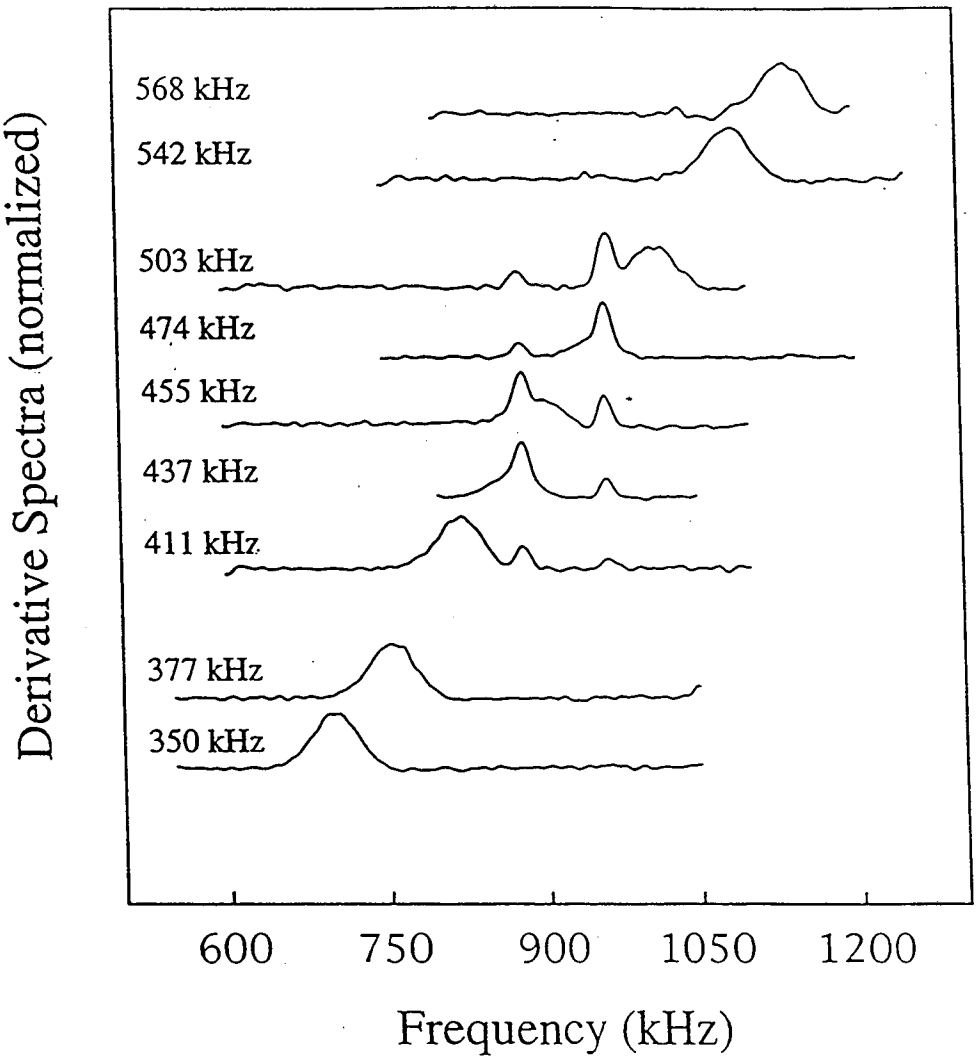


Figure 5.13. Derivative spectra of DL-serine for different magnetic field strengths. The broad proton line appears at double the Larmor frequency. The nitrogen transitions, $\nu_-$ (882 kHz) and $\nu_+$ (961 kHz) become visible near level matching.

## 5.4 Experimental Results

Tables 5.2 and 5.3 provide a list of the $^{14}N$ NQR resonances that we have obtained up to this time. Also included are field cycling measurements at 77 K from the literature.[57, 98-102] It can be seen that the agreement is quite good. Most of those resonances are below 2 MHz, a frequency range where standard NQR experiments don't work. However, first I wish to mention some higher frequency experiments.

The first $^{14}N$ NQR resonances measured by this method were those for a urea inclusion compound with octanoic acid. The measured quadrupole parameters for this compound are $C_Q = 3487 \pm 20$ kHz and $\eta = 0.344 \pm 0.011$. These compares well with urea at 77 K ($C_Q = 3507$ and $\eta = 0.323$).[103] The other two high frequency compounds are pyridine ($C_Q = 5216 \pm 6$ kHz, $\eta = 0.019 \pm 0.002$) and uracil. For uracil,[100, 104] a nucleic base used in DNA, the two resonances observed correspond to $\nu_+$ for different nitrogen sites as described by Edmonds.[100] The parameters of these three materials are typical NH and $NH_2$ values.

Amino acids provide good examples of $NH_3^+$ groups which typically have $C_Q \approx$ 1.0 - 1.5 MHz and $\eta < 0.2$.[102] Thus the resonance frequencies are less then 1300 kHz. These types of resonances are difficult to observe except with the SQUID spectrometer or field cycling experiments.

When there are several nitrogens per molecule it becomes imperative to try and assign the lines to specific sites. One useful tool is symmetry. An $NH_3^+$ group has a $C_3$ axis along its bond to the carbon skeleton. This translates into $\eta = 0$ for that site (see section 3.1.1).[102] This situation only occurs for a perfectly tetrahedral $NH_3^+$ group. However, referring to Tables 5.2 and 5.3, we find that most of the $NH_3^+$ groups have $\eta <$ 0.2 making them easy to spot as opposed to other sites. Alanine, histidine, and serine provide good examples of the near tetrahedral $NH_3^+$ group.

| Name | Site | $\nu_+$ (kHz) | $\nu_-$ (kHz) | $\nu_0$ (kHz) | $C_Q$ (kHz) | $\eta$ | Ref. | T(K) |
|---|---|---|---|---|---|---|---|---|
| L-Alanine | $NH_3^+$ | 988 ± 3 | 828 ± 10 | 160 ± 3 | 1208 ± 3 | 0.267 ± 0.005 | | 4.2 |
| | | (982) | (825) | | (1205) | (0.261) | 57 | (77) |
| Glycine | $NH_3^+$ | 1099 ± 2 | 782 ± 3 | — | 1254 ± 3 | 0.506 ± 0.005 | | 4.2 |
| | | (1093) | (780) | (313) | (1249) | (0.501) | 57 | (77) |
| L-Histidine | $NH_3^+$ | 1032 ± 5 | 939 ± 5 | — | 1314 ± 5 | 0.142 ± 0.008 | | 4.2 |
| | (mono) | (1025) | (932) | | (1305) | (0.143) | 57 | (77) |
| | $NH_3^+$ | 984 ± 6 | 908 ± 4 | — | 1261 ± 5 | 0.121 ± 0.008 | | 4.2 |
| | (ortho) | (974) | (903) | | (1251) | (0.113) | 57 | (77) |
| | NH | 1412 ± 4 | — | — | — | — | | 4.2 |
| | | (1406) | (749) | (657) | (1437) | (0.915) | 57 | (77) |
| D-Serine | $NH_3^+$ | 976 ± 4 | 859 ± 2 | 116 ± 8 | 1223 ± 3 | 0.190 ± 0.005 | | 4.2 |
| L-Serine | $NH_3^+$ | 977 ± 3 | 860 ± 3 | — | 1225 ± 3 | 0.191 ± 0.005 | | 4.2 |
| | | (967.5) | (855.5) | | (1215) | (0.184) | 57 | (77) |
| DL-Serine | $NH_3^+$ | 961 ± 3 | 882 ± 3 | — | 1227 ± 3 | 0.128 ± 0.005 | | 4.2 |
| | | (949) | (875) | | (1217) | (0.118) | 57 | (77) |

Table 5.1 Amino Acid $^{14}N$ results. Literature values are given in parentheses below our experimental results.

| Name | Site | $\nu_+$ (kHz) | $\nu_-$ (kHz) | $\nu_0$ (kHz) | $C_Q$ (kHz) | $\eta$ | Ref. | T(K) |
|---|---|---|---|---|---|---|---|---|
| Diglycine | $NH_3^+$ | 2590 ± 3 | 1972 ± 3 | — | 3041 ± 3 | 0.407 ± 0.005 | | 4.2 |
| | | (2585) | (1975) | (620) | (3030) | (0.41) | 57 | (77) |
| | NH | 1058 ± 3 | — | — | — | — | | 4.2 |
| | | (1090) | — | (260) | (1280) | (0.41) | 57 | (77) |
| Triglycine | ? | 1167 ± 6 | | | | | | 4.2 |
| | ? | 898 ± 8 | | | | | | 4.2 |
| | ? | 843 ± 7 | | | | | | 4.2 |
| | NH | (2900) | | (1175) | (3080) | (0.76) | 57 | (77) |
| | NH | (2620) | | (720) | (3010) | (0.48) | 57 | (77) |
| | $NH_3^+$ | (1025) | | (275) | (1180) | (0.46) | 57 | (77) |
| L-alanyl-L-histidine | $NH_3^+$ | 1203 ± 6 | 933 ± 4 | — | 1424 ± 5 | 0.379 ± 0.007 | | 4.2 |
| | $NH_3^+$ | 1160 ± 3 | 834 ± 4 | 327 ± 5 | 1329 ± 4 | 0.491 ± 0.006 | | 4.2 |
| | NH | 1550 ± 3 | — | — | — | — | | 4.2 |
| | NH | 1477 ± 3 | — | 524 ± 7 | 1620 ± 6 | 0.647 ± 0.008 | | 4.2 |
| L-alanyl-diglycine | $NH_3^+$ | 1033 ± 13 | 837 ± 5 | 183 ± 6 | 1247 ± 9 | 0.314 ± 0.014 | | 4.2 |
| Urea/Octanoic Acid | Urea | 2915 ± 20 | 2315 ± 20 | — | 3487 ± 20 | 0.344 ± 0.011 | | 4.2 |
| Pyridine | | 3937 ± 7 | 3887 ± 5 | — | 5216 ± 6 | 0.019 ± 0.002 | | 4.2 |
| Uracil | NH | 2318 ± 7 | — | — | — | — | | 4.2 |
| | | (2320) | (1585) | (740) | (2600) | (0.569) | 57 | (77) |
| | NH | 2285 ± 5 | — | — | — | — | | 4.2 |
| | | (2290) | (1620) | (675) | (2600) | (0.519) | 57 | (77) |

Table 5.2 Polypeptide and other $^{14}N$ results. Literature values are given in parentheses below our experimental results.

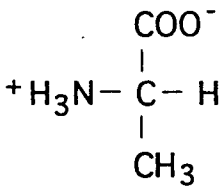

Alanine

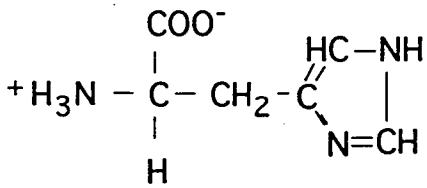

Histidine

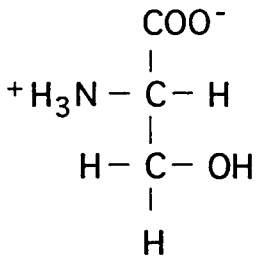

Serine

We investigated D-, L-, and DL-serine in order to confirm an hypothesis about the crystal structures of these compounds. D and L isomers are simply mirror images of one another so one would expect to see crystal structures that are also mirror images. For the quadrupolar interaction this should make no difference and thus the quadrupolar parameters should be the same. This is confirmed by D- and L-serine. However, for DL-serine, which is a racemic mixture of D and L isomers, the crystal structure should be significantly altered to accommodate both molecules. This change in crystal structure should have an impact on the quadrupolar parameters, which is also confirmed by our results. This is another indication of the importance of crystal structure in the quadrupolar interaction and illustrates the type of information that we can obtain.

Another interesting sample is L-histidine because it has three nitrogens per molecule. Quadrupolar transitions for both the $NH_3^+$ and the NH groups have been observed. No resonances arising from the ring nitrogen with no attached protons have been detected probably because it does not have very efficient cross-relaxation with any nearby protons. Perhaps slower sweeps and more rf power might help in detecting these kinds of resonances. Only one transition for the NH group has been measured but the level matching requirement for that experiment implies that $\nu_- \approx \nu_0$ so $\eta \approx 1$. We are unsure why we can not detect the $\nu_-$ and $\nu_0$ transitions, but work is continuing in this regard.

The four $NH_3^+$ resonances in this sample imply two separate sites. Edmonds also observes these signals for certain preparations of histidine.[101] He explains that the sample

is a mixture of two crystal structures: monoclinic and orthorhombic. They were able to obtain a pure orthorhombic sample and from that assign the resonances to the corresponding structure. We follow their assignment. This sample could provide a perfect opportunity to use the double irradiation technique to connect transitions.

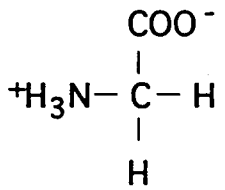

Glycine

Glycine seems to break the pattern of $NH_3^+$ groups with $\eta <$ 0.2. A look at the crystal structure, however, explains the difference. Two of the protons in the $NH_3^+$ group are strongly hydrogen bonded to neighboring molecules, however the third proton participates in a weaker bifurcated hydrogen bond with two adjoining molecules.[102, 105] Thus the three protons are no longer equivalent and the $C_3$ axis symmetry does not exist. This again confirms the fact that crystal structure can often have a profound impact on quadrupolar parameters.

The next step on the way to proteins is polypeptides. We have studied several di- and tripeptides with mixed success. The problems here arise from several sources. First, the intensity of the signal is decreased by the increased size of the molecule. Fewer nitrogens from a given site are found in the sample. Second, there is more than one nitrogen site in the sample and therefore there are many resonances which must be assigned. Despite the predictions made in the theoretical section there has been only limited success in connecting resonances from the same site. However, our ability to conduct these experiments is increasing and should result in easier assignments.

The first attempts at polypeptides were di- and triglycine.[99] Diglycine resonances were found at 2590 ± 3 kHz, 1972 ± 3 kHz, and 1058 ± 3 kHz. The first two are assigned to the bridging nitrogen bond based on comparison with typical NH quadrupolar parameters. We also expect that the terminal diglycine nitrogen should have quadrupolar splittings similar to those for glycine and the third resonance fits that profile. Unfortunately, the $\nu_-$ and $\nu_0$ transitions have not yet been observed for the terminal

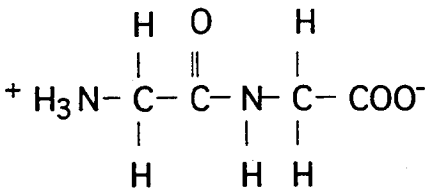

Diglycine

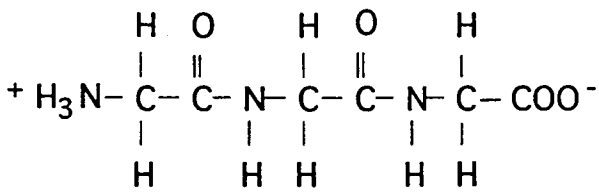

Triglycine

nitrogen so we are not able to compare the quadrupolar parameters of this sample with those of glycine.

Triglycine has proven to be a difficult sample. Long spin-lattice relaxation times have prevented us from averaging scans and until now resonances have been found only at 1167 ± 6 kHz, 898 ± 8 kHz, and 843 ± 7 kHz. Early conjecture would place the 1167 resonance and one of the other two as terminal glycine nitrogen signals, because that would be similar to glycine itself. The other resonances would be $\nu_-$ or $\nu_0$ (for a large $\eta$ site) of a bridging nitrogen.

L-alanyl-L-histidine has proven to be a much better sample. We have observed several transitions. My coworkers, Marcia Ziegeweid and Ulrike Werner, have recently proposed connections between the resonances (see Table 5.2). Their analysis indicates that there are two distinct $NH_3^+$ groups in this sample. This would imply that there are two

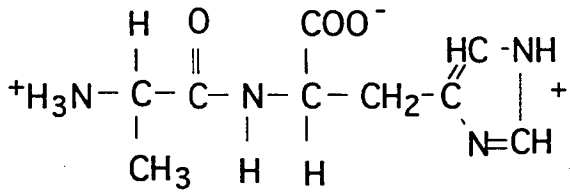

Alanyl-Histidine

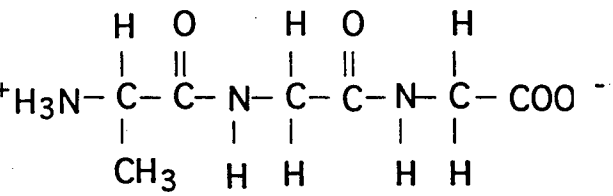

Alanyl-Diglycine

distinct lattice sites as there is only one $NH_3^+$ group in the molecule (the terminal alanine nitrogen). In addition they have identified two NH groups which could either be the bridging amino group of histidine or one of the nitrogens in the histidine ring. This model indicates that there are still several nitrogens and their resonances to be found in order to

provide a final assignment. Also, a crystal structure of this sample would be helpful in confirming the existence of two lattice sites.

Finally, we have been able to find resonances from the $NH_3^+$ site in L-alanyl-diglycine. Unfortunately, we have not observed transitions from either of the glycine nitrogens and a further search for these resonances is warranted.

The di- and tripeptides are a step towards biologically important molecules. Realistically, however, it must be noted that many of these resonances occur in the same frequency range (100-1300 kHz for terminal nitrogens and 700-3000 kHz for bridging nitrogens). Thus significant overlap of transitions would occur with larger molecules. Also, assignment of the nitrogen site to a specific amino acid residue may be difficult, again because of the overlap in the frequency range. These problems must be resolved for $^{14}N$ NQR to be useful in biological molecules.

As indicated by the incomplete list of resonances for several of these samples, much work remains to perfect the technique. This is, however, an important beginning for the study of $^{14}N$ NQR by the SQUID spectrometer.

# Chapter 6
# SQUID NMR and Methyl Quantum Tunneling

Methyl quantum tunneling provides an important example of quantum processes in molecules. It has been widely studied by inelastic neutron scattering (INS)[106] and NMR.[23] In this chapter I will show how we use the SQUID spectrometer to measure tunneling splittings and discuss the advantages of this approach as compared to the field cycling method. I will also present a correlation between the microscopic methyl tunneling splittings and macroscopic thermodynamic properties. This correlation may then be used to learn about the surroundings and interactions of the methyl group.

## 6.1 Theory

An understanding of the methyl quantum tunneling experiments first requires an analysis of the effects of symmetry on the methyl group wavefunction.[107-113] If we assume that the equilibrium temperature is low enough that classical internal rotation is frozen then the usual model for a methyl group is an equilateral triangle confined by a hindering barrier to small oscillations about its symmetry axis. Rotation of the methyl group is treated as a sudden transition from one orientation to one of the two other equivalent alignments. This model of the methyl group introduces $C_3$ geometrical symmetry. The $C_3$ symmetry table is reproduced below for reference during this discussion.

| $C_3$ | E | $C_3$ | $C_3^2$ |
|---|---|---|---|
| A | 1 | 1 | 1 |
| $E^a$ | 1 | $\varepsilon$ | $\varepsilon^*$ |
| $E^b$ | 1 | $\varepsilon^*$ | $\varepsilon$ |

$\varepsilon = \exp(2\pi i/3)$

Table 6.1 $C_3$ Character Table

The total wavefunction for the methyl group can be expressed as

$$\Psi_{total} = \Psi_e \Psi_v \Psi_r \Psi_s. \qquad 6.1$$

The four terms on the right side refer to the electronic, vibrational, rotational, and spin parts of the total wavefunction. We do not consider the electronic or vibrational wavefunctions further as they are not involved in the methyl group rotation. But we will assume that they are in a symmetric ground state although this is not a general requirement for the validity of the following argument. This discussion begins by examining the rotational part of the wavefunction first.

The rotational Hamiltonian, $H_r$, consists of a kinetic energy term, corresponding to the free rotation of the methyl group, and a potential energy term, which describes the barrier to free rotation. This can be written as

$$H_r = -\frac{\hbar^2}{2I}\frac{\partial^2}{\partial\phi^2} + V(\phi) \qquad 6.2$$

where I is the moment of inertia and $\phi$ is the angle of rotation from a specific orientation. Because of the $C_3$ symmetry the potential can be described by the following Fourier series

$$V(\phi) = \frac{1}{2}\sum_n V_{3n}(1-\cos(3n\phi)). \qquad 6.3$$

In these experiments the first term in the series dominates and so we ignore all others.

$$V(\phi) \approx \frac{V_3}{2}(1-\cos(3\phi)). \qquad 6.4$$

This is true for the samples we study because they have high barriers and no other local symmetry. For samples with lower barriers, which are usually analyzed by inelastic neutron scattering, this approximation is not good and a second term in the expansion is often needed.

The rotational Hamiltonian is now

$$H_r = -\frac{\hbar^2}{2I}\frac{\partial^2}{\partial\phi^2} + \frac{V_3}{2}(1-\cos(3\phi)). \qquad 6.5$$

For small variations in the angle $\phi$ the potential term can be expanded around the three minima, $\phi_0 = 0, \pm 2\pi/3$, to give[108]

$$V(\phi) \approx \frac{9}{4}(\phi - \phi_0)^2 V_3 = \frac{1}{2} I\, \omega^2(\phi-\phi_0)^2 \qquad 6.6$$

where

$$\omega = \sqrt{\frac{9V_3}{2I}}. \qquad 6.7$$

Thus the rotational Hamiltonian is now;

$$H_r = -\frac{\hbar^2}{2I}\frac{\partial^2}{\partial\phi^2} + \frac{1}{2} I\omega^2(\phi-\phi_0)^2, \qquad 6.8$$

which is the harmonic oscillator Hamiltonian and has eigenvalues

$$E_k = \hbar\omega(k + \frac{1}{2}). \qquad 6.9$$

The triply degenerate ground state wavefunction is calculated to be

$$\Psi_0 = \left(\frac{I\omega}{\hbar\pi}\right)^{1/2} \exp\left(-\frac{I\omega(\phi - \phi_0)^2}{2\hbar}\right) \qquad 6.10$$

with $\phi_0 = 0$ or $\pm 2\pi/3$. Figure 6.1 depicts this situation, which deliberately ignores any tunneling between the potential wells.

Returning to equation 6.5, the eigenstates of this Hamiltonian can be expressed in a basis formed by the three harmonic oscillator ground states. To do this calculation we define the off-diagonal elements to be

$$\int_0^{2\pi} \Psi_0(\phi)\, H_r\, \Psi_0(\phi + \frac{2\pi}{3})\, d\phi = -\frac{\hbar\omega_t}{3} \qquad 6.11$$

where $\omega_t$ is what we call the tunneling splitting.[108] The eigenstates of the rotational Hamiltonian are then found to be

$$\Psi^\lambda = \frac{1}{\sqrt{3}} (\Psi_0(\phi) + \lambda\Psi_0(\phi - \frac{2\pi}{3}) + \lambda^* \Psi_0(\phi + \frac{2\pi}{3})) \qquad 6.12$$

where $\lambda = 1, \varepsilon$ or $\varepsilon^*$ with $\varepsilon = \exp\left(\frac{2\pi i}{3}\right)$. The corresponding eigenvalues are

$$E^1 = E_0 - \frac{2\hbar\omega_t}{3}, \qquad 6.13a$$

$$E^\varepsilon = E^{\varepsilon^*} = E_0 + \frac{\hbar\omega_t}{3}, \qquad 6.13b$$

where $E_0$ is the ground state energy found in the harmonic potential.

We classify the three eigenstates according to the irreducible representations of the $C_3$ symmetry as A, $E^a$, and $E^b$ for $\Psi^0$, $\Psi^{\varepsilon^*}$, and $\Psi^\varepsilon$ respectively. Figure 6.2 displays an energy level diagram of several rotational states. The A and E states are split by what we have defined as the tunneling frequency, $\omega_t$. We can use this parameter to numerically calculate the barrier height to rotation, $V_3$.

Now to the spin part of the wavefunction, because this is, of course, an NMR experiment. First, we define an operator which cyclically permutes the space coordinates,

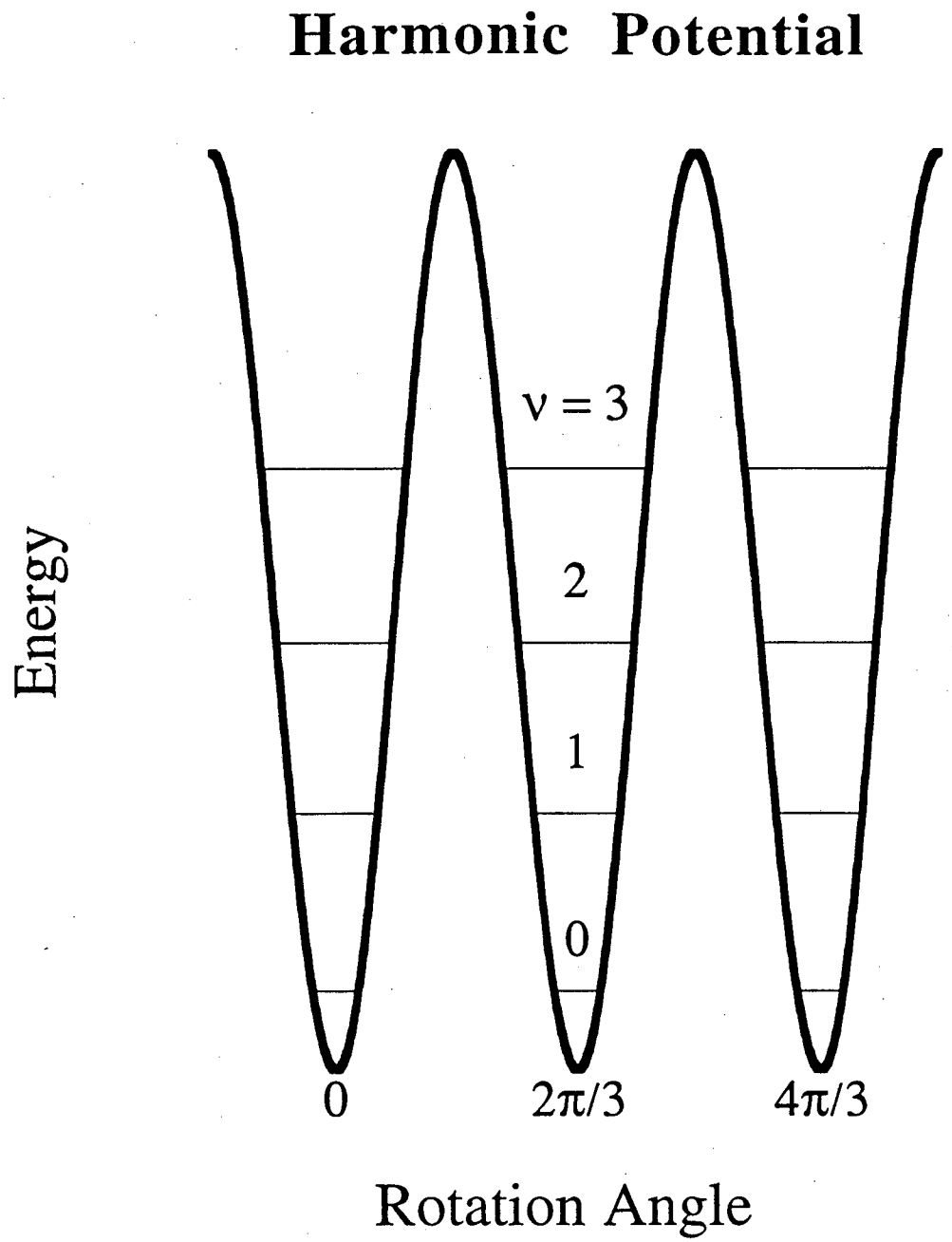


Figure 6.1 Potential energy diagram for a methyl group. The eigenstates are formed from a harmonic approximation (equation 6.8) that does not allow tunneling.

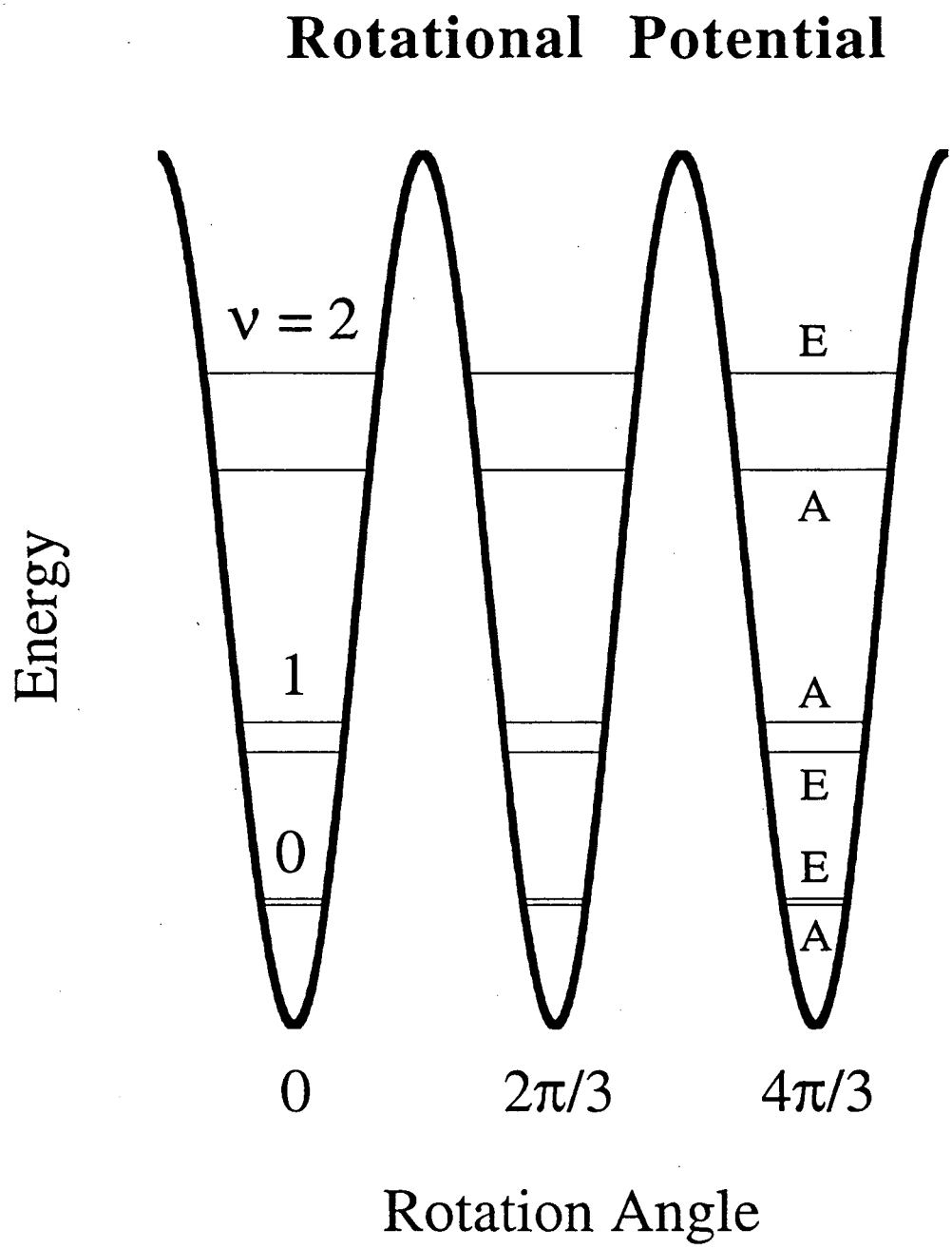


Figure 6.2 Potential energy diagram displaying the energy levels for the full rotational Hamiltonian (equation 6.5). The ground rotational states are split by $\omega_t$, the tunneling frequency.

$$R\Psi_0(\phi) = \Psi_0(\phi + \frac{2\pi}{3}) = R^{-1}\Psi_0(\phi - \frac{2\pi}{3}). \qquad 6.14$$

From this operator a Hamiltonian can be built, $H_t$, that, so long as the system is limited to the ground torsional state, can replace $H_r$ (equation 6.5) since both have the same eigenvalues apart from an unimportant additive constant:

$$H_t = -\frac{\hbar\omega_t}{3}(R + R^{-1}). \qquad 6.15$$

An operator, P, can also be defined which cyclically permutes the spin coordinates. The indistinguishability of the three orientations means that PR is the unit operator so

$$H_t = -\frac{\hbar\omega_t}{3}(P + P^{-1}). \qquad 6.16$$

This Hamiltonian can now be applied to the methyl group spin states which are written in a basis, $|123\rangle$, where 1, 2, and 3 = $\alpha$ or $\beta$ depending on whether the magnetic moment of the particular proton spin is aligned parallel or antiparallel to the orientation of an applied magnetic field. The eigenstates of the combined Zeeman (equation 3.5) and tunneling Hamiltonians are[107]

$$A_{+3/2} = |\alpha\alpha\alpha\rangle, \qquad 6.17a$$

$$A_{+1/2} = \frac{1}{\sqrt{3}}(|\alpha\alpha\beta\rangle + |\alpha\beta\alpha\rangle + |\beta\alpha\alpha\rangle), \qquad 6.17b$$

$$A_{-1/2} = \frac{1}{\sqrt{3}}(|\alpha\beta\beta\rangle + |\beta\alpha\beta\rangle + |\beta\beta\alpha\rangle), \qquad 6.17c$$

$$A_{-3/2} = |\beta\beta\beta\rangle, \qquad 6.17d$$

$$E^a_{+1/2} = \frac{1}{\sqrt{3}}(|\alpha\alpha\beta\rangle + \varepsilon|\alpha\beta\alpha\rangle + \varepsilon^*|\beta\alpha\alpha\rangle), \qquad 6.17e$$

$$E^a_{-1/2} = \frac{1}{\sqrt{3}}(|\alpha\beta\beta\rangle + \varepsilon|\beta\alpha\beta\rangle + \varepsilon^*|\beta\beta\alpha\rangle), \qquad 6.17f$$

$$E^b_{+1/2} = \frac{1}{\sqrt{3}}(|\alpha\alpha\beta\rangle + \varepsilon^*|\alpha\beta\alpha\rangle + \varepsilon|\beta\alpha\alpha\rangle), \qquad 6.17g$$

$$E^b_{-1/2} = \frac{1}{\sqrt{3}}(|\alpha\beta\beta\rangle + \varepsilon^*|\beta\alpha\beta\rangle + \varepsilon|\beta\beta\alpha\rangle). \qquad 6.17h$$

In each case we give the state a short hand name which specifies the irreducible representation of the $C_3$ symmetry group which it transforms as and its magnetic quantum number, $m = m_1 + m_2 + m_3$. For example, $A_{+3/2}$ means an A symmetry state with a total magnetic quantum number of 3/2 (all spins aligned in the direction of the field). The corresponding eigenvalues are

$$E(A_{+3/2}) = -\frac{3}{2}\hbar\omega_z - \frac{2}{3}\hbar\omega_t, \qquad 6.18a$$

$$E(A_{+1/2}) = -\frac{1}{2}\hbar\omega_z - \frac{2}{3}\hbar\omega_t, \qquad 6.18b$$

$$E(A_{-1/2}) = +\frac{1}{2}\hbar\omega_z - \frac{2}{3}\hbar\omega_t, \qquad 6.18c$$

$$E(A_{-3/2}) = +\frac{3}{2}\hbar\omega_z - \frac{2}{3}\hbar\omega_t, \qquad 6.18d$$

$$E(E^a_{+1/2}) = -\frac{1}{2}\hbar\omega_z + \frac{1}{3}\hbar\omega_t, \qquad 6.18e$$

$$E(E^a_{-1/2}) = +\frac{1}{2}\hbar\omega_z + \frac{1}{3}\hbar\omega_t, \qquad 6.18f$$

$$E(E^b_{+1/2}) = -\frac{1}{2}\hbar\omega_z + \frac{1}{3}\hbar\omega_t, \qquad 6.18g$$

$$E(E^b_{-1/2}) = +\frac{1}{2}\hbar\omega_z + \frac{1}{3}\hbar\omega_t. \qquad 6.18h$$

An energy level diagram for the methyl group in a magnetic field is shown in Figure 6.3.

A second variation describing the coupling between the rotational and spin states invokes the Pauli principle instead of the Hamiltonian described in equations 6.14 to 6.16. Beginning with the $|123\rangle$ states, one can symmetrize them to conform with the $C_3$ symmetry group. This leads to the same eigenstates listed above. We recall that the Pauli principle states that a wavefunction must be antisymmetric with regards to the exchange of two indistinguishable fermions.[114] Also, we realize that a $C_3$ rotation of an equilateral triangle of indistinguishable protons corresponds to a double exchange of particles. Thus, the total wavefunction must be symmetric under a $C_3$ rotation. As stated above, the electronic and vibrational wavefunctions are assumed to be in a symmetric ground state because our experiments take place at 4.2 K (i.e. $\frac{\hbar\omega_e}{kT}, \frac{\hbar\omega_v}{kT} >> 4.2$ K). Thus the

## Spin States of the Methyl Group

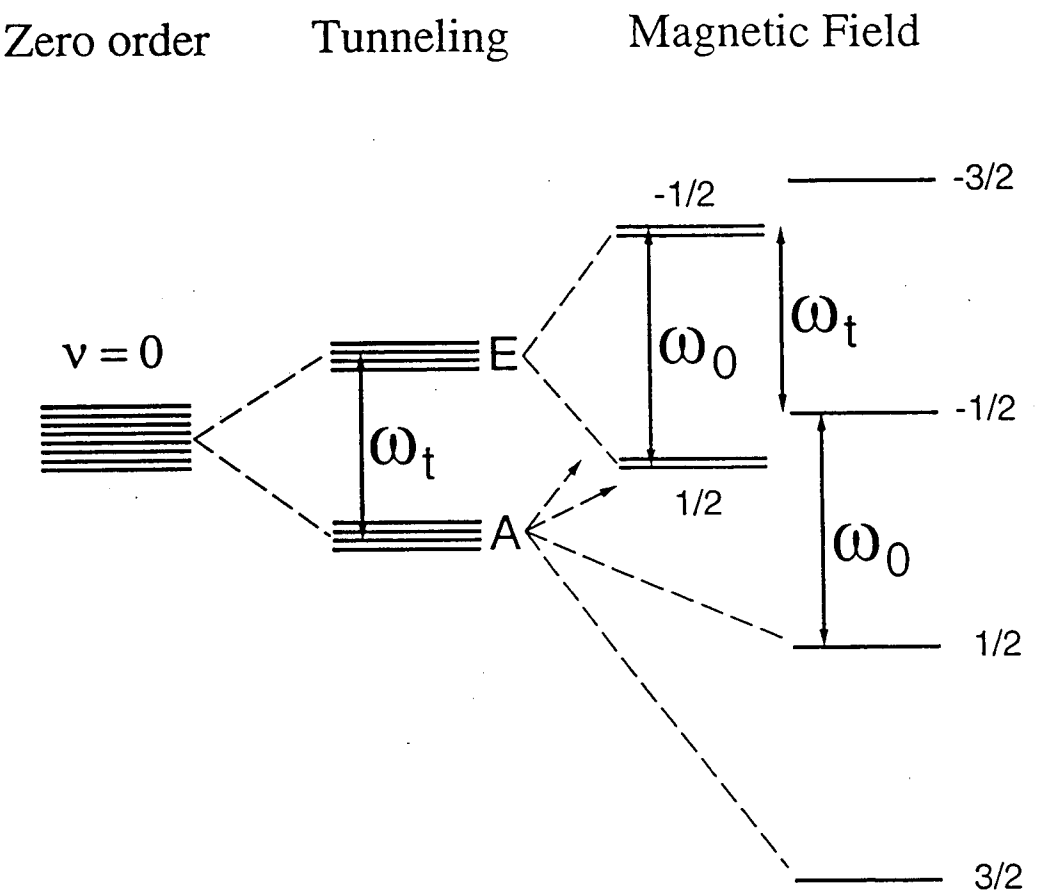


Figure 6.3. Rotational energy levels of a methyl group. (a) Without tunneling. (b) With tunneling: The eight spin states of the $\nu = 0$ rotational state, degenerate in zero order, are split by the tunneling frequency, $\omega_t$, into two manifolds, A and E, consisting of four degenerate states each. (c) When a magnetic field is applied, the A states split according to a spin-3/2 manifold and the E states split according to a doubly degenerate spin-1/2 manifold.

combination of rotational and spin wavefunctions must also be symmetric. Therefore only certain combinations are allowed, namely $A_{rot}A_{spin}$, $E^a{}_{rot}E^b{}_{spin}$, and $E^b{}_{rot}E^a{}_{spin}$. Because the E and A rotational state are split by $\omega_t$, the E and A spin states must be split by the same amount due to this coupling as depicted in Figure 6.3.

Professor S. Clough has recently taken exception to the concept of the indistinguishability of the protons in the methyl group and so he rejects the two previous explanations of the coupling between the spin and rotational systems.[115] He claims that the methyl group can be treated as an anyon and he then uses a Hamiltonian similar to equation 6.15 seemingly without justifying the coupling suggested by this Hamiltonian. Whether this interpretation is true or not is contested but seems necessary to support some of Clough's other contentions such as rotational pressure and rotational friction, both of which could lead to a rotational polarization of the methyl group (i.e. the energies of the $E^a$ and $E^b$ states are inequivalent).[24, 116]

Figure 6.3 displays the steps taken to find the final energy level diagram for the methyl group. Several transitions can now be identified. Those involving transitions between states of the same symmetry: $\omega_z$, $2\omega_z$, and $3\omega_z$; and those between states of different symmetry: $\omega_t$, $\omega_z \pm \omega_t$, and $2\omega_z \pm \omega_t$. An experimental spectrum of hexanol is presented in Figure 6.4 and displays most of these transitions.

In the experiment we must irradiate the system with rf in order to detect the transitions from which the tunneling frequency can be calculated. This, however, is not trivial when one realizes that rf can not excite transitions between states of different symmetry. This is easily understood by looking at the transition probability;

$$\int \Psi_0{}^* \, H \, \Psi_1 \, d\tau, \qquad 6.19$$

where $\Psi_0$ is the original state, $\Psi_1$ is the new state, and H is the Hamiltonian used to induce the transition. This integral vanishes unless the direct product $\Psi_0{}^* \otimes H \otimes \Psi_1$ has a component with A type symmetry.[117] For rf excitation the Hamiltonian given in equations

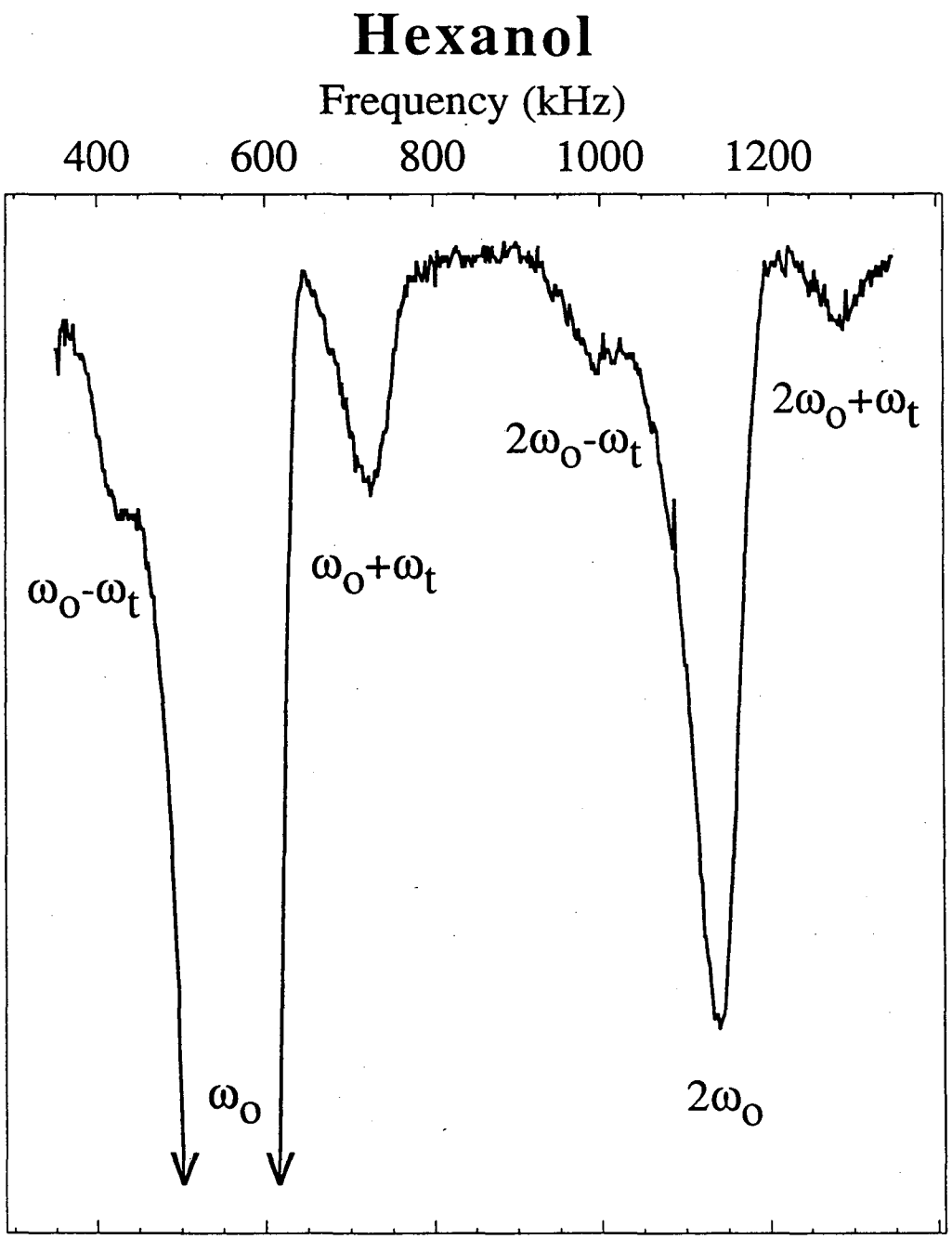


Figure 6.4. Methyl tunneling spectrum of hexanol.

3.9 and 3.10 have only A type symmetry. The matrix element is, therefore, a direct product of terms with A, A, and E type symmetry respectively. This direct product is completely of E type symmetry and therefore the transition probability is zero. Thus a transition between states of A and E states is forbidden. However, in low field the dipolar interaction helps overcome this problem.

The dipolar Hamiltonian promotes mixing between all states in the energy level system.[109] The A and E states are specifically mixed together by the nonsecular parts of the dipolar interaction (terms "C"-"F" of the dipolar Hamiltonian, equations 3.8c-f). Because it is the nonsecular terms that cause the mixing, these experiments can not be performed at high field, where these parts of the dipolar Hamiltonian are very small compared to the Zeeman term and rotating off resonance so as to have little effect on the eigenstates. The SQUID provides the ideal environment for these experiments because it easily satisfies both requirements for success: low temperature (where classical rotation is frozen) and low field (where the dipolar coupling makes the tunneling transitions slightly allowed).

Clough and coworkers have proposed an additional mechanism for excitation to account for the intensities of the tunneling lines in their field cycling experiments.[118] They find that the transitions corresponding to $\Delta m = \pm 1$ and $\Delta m = \pm 2$ have comparable intensities and are larger than the $\Delta m = \pm 3$ transitions. If rf irradiation provided the only means for causing transitions, one should find that the $\Delta m = \pm 1$ transitions would be much larger then the others and that the $\Delta m = \pm 2$ and $\Delta m = \pm 3$ transitions should be comparable.[119] To account for this anomaly in their experiments they propose what they call dipolar driven NMR. They suggest that the rf and magnetic fields can be added to give a time dependent field. In a reference frame moving with this composite field, part of the dipolar Hamiltonian becomes time dependent. This now produces a spectrum with transitions defined by the selection rules of the dipolar Hamiltonian. That leads to a spectrum with the $\Delta m = \pm 1$ and $\Delta m = \pm 2$ transitions of comparable magnitude.

Dipolar driven NMR appears to also explain our spectra. We do not see any transitions corresponding to $\Delta m = \pm 3$, but those with $\Delta m = \pm 2$ are approximately 1/2 to 1/4 the intensity of the $\Delta m = \pm 1$ transitions. Thus, it would seem that the dipolar interaction takes a more active role in the experiment rather than just mixing states of different symmetry.

### 6.1.1 Barrier Heights

The objective of these experiments is to obtain the tunneling frequency and from that calculate the barrier to rotation, $V_3$.[120] This barrier comes from both intramolecular and intermolecular sources:

$$V_{barrier} = V_{intra} + V_{inter}. \qquad 6.20$$

Some generalizations can be made about the barrier height and its intra- and intermolecular elements.

Usually, the intramolecular part dominates and that in turn is dominated by the sections of the molecule closest to the methyl group. One can estimate the size of the barrier by looking at the hybridization of the carbon to which the methyl group is attached. If that carbon atom is sp or $sp^2$ hybridized, such as in acetone or toluene, the barrier is approximately 10-30 meV with tunneling frequencies in the MHz-GHz range.[106] If, however, the carbon atom is $sp^3$ hybridized, such as in the alkanes or the alcohols, the barrier is much larger due to the increased steric hindrance around the methyl group.[25, 26] These barriers tend to be in the 130-150 meV region with tunneling frequencies less than 1 MHz. Figure 6.5 graphs several representative samples and displays this overall trend. This last range is the ideal environment for the SQUID spectrometer and will be the focus for the rest of our discussion.

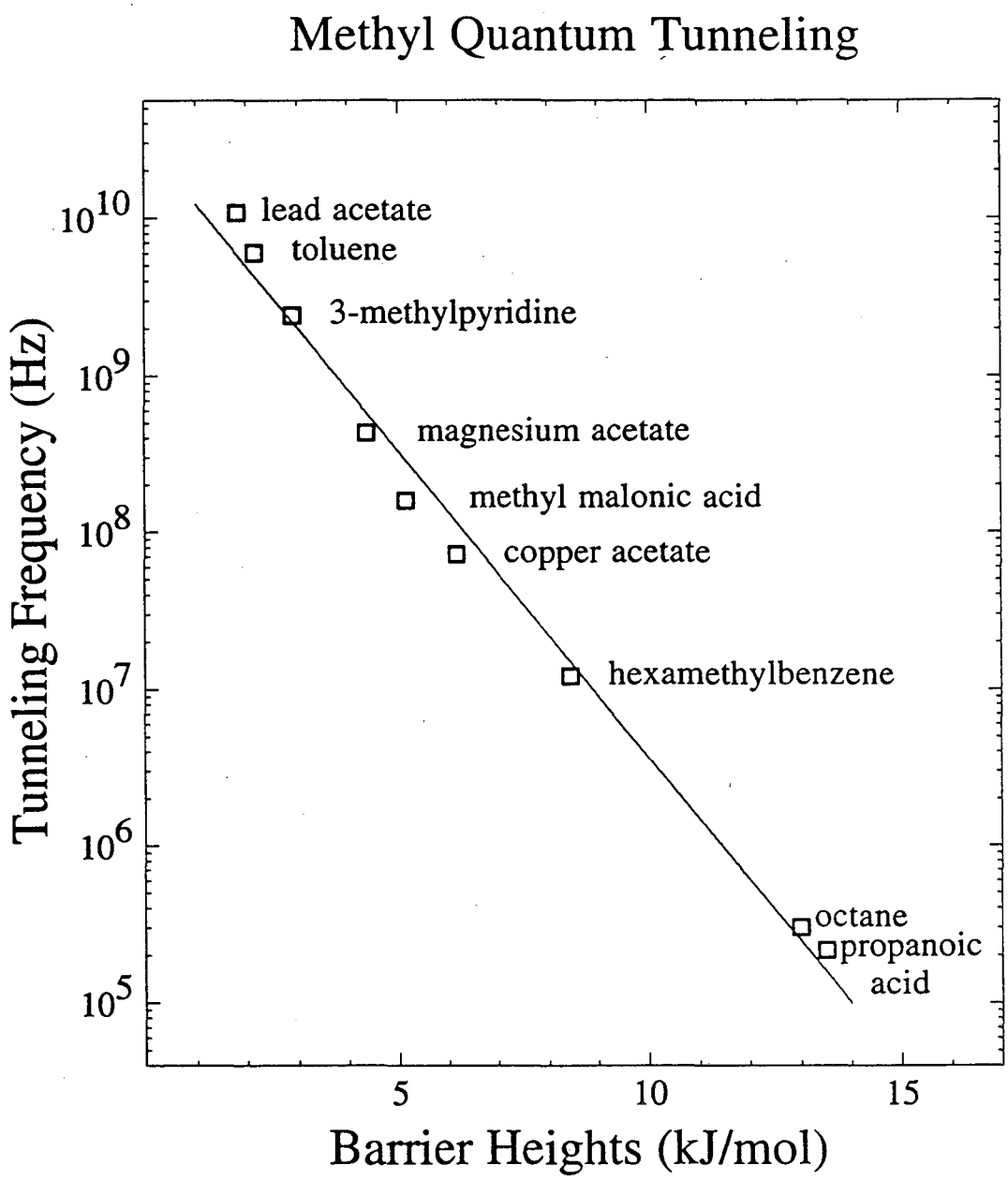


Figure 6.5. Plot of the tunneling frequency vs. barrier height for several representative samples.[121] Note the wide range of tunneling frequencies. Those with high values, usually methyl groups attached to sp or $sp^2$ hybridized carbon atoms, are measured by inelastic neutron scattering. The materials with tunneling frequencies less than 1 MHz, typically those attached to $sp^3$ hybridized carbons, can be analyzed by field cycling NMR or the SQUID spectrometer. (1 kJ/mol = 10.36 meV)

Although the intramolecular part of the barrier dominates, information can be obtained about the intermolecular interactions. One way of doing this is by analyzing the same compound but different crystal structure. However, the difference in the barrier heights is then not strictly due to intermolecular changes but also reflects the influence of crystal structure on the molecular conformation near the methyl group.

Another way to gain information about intermolecular interactions is by the study of a series of related molecules with the same type of crystal structure. The idea is to keep the intramolecular contribution constant while studying changes in the tunneling barrier versus differences in the crystalline parameters. For small changes in the barrier height due to intermolecular interactions such as these, the tunneling frequency becomes approximately an exponential function of $V_3$.[122]

The high barrier samples in these experiments have a dominating intramolecular potential. However, because the important contributions to the intramolecular potential come only from those parts of the molecule that are very close to the methyl group, lengthening the chain will not be important as the methyl group feels essentially only methylene units. So the intramolecular potential is kept relatively constant for a series of compounds where the only structural modification is in the length of the chain. The difference in the barrier between molecules due to changes in the intermolecular potential should become apparent so long as they have the same basic crystal structure.

## 6.1.2 Previous Methods

The earliest measurements of the tunneling frequency were from microwave spectra of small molecules in the gas phase.[123, 124] This method is of limited usefulness because the rotational spectrum becomes excessively complicated and unresolvable for larger molecules. However, tunneling measurements on molecules such as methanol, ethanol, and acetone were carried out.

More recently, investigators have primarily used techniques such as inelastic neutron scattering (INS), a $T_1$ temperature minimum correlation, and field cycling experiments. For tunneling frequencies in the hundreds of MHz to GHz range, INS provides the best method for measurement. Also, Clough and coworkers were also able to correlate the $T_1$ temperature minimum and the tunneling frequency to give a rough estimate of barrier to rotation.[125] Recently, he showed that this correlation is true for the entire range of tunneling frequencies.[126]

However, the method I wish to focus on is the field cycling experiment, used primarily by Clough et. al., because it is in direct competition with the SQUID spectrometer. These experiments are very similar to those described in Chapter 5 for $^{14}N$ NQR detection. The method can be divided into three parts: 1) preparation, 2) irradiation, and 3) detection. In the preparation phase the sample is left in a high field magnet long enough for the protons to achieve an equilibrium polarization. The sample is then placed into zero or low field either by moving the sample or decreasing the field of the magnet. In this low or zero field, the sample is irradiated at a specific rf frequency. If this frequency corresponds to a resonance then the proton spin bath absorbs energy, otherwise nothing happens. Upon returning to high field the proton magnetization is measured. If the irradiation frequency corresponded to a resonance then that final magnetization will be smaller. Each cycle gives a single point for the final low field spectrum. This process is repeated, each time stepping either the irradiation frequency or the low field magnet strength by a specific amount until the entire spectrum is obtained. This can take a long period of time, especially when signal averaging is needed.

The SQUID spectrometer has several advantages over field cycling. First, as alluded to above, the SQUID method can have a great savings in experimental time. A spectrum can be obtained in one scan by the SQUID spectrometer (although usually at least one scan in each sweep direction for each resonance is preferred) compared to the many cycles needed for field cycling experiments. Also, the SQUID spectrometer is specifically

built to operate at low temperatures, which is a requirement for observation of the tunneling phenomenon. A low temperature field cycling apparatus requires either the shuttling of the sample at 4.2 K or changing the field strength of the NMR magnet with the sample in a cryostat. Neither of which is particularly simple to construct and use. Thus the SQUID spectrometer may ultimately be the method of choice for low frequency methyl quantum tunneling measurements.

## 6.2 Experimental Results

In this section I present the results that we have obtained from the SQUID spectrometer. We studied a series of straight chained carboxylic acids with 3-15 carbon atoms.[22, 127] The results are given in Table 6.2. The tunneling frequency for propanoic acid was previously measured by field cycling to be 210 kHz[24] which agrees with that obtained in these experiments. I have also provided in this table a key of the crystal structures of the acids as the tunneling frequency is a function of this parameter. The symbols for these structures are based on the literature.[128]

A tunneling frequency was not found for butanoic acid. It could be that the tunneling frequency was to small to detect due to the overlapping of the tunneling resonance with the much stronger Larmor line or perhaps butanoic acid formed a glass upon cooling to low temperature which would produce a distribution of sites over which the signal intensity would be spread. It is interesting to note that of all the carboxylic acids studied, butanoic acid is the only one to have a low temperature phase transition as demonstrated by heat capacity measurements.[129-131] Quite possibly something about this phase transition prevents us from finding the tunneling resonances.

We have also obtained tunneling splittings for other molecules, most notably simple organic molecules with six carbon atoms, in order to compare their barriers to rotation. These are also shown in Table 6.2. All of these samples have barriers of the same order of

| Name (No. of Carbons) | Crystal Phase | Tunneling Frequency (kHz) | Barrier Height (meV) |
|---|---|---|---|
| Propanoic Acid (3) | m | 215 | 140.0 |
| Butanoic Acid (4) | | See text | |
| Pentanoic Acid (5) | m | 250 | 137.7 |
| Hexanoic Acid (6) | m* | 168 | 143.8 |
| Heptanoic Acid (7) | m* | 193 | 141.6 |
| Octanoic Acid (8) | m* | 170 | 143.6 |
| Nonanoic Acid (9) | m* | 156 | 144.9 |
| Decanoic Acid (10) | A | 189 | 141.9 |
| Undecanoic Acid (11) | C' | 140 | 146.8 |
| " | A' | 193 | 141.6 |
| Dodecanoic Acid (12) | C | 177 | 142.9 |
| " | A | 168 | 143.8 |
| Tridecanoic Acid (13) | A' | 191 | 141.8 |
| Tetradecanoic Acid (14) | A | 162 | 144.3 |
| Pentadecanoic Acid (15) | A' | 190 | 141.9 |
| Hexadecanoic Acid (16) | B | 179 | 142.8 |
| 1-Bromohexane | | 246 | 138.1 |
| 1-Bromooctane | | 207 | 140.7 |
| 1-Bromodecane | | 207 | 140.7 |
| Hexanol | | 155 | 145.0 |

Table 6.2 Methyl group tunneling frequencies ( ± 4 kHz) obtained from SQUID-NMR measurements. The crystal phases are taken from refs. 128, 132-134 . A and A' are triclinic crystals and B, C, C' and m are monoclinic structures. m* denotes an assumed monoclinic phase inferred from the known crystal structures of the other acids.

magnitude, however trends due to the functionality at the end of a carbon chain can't be determined because the crystal structures of these molecules are not similar.

Figure 6.6 shows a graph of the tunneling frequencies of the carboxylic acids versus the number of carbon atoms in the molecule and includes lines connecting acids of similar crystal structure. This plot indicates some general trends in the series. First, the acids with odd and even numbers of carbons have different but related crystal structures[128] and that the trends in tunneling frequency confirm this information. Clough and coworkers found a similar odd-even effect in their study of a series of alkanes.[25] The next interesting feature is the large variation in tunneling frequency for the smaller acids and relative constancy for the larger acids. This makes sense as we expect the shorter acids to show bigger changes between their crystal structures and those of slightly longer acids. It is also of interest that the tunneling frequencies of the same molecule in unlike crystalline forms are significantly different, especially in the case of undecanoic acid.

Another interesting feature is the overall maximum tunneling frequency of pentanoic acid. This is unusual for we would expect a maximum at either end of the series. However, when one looks at other properties of this series such as melting point temperatures and enthalpies of fusion one finds that pentanoic acid is also an extreme.[135] This leads us to consider possible correlations between the thermodynamic properties of the carboxylic acids and their tunneling frequencies.

## 6.3 Correlations with Thermodynamic Properties

As mentioned above the anomalous behavior of pentanoic acid led us to study other features of the carboxylic acids. We were able to make a correlation between the tunneling frequency and the enthalpy of fusion[129-131, 136] for carboxylic acids of the same crystal structure. The plots are found in Figure 6.7 with the correlation:

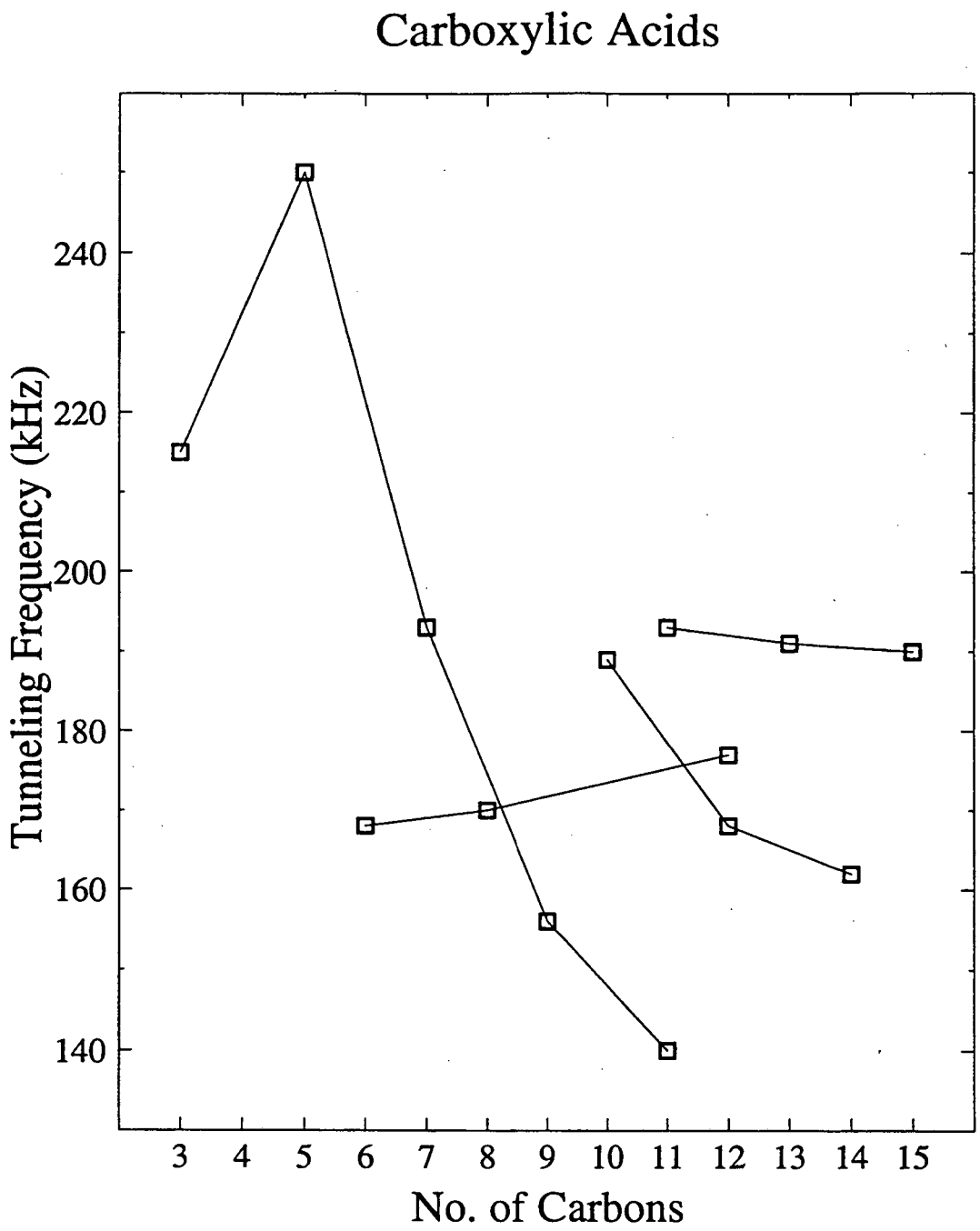


Figure 6.6. Plot of the tunneling frequency vs. number of carbons for the carboxylic acids. Those materials with the same type of crystal structure are connected by lines.

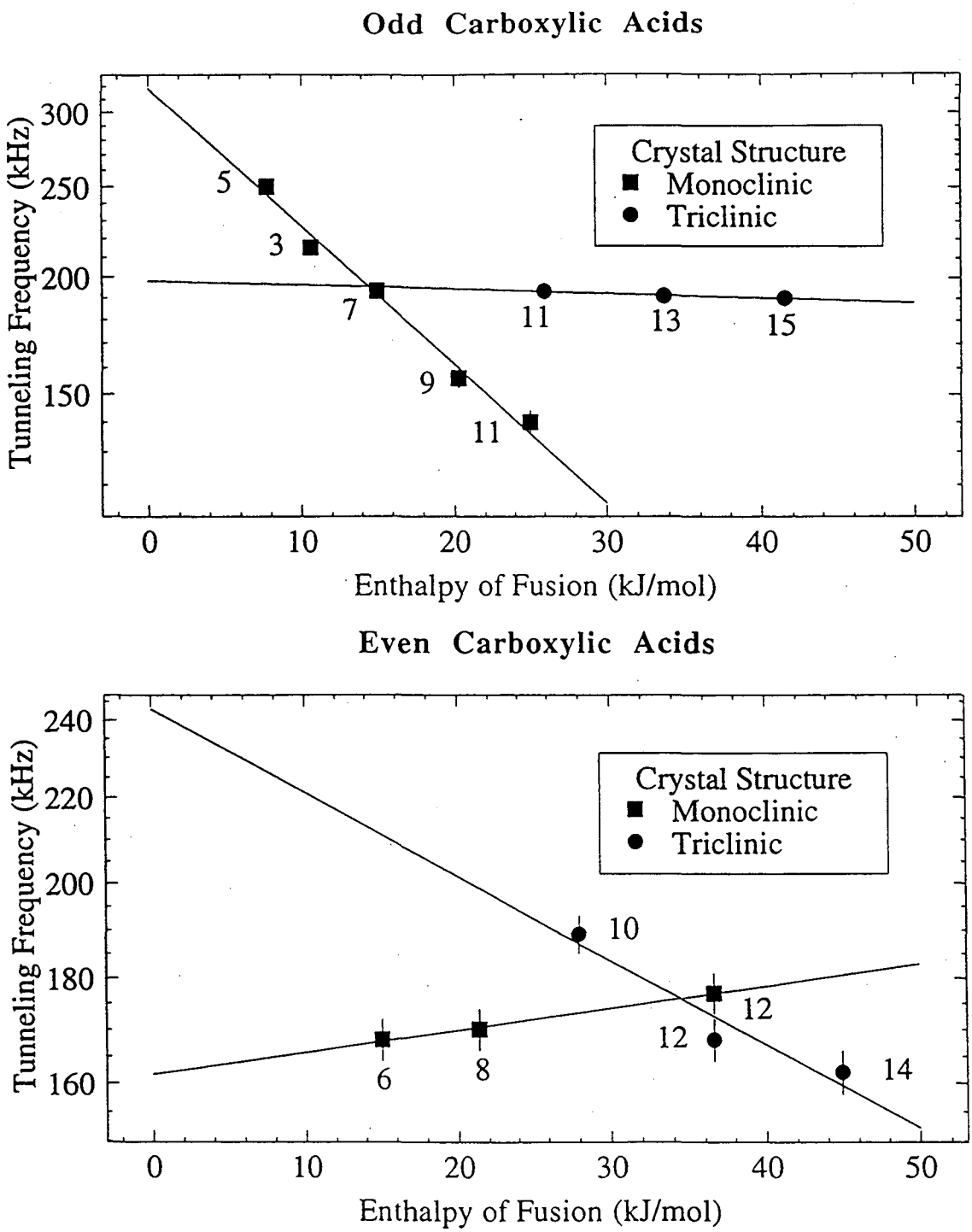


Figure 6.7. Experimentally determined tunneling frequencies as a function of the enthalpies of fusion for a series of carboxylic acids. For pentanoic acid there is considerable disagreement about the enthalpy of fusion.

$$\omega_t = a \exp(-\Delta H_{fus}/b); \qquad 6.21$$

where a and b are fitting parameters. This also implies that

$$V_3 \propto \Delta H_{fus}. \qquad 6.22$$

A fundamental question is raised by this correlation about how a macroscopic property, such as the enthalpy of fusion, can be related to a microscopic property, the barrier height to rotation. Perhaps even more puzzling is why would a property, like the enthalpy of fusion that depends upon the interactions of the entire molecule, be correlated to the tunneling frequency, which is concerned only with the region around the methyl group. A close look at the origin of the enthalpy of fusion and barrier height to rotation in relation to the crystal structure of these materials may provide some answers.

Looking at the crystal structures of the carboxylic acids (for example Figure 6.8), it becomes apparent that the methyl group of one acid is between the four carboxylic acid dimer groups above and below.[128, 132-134] These groups tend to get closer together as the acids get longer and in general correlate to the tunneling frequency although a quantitative measure of this can not be obtained due to the lack of crystal structure data. As the acid groups get closer together, the methyl group is squeezed between them causing a higher barrier to rotation and thus a smaller tunneling frequency.

Another indication of the influence of the acid groups is the tunneling barrier for long chain molecules. For long chained alkanes and ketones this tunneling frequency is on the order of 300 kHz.[25, 26] However, for the carboxylic acids this frequency is around 180 kHz. This lower frequency and thus higher barrier is probably due to the stronger interactions between the highly polar carboxylic acid groups which squeeze the methyl group.

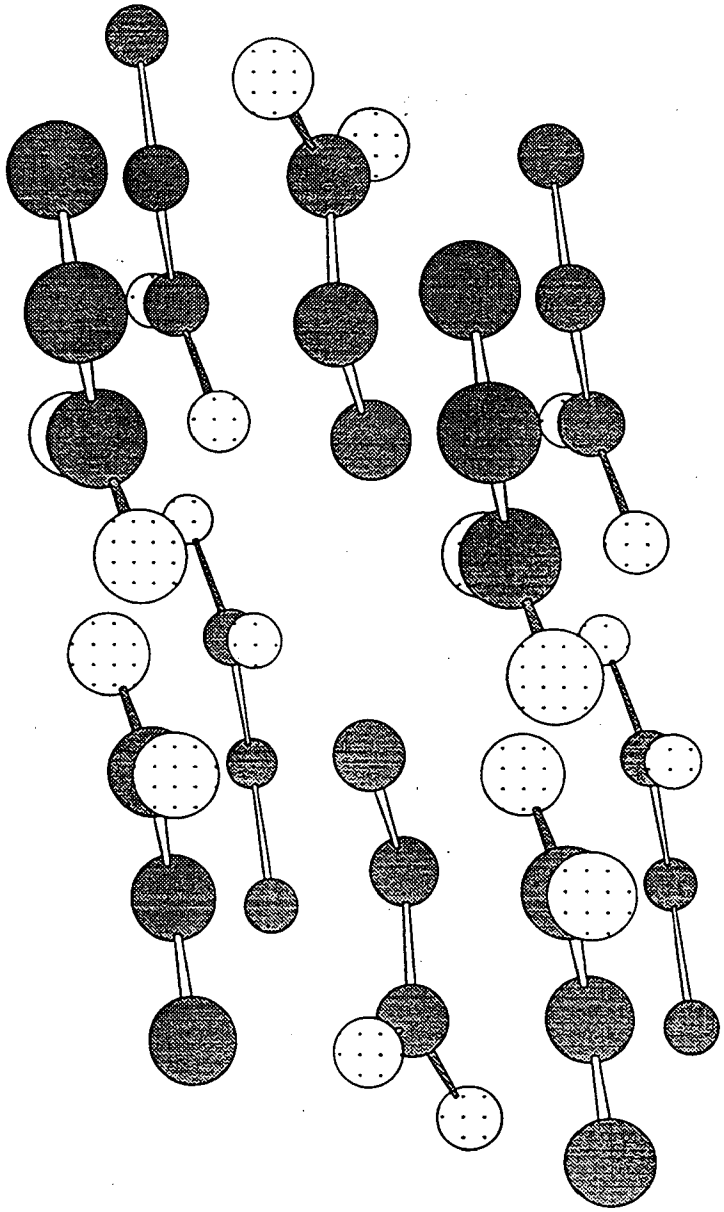

Figure 6.8. Sample crystal structure of propanoic acid.[133] Carbon atoms are shaded, oxygens are patterned. The methyl group is placed between four carboxylic acid dimer groups.

It is well known that the carboxylic acids have a much higher enthalpy of fusion than equally heavy alkanes. This, of course, is because of the hydrogen bonding and electrostatic interactions of the highly polarizable carboxylic acid groups. The strength of these interactions increases as the acid groups get closer together. Thus giving a corresponding increase in the enthalpy of fusion as the acids gets longer and the carboxylic groups get closer together which is almost entirely due to the acid functionalities.

And thus we have our correlation. Both the enthalpy of fusion and the changes in the barrier to rotation are influenced by the surrounding carboxylic acid groups. This kind of experiment indicates that the study of methyl quantum tunneling can give us some insight into what is happening around a specific part of a molecule, namely the methyl group.

# Bibliography


1. T. P. Das and E. L. Hahn, *Solid State Physics*, Supplement 1, edited by F. Seitz and D. Turnbull, (Academic Press, New York, 1958).

2. M. H. Cohen and F. Reif, *Solid State Physics*, Vol. 5, edited by F. Seitz and D. Turnbull, (Academic Press, New York, 1957).

3. R. V. Pound, *Phys. Rev.* **79**, 685 (1950).

4. G. E. Pake, *J. Chem. Phys.* **16**, 327 (1948).

5. N. Bloembergen and J. A. Rowland, *Acta Metallurg.* **1**, 731 (1953).

6. C. H. Townes and B. P. Dailey, *J. Chem. Phys.* **20**, 35 (1952).

7. A. Samosan, E. Kundla and E. Lippmaa, *J. Magn. Reson.* **49**, 350 (1982).

8. K. T. Mueller, B. Q. Sun, G. C. Chingas, J. W. Zwanziger, T. Terao and A. Pines, *J. Magn. Reson.* **86**, 470 (1990).

9. Y. Wu, B. Q. Sun, A. Pines, A. Samosan and E. Lippmaa, *J. Magn. Reson.* **89**, 297 (1990).

10. D. I. Hoult and R. E. Richards, *J. Magn. Reson.* **24**, 71 (1976).

11. P. Lorrain and D. R. Corson, *Electromagnetic Fields and Waves*, 2nd edition, (W. H. Freeman and Co., San Francisco, 1962).

12. D. B. Zax, A. Bielecki, K. W. Zilm, A. Pines and D. P. Weitekamp, *J. Chem. Phys.* **83**, 4877 (1985).

13. D. T. Edmonds, *Int. Rev. Phys. Chem.* **2**, 103 (1982).

14. J. Clarke, *Phys. Today* **39**, 36 (1986).

15. J. Clarke, in *Superconductor Applications: SQUIDs and Machines*, edited by B. B. Schwartz and S. Foner, (Plenum Press, New York, 1977).

16. R. L. Fagaly, *Sci. Prog., Oxf.* **71**, 181 (1987).

17. C. Connor, *Low Frequency Magnetic Resonance with a dc SQUID*, Ph.D. Thesis, University of California at Berkeley, 1989.

18. J. W. Chang, *Low Frequency Nuclear Quadrupole Resonance with a dc SQUID*, Ph.D. Thesis, University of California at Berkeley, 1991.

19. J. Knuutila, A. Ahonen and C. Tesche, *J. Low Temp. Phys.* **68**, 269 (1987).

20. J. Chang, C. Connor, E. L. Hahn, H. Huber and A. Pines, *J. Magn. Reson.* **82**, 387 (1989).

21. C. Connor, J. Chang and A. Pines, *Rev. Sci. Instrum.* **61**, 1059 (1990).

22. C. Connor, J. Chang and A. Pines, *J. Chem. Phys.* **93**, 7639 (1990).

23. *Quantum Aspects of Molecular Motions in Solids*, edited by A. Heidemann, A. Magerl, M. Prager, D. Richter and T. Springer, (Springer Verlag, Berlin, 1987).

24. S. Clough, G. J. Baker, K. J. Abed and A. J. Horsewill, *Phys. Rev. Lett.* **60**, 136 (1988).

25. K. J. Abed and S. Clough, *Chem. Phys. Lett.* **142**, 209 (1987).

26. K. J. Abed, S. Clough, A. J. Horsewill and M. A. Mohammad, *Chem. Phys. Lett.* **147**, 624 (1988).

27. J. Clarke, *Am. Jour. of Phys.* **38**, 1071 (1970).

28. J. Clarke, *Proc. IEEE* **61**, 8 (1973).

29. F. Wellstood, C. Heiden and J. Clarke, *Rev. Sci. Instrum.* **55**, 952 (1984).

30. J. Clarke, W. M. Goubau and M. B. Ketchen, *J. Low Temp. Phys.* **25**, 99 (1976).

31. C. Kittel, *Introduction to Solid State Physics*, (John Wiley and Sons, New York, 1986).

32. A. Th. A. M. De Waele and R. De Bruyn Ouboter, *Physica* **41**, 225 (1969).

33. D. E. McCumber, *J. Appl. Phys.* **39**, 2503 (1968).

34. R. P. Feynman, R. B. Leighton and M. Sands, *The Feynman Lectures on Physics*, Vol. 3 (Addison-Wesley Publishing, Reading, Mass., 1965).

35. R. C. Jaklevic, J. Lambe, J. E. Mercereau and A. H. Silver, *Phys. Rev. A* **140**, 1628 (1965).

36. T. Jach, *Appl. Phys. Lett.* **28**, 49 (1976).

37. H. K. Onnes, *Comm. Phys. Lab.*, Univ. Leiden, Nos. 119, 120, 122 (1911).

38. J. Bardeen, L. N. Cooper and J. R. Schriefer, *Phys. Rev.* **108**, 1175 (1957).

39. N. W. Ashcroft and N. D. Mermin, *Solid State Physics*, (Saunders College, Philadelphia, 1976).

40. W. Meisner and R. Ochsenfeld, *Naturwiss.* **21**, 787 (1933).

41. H. London and F. London, *Proc. Roy. Soc. (London)* **A149**, 71 (1935).

42. H. London and F. London, *Physica* **2**, 341 (1935).

43. F. London, in *Superfluids*, Vol. 1, (John Wiley and Sons, New York, 1950).

44. B. D. Josephson, *Phys. Lett.* **1**, 251 (1962).

45. C. D. Motchenbacher and F. C. Fitchen, *Low-Noise Electronic Design*, (John Wiley and Sons, New York, 1973).

46. P. Horowitz and W. Hill, *The Art of Electronics*, (Cambridge University Press, Cambridge, Mass., 1980).

47. J. Clarke, *IEEE Trans. Magn.* **MAG-19**, 288 (1983).

48. M. Tinkham, *Introduction to Superconductivity*, (McGraw-Hill, New York, 1975).

49. D. P. Osterman and S. J. Williamson, *Rev. Sci. Instrum.* **54**, 1380 (1983).

50. E. P. Day, *Phys. Rev. Lett.* **29**, 540 (1972).

51. R. V. Chamberlain, L. A. Moberly and O. G. Symko, *J. Low Temp. Phys.* **35**, 337 (1979).

52. R. A. Webb, *Rev. Sci. Instrum.* **48**, 1585 (1977).

53. T. Jach, *Observation of Nuclear Quadrupole Resonance with Superconducting Magnetometers*, Ph.D. thesis, Stanford University, 1975.

54. C. H. Townes and B. P. Dailey, *J. Chem. Phys.* **17**, 782 (1949).

55. P. J. Bray, *J. Non-Cryst. Solids* **73**, 19 (1985).

56. P. J. Bray, *J. Non-Cryst. Solids* **75**, 29 (1985).

57. D. T. Edmonds, *Phys. Rep.* **29**, 233 (1977).

58. C. P. Slichter, *Principles of Magnetic Resonance*, 3rd edition, (Springer Verlag, New York, 1989).

59. N. Bloembergen, S. Shapiro, P. S. Pershan and J. O. Artman, *Phys. Rev.* **114**, 445 (1959).

60. D. Suter and R. R. Ernst, *Phys. Rev. B* **32**, 5608 (1985).

61. A. Abragam and K. Kambe, *Phys. Rev.* **91**, 894 (1953).

62. C. Dean, *Phys. Rev.* **96**, 1053 (1954).

63. M. Bloom, E. L. Hahn and B. Herzog, *Phys. Rev.* **97**, 1699 (1955).

64. M. J. Weber and E. L. Hahn, *Phys. Rev.* **120**, 365 (1960).

65. M. Goldman, *Spin Temperature and Nuclear Magnetic Resonance in Solids*, (Clarendon Press, Oxford, 1970).

66. S. J. Gravina and P. J. Bray, *J. Magn. Reson.* **89**, 515 (1990).

67. P. J. Bray, S. J. Gravina, D. H. Hintenlang and R. V. Mulkern, *Magn. Reson. Rev.* **13**, 263 (1988).

68. D. Lee, S. J. Gravina and P. J. Bray, *Z. Naturforsch.* **45a**, 268 (1990).

69. S. J. Gravina, P. J. Bray and G. L. Petersen, *J. Non-Cryst. Solids* **123**, 165 (1990).

70. P. J. Bray, D. Lee, D. G. Mao, G. L. Petersen, S. A. Feller, D. L. Bain, D. A. Feil, P. Pandikuthira and S. Nijhawan, *Z. Naturforsch.* **47a**, 30 (1992).

71. Y. Morino and M. Toyama, *J. Chem. Phys.* **35**, 1289 (1961).

72. Y. H. Yun and P. J. Bray, *J. Non-Cryst. Solids* **27**, 363 (1978).

73. Y. H. Yun, S. A. Feller and P. J. Bray, *J. Non-Cryst. Solids* **33**, 273 (1979).

74. W. J. Dell, P. J. Bray and S. Z. Xiao, *J. Non-Cryst. Solids* **58**, 1 (1983).

75. P. J. Bray, S. J. Gravina, P. E. Stallworth, S. P. Szu and J. Zhong, *Exp. Tech. Phys.* **36**, 397 (1988).

76. R. S. Pease, *Acta Crystallogr.* **5**, 356 (1952).

77. C. J. Whidden, C. D. Williams and R. F. Tipsword, *J. Chem. Phys.* **50**, 507 (1969).

78. H. S. Gutowsky and G. A. Williams, *Phys. Rev.* **105**, 464 (1957).

79. J. Itoh and R. Kusaka, *J. Phys. Soc. Japan* **9**, 434 (1954).

80. N. Ishizawa, T. Miyata, I. Minato, F. Marumo and S. Iwai, *Acta Crystallogr.* **B36**, 228 (1980).

81. D. Lee and P. J. Bray, *J. Magn. Reson.* **94**, 51 (1991).

82. T. Tagai, H. Reid, W. Joswig and M. Korekawa, *Z. Kristallogr.* **160**, 159 (1982).

83. K. T. Mueller, G. C. Chingas and A. Pines, *Rev. Sci. Instrum.* **62**, 1445 (1991).

84. J. F. Baugher, P. C. Taylor, T. Oja and P. J. Bray, *J. Chem. Phys.* **50**, 4914 (1969).

85. D. Mao, P. J. Bray and G. L. Petersen, *J. Am. Chem. Soc.* **113**, 6812 (1991).

86. A. Nolle, *Z. Physik A* **282**, 21 (1977).

87. G. J. Palenik, *Inorg. Chem.* **6**, 503 (1967).

88. E. G. Boonstra, *Acta Crystallogr.* **B24**, 1053 (1968).

89. G. W. Leppelmeier and E. L. Hahn, *Phys. Rev.* **141**, 724 (1966).

90. G. M. Muha, *J. Chem. Phys.* **73**, 4139 (1980).

91. G. M. Muha, *J. Magn. Reson.* **49**, 431 (1982).

92. J. R. Brookeman, M. M. McEnnan and T. A. Scott, *Phys. Rev. B* **4**, 3661 (1971).

93. T. A. Scott, *J. Chem. Phys.* **36**, 1459 (1962).

94. D. Stephenson and J. A. S. Smith, *Proc. R. Soc. Lond. A* **416**, 146 (1988).

95. R. E. Slusher and E. L. Hahn, *Phys. Rev.* **166**, 332 (1968).

96. R. Blinc, in *Advances in Nuclear Quadrupole Resonance* , edited by J. A. Smith, Vol. 2 (Heyden & Son Ltd., London, 1975).

97. D. T. Edmonds and J. P. G. Mailer, *J. Magn. Reson.* **26**, 93 (1977).

98. M. J. Hunt, *J. Magn. Reson.* **15**, 113 (1974).

99. D. T. Edmonds and P. A. Speight, *Phys. Lett.* **34A**, 325 (1971).

100. D. T. Edmonds and P. A. Speight, *J. Magn. Reson.* **6**, 265 (1972).

101. D. T. Edmonds and C. P. Summers, *J. Magn. Reson.* **12**, 134 (1973).

102. D. T. Edmonds, M. J. Hunt and A. L. MacKay, *J. Magn. Reson.* **9**, 66 (1973).

103. C. T. O'Konski and K. Torizuka, *J. Chem. Phys.* **51**, 461 (1969).

104. R. Blinc, M. Mali, R. Osredkar, A. Prelesnik, J. Selinger, I. Zupancic and L. Ehrenberg, *J. Chem. Phys.* **57**, 5087 (1972).

105. P. Jönsson and Å. Kvick, *Acta Crystallogr.* **B28**, 1827 (1972).

106. *Single Particle Rotations in Molecular Crystals* , edited by W. Press, Springer Tracts in Modern Physics, Vol. 92 (Springer Verlag, Berlin, 1981).

107. J. H. Freed, *J. Chem. Phys.* **43**, 1710 (1965).

108. S. Clough, in *NMR-Basic Principles and Progress*, edited by M. M. Pintar, Vol. 13 (Springer Verlag, Berlin, 1976).

109. A. E. Zweers, *Methyl Group Rotation and Nuclear Relaxation at Low Temperatures*, Ph.D. thesis, Leiden, 1976.

110. S. Clough, *J. Phys. C* **4**, 2180 (1971).

111. S. Emid, R. A. Wind and S. Clough, *Phys. Rev. Lett.* **33**, 769 (1974).

112. S. Emid, R. J. Baarda, J. Smidt and R. A. Wind, *Physica* **93B**, 327 (1978).

113. B. Gabrys, *Mol. Phys.* **51**, 601 (1984).

114. H. Clark, *A First Course in Quantum Mechanics*, (Van Nostrand Reinhold, Berkshire, 1982).

115. S. Clough, A. J. Horsewill, M. R. Johnson and I. B. I. Tomsah, *preprint* (1993).

116. S. Clough and K. J. Abed, *Bull. of Magn. Reson.* **11**, 3 (1989).

117. L. D. Landau and E. M. Lifshitz, *Quantum Mechanics, Non-Relativistic Theory*, 3rd edition (Pergamon Press, Oxford, 1977).

118. S. Clough, A. J. Horsewill, P. J. McDonald and F. O. Zelaya, *Phys. Rev. Lett.* **55**, 1794 (1985).

119. J. T. Daycock and G. P. Jones, *J. Phys. C* **2**, 998 (1969).

120. R. F. Gloden, Euratom Report **EUR 4349, EUR 4358**.

121. M. Prager and A. Heidemann, *Tunneling Spectroscopy: Compilation of Available Data* , unpublished (1987).

122. A. Hüller and J. Raich, *J. Chem. Phys.* **71**, 3851 (1979).

123. J. E. Wollrab, *Rotational Spectra and Molecular Structure*, (Academic Press, New York, 1967).

124. O. L. Stiefvater, *J. Chem. Phys.* **62**, 233 (1975).

125. S. Clough, A. Heidemann, A. J. Horsewill, J. D. Lewis and M. N. J. Paley, *J. Phys. C: Solid State Phys.* **14**, L525 (1981).

126. M. J. Barlow, S. Clough, A. J. Horsewill and M. A. Mohammad, *Solid State Nuc. Magn. Reson.* **1**, 197 (1992).

127. B. Black, G. Majer and A. Pines, *Chem. Phys. Lett.* **201**, 550 (1993).

128. E. van Sydow, *Arkiv Kemi* **9**, 231 (1956).

129. R. C. F. Schaake, J. C. van Miltenberg and C. G. de Kruif, *J. Chem. Thermodynamics* **14**, 763 (1982).

130. R. C. F. Schaake, J. C. van Miltenberg and C. G. de Kruif, *J. Chem. Thermodynamics* **14**, 771 (1982).

131. J. F. Martin and R. J. L. Andon, *J. Chem. Thermodynamics* **14**, 679 (1982).

132. F. J. Streiter and D. H. Templeton, *Acta Crystallogr.* **15**, 1240 (1962).

133. F. J. Streiter, D. H. Templeton, R. F. Scheuermann and R. L. Sass, *Acta Crystallogr.* **15**, 1240 (1962).

134. R. F. Scheuermann and R. L. Sass, *Acta Crystallogr.* **15**, 1244 (1962).

135. R. T. Morrison and R. N. Boyd, *Organic Chemistry*, 4th edition (Allyn and Bacon, Newton, Mass., 1983).

136. J. Timmermans, *Bull. Soc. Chim. Belg.* **43**, 626 (1934).

LAWRENCE BERKELEY LABORATORY
UNIVERSITY OF CALIFORNIA
TECHNICAL INFORMATION DEPARTMENT
BERKELEY, CALIFORNIA 94720

ABH174
LBL Libraries